

NAVAL POSTGRADUATE SCHOOL MONTEREY, CALIFORNIA



THESIS

THE UTILITY OF HYPERSPECTRAL DATA TO
DETECT AND DISCRIMINATE ACTUAL AND
DECOY TARGET VEHICLES

by

Steven M. Bergman

December, 1996

Thesis Advisor:
Co-Advisor:

Richard C. Olsen
David D. Cleary

Approved for public release; distribution is unlimited.

19970625 048

REPORT DOCUMENTATION PAGE

Form Approved OMB No. 0704-0188

Public reporting burden for this collection of information is estimated to average 1 hour per response, including the time for reviewing instruction, searching existing data sources, gathering and maintaining the data needed, and completing and reviewing the collection of information. Send comments regarding this burden estimate or any other aspect of this collection of information, including suggestions for reducing this burden, to Washington Headquarters Services, Directorate for Information Operations and Reports, 1215 Jefferson Davis Highway, Suite 1204, Arlington, VA 22202-4302, and to the Office of Management and Budget, Paperwork Reduction Project (0704-0188) Washington DC 20503.

1. AGENCY USE ONLY (<i>Leave blank</i>)	2. REPORT DATE December 1996	3. REPORT TYPE AND DATES COVERED Master's Thesis	
4. TITLE AND SUBTITLE TITLE OF THESIS. The Utility of Hyperspectral Data to Detect and Discriminate Actual and Decoy Target Vehicles		5. FUNDING NUMBERS	
6. AUTHOR Steven M. Bergman			
7. PERFORMING ORGANIZATION NAME(S) AND ADDRESS(ES) Naval Postgraduate School Monterey CA 93943-5000		8. PERFORMING ORGANIZATION REPORT NUMBER	
9. SPONSORING/MONITORING AGENCY NAME(S) AND ADDRESS(ES)		10. SPONSORING/MONITORING AGENCY REPORT NUMBER	
11. SUPPLEMENTARY NOTES The views expressed in this thesis are those of the author and do not reflect the official policy or position of the Department of Defense or the U.S. Government.			
12a. DISTRIBUTION/AVAILABILITY STATEMENT Approved for public release; distribution is unlimited.		12b. DISTRIBUTION CODE	
13. ABSTRACT (<i>maximum 200 words</i>) The objective of this work is to evaluate the utility of hyperspectral signature data in satisfying time-sensitive intelligence requirements. This work is conducted in support of the Hyperspectral MASINT Support to Military Operations (HYMSMO) program. Data are used from the Hyperspectral Digital Imaging Collection Experiment (HYDICE) imaging spectrometer using the 0.4 μ m to 2.5 μ m wavelength range. Operation Forest Radiance I was the third in a series of HYMSMO-sponsored collection and exploitation experiments, and the data set analyzed herein was derived from this effort. The first phase of the Forest Radiance experiment emphasized the collection of spectra from a suite of overtly exposed mobile vehicles, decoys, and target panels. Analysis shown here was conducted to determine if it is possible to detect and discriminate real and decoy vehicles. The Low Probability of Detection (LPD) and Spectral Angle Mapper (SAM) anomaly detection and classification algorithms are applied to the data set being analyzed. The LPD algorithm performs well at detecting residual spectra, but produces a significant number of false alarms. The SAM technique is equally successful at detecting residual spectra and proves to have an advantage over the LPD when it comes to obviating misidentifications. This thesis shows that detection and discrimination of mobile vehicles (HMMWVs) and decoys in a natural grass environment is possible using this technology.			
14. SUBJECT TERMS Hyperspectral, Multispectral, Image Processing, Spectroscopy		15. NUMBER OF PAGES 135	
		16. PRICE CODE	
17. SECURITY CLASSIFICATION OF REPORT Unclassified	18. SECURITY CLASSIFICATION OF THIS PAGE Unclassified	19. SECURITY CLASSIFICATION OF ABSTRACT Unclassified	20. LIMITATION OF ABSTRACT UL

NSN 7540-01-280-5500

Standard Form 298 (Rev. 2-89)
Prescribed by ANSI Std. Z39-18 298-102

Approved for public release; distribution is unlimited.

**THE UTILITY OF HYPERSPECTRAL DATA TO DETECT AND
DISCRIMINATE ACTUAL AND DECOY TARGET VEHICLES**

Steven M. Bergman
Lieutenant, United States Navy
B.A., University of New Mexico, 1989

Submitted in partial fulfillment
of the requirements for the degree of

**MASTER OF SCIENCE IN SYSTEMS TECHNOLOGY
(SCIENTIFIC AND TECHNICAL INTELLIGENCE)**

from the

NAVAL POSTGRADUATE SCHOOL
December 1996

Author:

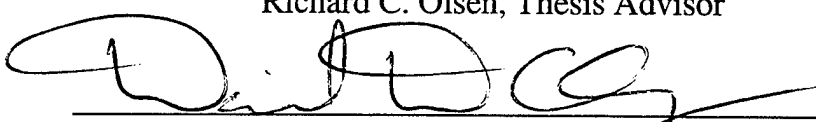


Steven M. Bergman

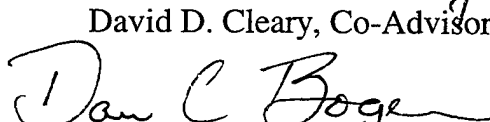
Approved by:



Richard C. Olsen, Thesis Advisor



David D. Cleary, Co-Advisor



Dan C. Boger, Chairman

Command, Control, and Communications Academic Group

ABSTRACT

The objective of this work is to evaluate the utility of hyperspectral signature data in satisfying time-sensitive intelligence requirements. This work is conducted in support of the Hyperspectral MASINT Support to Military Operations (HYMSMO) program. Data are used from the Hyperspectral Digital Imaging Collection Experiment (HYDICE) imaging spectrometer using the $0.4 \mu\text{m}$ to $2.5 \mu\text{m}$ wavelength range. Operation Forest Radiance I was the third in a series of HYMSMO-sponsored collection and exploitation experiments, and the data set analyzed herein was derived from this effort. The first phase of the Forest Radiance experiment emphasized the collection of spectra from a suite of overtly exposed mobile vehicles, decoys, and target panels. Analysis shown here was conducted to determine if it is possible to detect and discriminate real and decoy vehicles. The Low Probability of Detection (LPD) and Spectral Angle Mapper (SAM) anomaly detection and classification algorithms are applied to the data set being analyzed. The LPD algorithm performs well at detecting residual spectra, but produces a significant number of false alarms. The SAM technique is equally successful at detecting residual spectra and proves to have an advantage over the LPD when it comes to obviating misidentifications. This thesis shows that detection and discrimination of mobile vehicles (HMMWVs) and decoys in a natural grass environment is possible using this technology.

vi

TABLE OF CONTENTS

I. INTRODUCTION	1
II. BACKGROUND	5
A. DEVELOPMENT OF IMAGING SPECTROSCOPY	5
1. Basic Characteristics	5
2. Imaging Concept	7
a. Data Presentation	8
b. Information Extraction	9
c. Technological Limitations	12
3. Imaging Spectrometry Development	15
a. Evolution	16
b. LANDSAT MSS and TM	17
c. Airborne Imaging Spectrometer (AIS I/II)	19
d. Airborne Visible/Infrared Imaging Spectrometer (AVIRIS)	22
e. Moderate Resolution Imaging Spectrometer (MODIS)	26
f. Portable Hyperspectral Imager for Low Light Spectroscopy(PHILLS) ...	27
4. Development Summary	28
B. EXPLOITATION SOFTWARE	28
1. Spectral Image Processing System (SIPS)	29
2. Environment for Visualizing Images (ENVI)	29
C. SELECTED ALGORITHMS	30
1. Principal Components Analysis (PCA)	30
2. Low Probability of Detection (LPD)	31
3. Spectral Angle Mapper (SAM)	31
III. MILITARY APPLICATIONS	33
A. CLASSES OF APPLICATIONS	33
1. Strategic Level	33
2. Operational Level	34

3. Tactical Level	35
B. TACTICAL UTILITY	37
1. Gulf War Problem	37
2. Lessons Learned	39
3. Current and Future Capabilities	41
a. Application Examples	41
b. Cross-Cueing	44
c. Automatic Target Recognition	45
d. Tactical Support Platform	46
IV. EXPERIMENT DESCRIPTION	49
A. GENERAL METHODOLOGY	49
1. Levels of Information (LOI)	49
2. Guidance	49
B. OPERATION FOREST RADIANCE I	50
1. Background	50
2. Airborne Data Collection Objectives	51
3. H-Field Site Description	52
4. Experiment Design	53
a. Target Objects	54
b. Phase I - Exposed Material and Vehicle Experiments	57
c. Phase II - Shadow and Adjacency Experiments	58
d. Phase III - Concealed Vehicle Experiments	59
5. Ground-Truth Measurements	60
6. Sensor Characteristics	61
a. Hyperspectral Digital Imaging Collection Experiment (HYDICE)	61
b. Airborne Remote Earth Sensor (ARES)	63
7. Ground Data Processing Subsystem (GDPS)	65
V. OBSERVATIONS AND ANALYSES	67
A. TECHNICAL OBJECTIVE	67

B. DATA PROCESSING	67
1. Post-Flight Processing	67
2. Reflectance Conversion	68
a. Empirical Line Method (ELM)	68
C. ANALYSES	69
1. Forest Radiance I Data Set	69
2. Methodology/Approach	71
D. FINDINGS	71
1. Qualitative Analysis of Signatures	71
2. Principal Components Analysis (PCA) Results	80
3. Low Probability of Detection (LPD) Results	84
4. Spectral Angle Mapper (SAM) Results	95
VI. CONCLUSIONS AND RECOMMENDATIONS	109
LIST OF REFERENCES	111
BIBLIOGRAPHY	115
INITIAL DISTRIBUTION LIST	117

ACKNOWLEDGEMENTS

The author would like to thank the following members of the HYDICE Program Office (HYPO) for their support during this research - Greg Pavlin, Pete Mitchell, Mary Kappas, Debbie Davidson, Dave Aldrich and Shelley Seburn. A very special thanks to Ron Resmini and Todd Westphal who were extremely generous in sharing their time and extensive experiences with the author. Financial support provided by the Office of Naval Intelligence (ONI), Professor Conner, and funding provided by the HYPO to Professor Olsen is gratefully acknowledged.

EXECUTIVE SUMMARY

The objective of this work is to evaluate the utility of hyperspectral signature data in satisfying time-sensitive intelligence requirements. Emphasis is placed on ascertaining the utility of hyperspectral data and exploitation techniques to detect and discriminate the spectral signatures of exposed mobile vehicles (HMMWVs) and decoys against the natural grass background. A thorough examination of the spectral variability inherent in these target objects was conducted.

This work is conducted in support of the Hyperspectral MASINT Support to Military Operations (HYMSMO) program. Data are used from the Hyperspectral Digital Imaging Collection Experiment (HYDICE) imaging spectrometer using the $0.4 \mu\text{m}$ to $2.5 \mu\text{m}$ wavelength range. HYDICE was designed and developed by Hughes-Danbury Optical Systems, Inc., to provide high quality hyperspectral data to explore literal and nonliteral exploitation techniques for a wide variety of military and civil applications. The sensor is integrated onboard an Environmental Research Institute of Michigan (ERIM) Convair (CV-580) aircraft. The sensor is a nadir-viewing, 210 channel imaging spectrometer. Radiance data are sampled contiguously in 10 nanometer (nm) wide channels using a pushbroom technique. The sensor covers a swath width of approximately 1 km and provides a ground sample distance (GSD) ranging from 0.75 to 3 m, depending on its operating altitude.

Operation Forest Radiance I was the third in a series of HYMSMO-sponsored collection and exploitation experiments, and the data set analyzed herein was derived from this effort. The Forest Radiance I tests were staged at the Aberdeen Proving Ground's H-Field from 17 to 31 August 1995. The H-Field range proved to be an ideal physical environment to examine the physics and phenomenology of various military target classes under different environmental conditions. H-Field is located on Edgewood Peninsula approximately 20 miles northeast of Baltimore, MD. The experiment was executed in three separate phases, each employing a progressive state of concealment.

The first phase, Phase I, emphasized a suite of overtly exposed vehicles, decoys, and target panels. In Phase II, the observables were re-deployed to the shadowed area adjacent to the treeline. In Phase III, the objects were again re-deployed under canopy for partial concealment. To satisfy the broad range of objectives, a wide array of target objects of varying shapes, sizes, and material types were deployed in different orientations throughout the test area.

There are a number of recently developed anomaly detection and classification algorithms being used in the hyperspectral remote imaging community. A thorough examination of two on-line target and anomaly detection methods was conducted. This document defines an anomaly as a target of military interest. The Low Probability of Detection (LPD) and Spectral Angle Mapper (SAM) methods are applied to the data set being analyzed. The LPD method is a statistically-based scene-dependent anomaly detection technique. The algorithm suppresses the unwanted spectral signatures that dominate the image, leaving the remaining spectral signatures to appear as false alarms in the output. The LPD algorithm performs well at detecting residual spectra, but produces a significant number of false alarms. The SAM algorithm is a statistical technique that takes advantage of spectral similarities shared between an endmember and each test pixel in the image cube. It is able to match the spectra without giving statistical weight to their relative brightness values to produce a quantifiable measure of effectiveness. The SAM technique is equally successful at detecting residual spectra and proves to have an advantage over the LPD when it comes to obviating misidentifications.

This thesis shows that detection and discrimination of mobile vehicles (HMMWVs) and decoys in a natural grass environment is possible using this technology. The findings clearly show that the actual and decoy target objects are differentiable in a natural grass environment. The low number of false alarms on the decoys serves as strong evidence that the objects are being identified, not just detected. The significant high false alarm rate of the real vehicles indicates that the spectral signatures are actually the signature of the surface paint, not the vehicle itself. The different hues in the paint scheme did prevent the possibility of acquiring homogeneous pixels; thus, a single pixel

is characterized by a one signature that represents all of the paint's spectral components. This complex pixel problem seemed to stress the performance of the LPD and SAM algorithms.

Hyperspectral technologies can be a viable tactical asset if the technology is allowed to advance at its current rate. Despite these initial successes, however, further analysis will be required to determine the practicality of using hyperspectral technologies to satisfy many of the requirements relevant to the warfighter. Any negative findings concerning this data set or analysis techniques to discriminate anomalous contacts should not be extrapolated to past or future experiments.

I. INTRODUCTION

Remote sensing is the science of gathering information about an object without having direct contact with it. The quantity most often measured is the electromagnetic (EM) energy reflecting or emanating from the object of interest. For decades, photographic cameras have been used to produce quality hardcopy imagery products for manual analysis. Recent years, however, have witnessed significant technological advances in the design of more sophisticated collection methods capable of recording EM radiation digitally. This technique has proven extremely reliable and has increased the ability to quickly and accurately measure and process large quantities of imaging data. Storing EM radiation digitally has also accelerated the development of new approaches to quantifying target-energy interaction well beyond the traditional image-oriented technologies. One such technology to emerge involves simultaneous acquisition of images and spectra. This technology is commonly referred to as imaging spectroscopy.

Imaging spectroscopy has acquired the cognomen of “hyperspectral imaging.” Hyperspectral imagers provide a new dimension in exploiting the EM spectrum, particularly in the visible, near-infrared (NIR) and short-wave-infrared (SWIR) regions. These instruments are capable of collecting reflected solar data over a large number of discrete, contiguous spectral bands or channels. This capability represents a major advance in the collection and exploitation of signature data by providing near-complete spectral coverage of sufficient resolution to identify narrow absorption features of both natural and man-made objects. It is this increased level in spectral resolution that makes the observation of subtle variations in a material’s spectra possible for the first time. Hence, the principal goals of hyperspectral imaging can be described as the observation of radiometric, spectral, spatial, and temporal variation which quantify information about the distribution of energy leaving objects of interest.

The military is currently evaluating the utility of hyperspectral signature data and exploitation techniques to satisfy time-sensitive intelligence requirements. Through the

years the military has relied heavily upon manual interpretation of pan-chromatic imagery to identify point targets based solely on their spatial characteristics. Today, hyperspectral imagers emphasize the spectral element of an image scene, which can provide insight into the properties of surface materials and provide valuable information about identities and conditions of terrain, vegetation, and objects. This technology has allowed us to push beyond the spatial exploitation of panchromatic imagery; that is, an analyst can now make analytical determinations based on the object's unique spectral signature. The opportunity for real-time adaptive processing is feasible and particularly important, especially in contrast to the present labor-intensive manual processes now being employed. All hyperspectral image data collected and processed for military use currently falls under the purview of the Measure and Signature Intelligence (MASINT) community of the Department of Defense (DoD).

The work presented here is part of the Hyperspectral MASINT Support to Military Operations (HYMSMO) program (pronounced "*High-Mizz-Mo*"). The program can be traced back to a Defense Intelligence Agency (DIA) sponsored survey that identified vetted Support to Military Operations (SMO) requirements uniquely suited to the MASINT community. The HYMSMO program was established to demonstrate and, if possible, validate the utility of these new imaging technologies as a means to satisfy these high priority needs. The technology validation phase of the program is well underway and the results to date show great promise. The technology can be applied to the traditional Scientific and Technical Intelligence (S&TI) role of the MASINT community, as well as the more non-traditional MASINT applications. These SMO requirements can be either strategic in nature, in the form of treaty compliance and verification missions, or focus on the more operational and tactical reconnaissance and surveillance operations.

The HYMSMO program evolved from a Congressionally-funded "Dual Use" initiative which leveraged from existing civilian-controlled multispectral imaging programs. The workhorse of the program is the Hyperspectral Digital Imaging Collection Experiment (HYDICE) instrument. The HYDICE instrument brings cutting edge technology to challenging intelligence problems by providing extremely high spectral

fidelity, increased spatial resolution, and superior dynamic range and signal-to-noise performance. The HYDICE Project Office (HYPO) is designated the executive agent for all HYDICE operations. The HYPO is an end-to-end organization whose responsibilities span all aspects of program operation, from transforming user requests into tailored experiments and mission flight profiles, to the processing of raw data for exploitation and dissemination. The organization consists of four core groups or functional components: a sensor development team; a collection team; an exploitation team; and an advanced systems technology team. Each of these groups are staffed by highly trained professionals working in the fields of geology, physics, engineering, computer science, and aviation.

The HYPO has designed and executed five data collection experiments during CY-94 and CY-95. The purpose of these applied remote sensing experiments were to ascertain the utility of the technology to satisfy the Levels of Information (LOIs) identified by each of the services. The experiments were designed with the philosophy of first trying to satisfy as many SMO requirements as possible and to conclude with a bottom-up technology assessment. The experiments are typically executed at a single collection site. Observables include overtly exposed, partially exposed, and concealed targets (i.e., military vehicles, decoys, camouflage netting, painted wood, metal, and canvas panels) situated in a target array to facilitate collection and exploitation. The first of these experiments, Operation Desert Radiance I, was conducted in October 1994. Operation Desert Radiance II, June 1995, Operations Forest Radiance I and Urban Radiance I, August 1995, and Operation Island Radiance, October 1995, rounded out the non-literal collection experiments scheduled during this time frame. The Forest Radiance I experiment was staged at the U.S. Army's Aberdeen Proving Grounds, MD, from 18-31 August, and the data sets exploited herein were derived from this operation.

This thesis is broken down into six chapters. Chapter I is the INTRODUCTION. Chapter II, BACKGROUND, provides the reader with an understanding of the hyperspectral imaging concept and a historical summary of various multiband imaging technologies. Chapter III, MILITARY APPLICATIONS, describes the classes of

applications and describes the technology's tactical utility. Chapter IV, **EXPERIMENT DESCRIPTION**, defines the objective and presents a physical description of the collection site. Chapter V, **OBSERVATIONS AND ANALYSIS**, describes the data set analyzed and presents the results of the analyses. Chapter VI, contains the **CONCLUSIONS AND RECOMMENDATIONS** drawn from Chapter V.

II. BACKGROUND

A. DEVELOPMENT OF IMAGING SPECTROSCOPY

Imaging spectroscopy is based upon the observed spectral differences that are either reflected or emitted from an object of interest. This principle forms a basis for understanding the concept of hyperspectral imaging. Imaging spectroscopy can be characterized as the science of observing spectral differences among materials and objects for the purpose of deriving information about them (Campbell, 1987).

1. Basic Characteristics

Remote sensing systems collect and record the EM radiation leaving the surface of an object, generally emphasizing select portions of the spectrum. Figure 2.1 illustrates the spectral imagery components that interact to create the recorded signature. The yellow lines provide a visual trace of the sun's energy interacting with objects on the

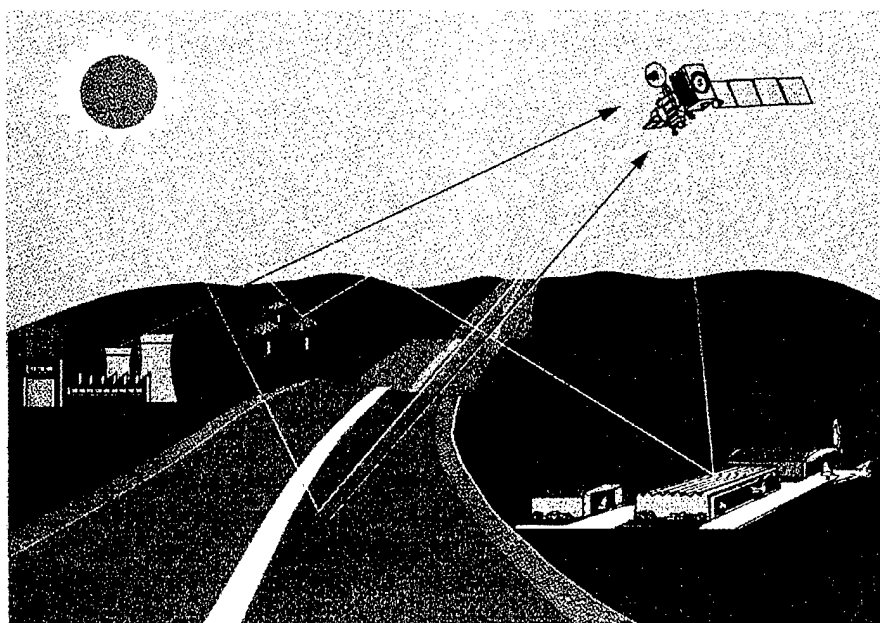


Figure 2.1. Spectral Imaging Components (From MUG, 1995)

earth's surface and the path it takes towards the collection sensor. Thermal sources are also present in the figure and its path is shown in red.

The most obvious portion of the spectrum to exploit is the visible region, which encompasses only a small fraction of the full EM spectrum ($0.4 \mu\text{m}$ to $0.7 \mu\text{m}$). A major advantage of hyperspectral imaging is the capability to record radiance data from the part of the spectrum not visible to the naked eye. The primary regions of the EM spectrum used in remote sensing are shown on the in Figure 2.2. The reflected solar energy is defined by the ultra violate (UV), visible, near-infrared (NIR), and short-wave-infrared (SWIR) regions of the spectral continuum. The mid-wave-infrared (MWIR) is

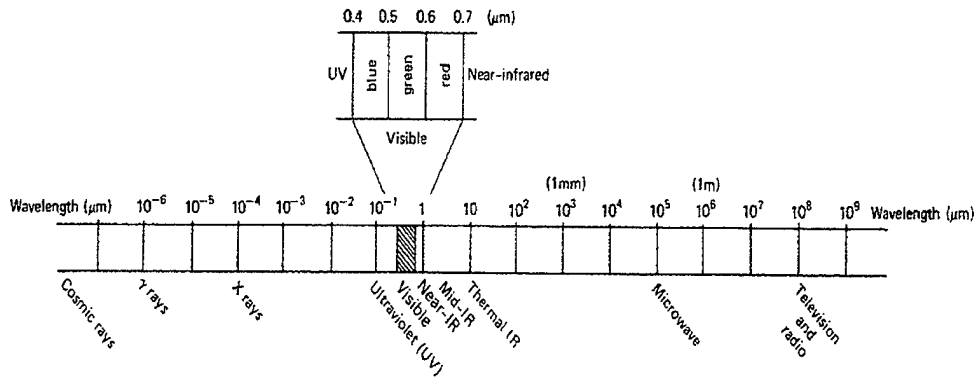


Figure 2.2. Electromagnetic Spectrum

characterized as a mix of reflected solar radiation and emitted (thermal) energy. The longwave-infrared (LWIR) region is dominated entirely by thermal emissions. The regions examined in this thesis are focused on the visible, NIR, and SWIR regions of the spectrum. The NIR and SWIR are defined as those regions immediately adjacent to the visible region, from $0.7 \mu\text{m}$ to $1.1 \mu\text{m}$ and $1.1 \mu\text{m}$ to $2.5 \mu\text{m}$, respectively.

Solar radiation must first pass through the Earth's atmosphere before it can interact with an object on the ground. As the energy travels through the atmospheric medium it can be either absorbed or scattered by various airborne gases or particulates.

Figure 2.3 illustrates the physical processes of how solar energy interacts with the atmosphere before it reaches the Earth's surface. This process is largely dependent upon

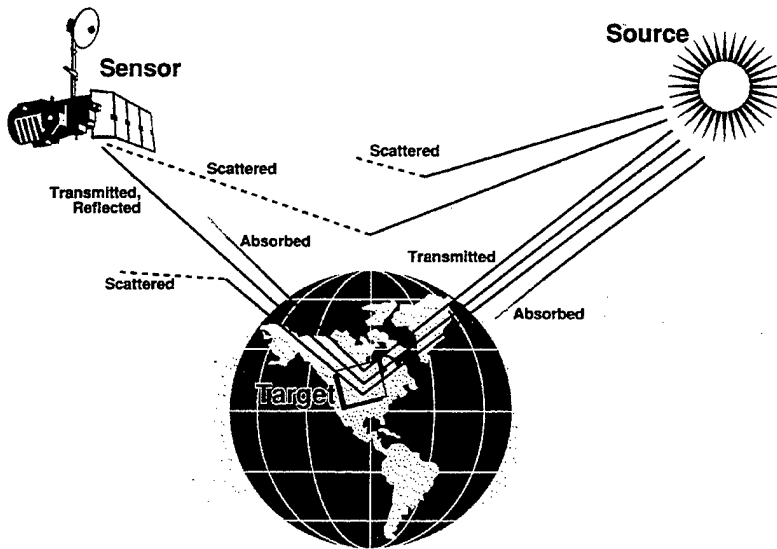


Figure 2.3. Atmospheric Effects (From LANDSAT Advertisement, 1985)

the wavelength of the solar energy and the size of the absorber or scatterer. The portion of the energy that reaches the object and reflects in the direction of the sensor is recorded by its optics. This reflected energy is again subjected to the intervening atmosphere as it travels towards the sensor. Once the light enters the sensor it is then converted into an electrical signal and recorded as radiance value or digital number (DN). The recorded spectral signature is a function of the properties of the irradiated object.

2. Imaging Concept

Spectral imaging can be categorized as either multispectral, hyperspectral, or ultraspectral, as shown in Figure 2.4. The multispectral sensors record data in tens of bands, hyperspectral in the hundreds, and ultraspectral will collect in the thousands. Ultraspectral sensors are still in the research and development phase, but proof-of-concept efforts are currently underway in the field.

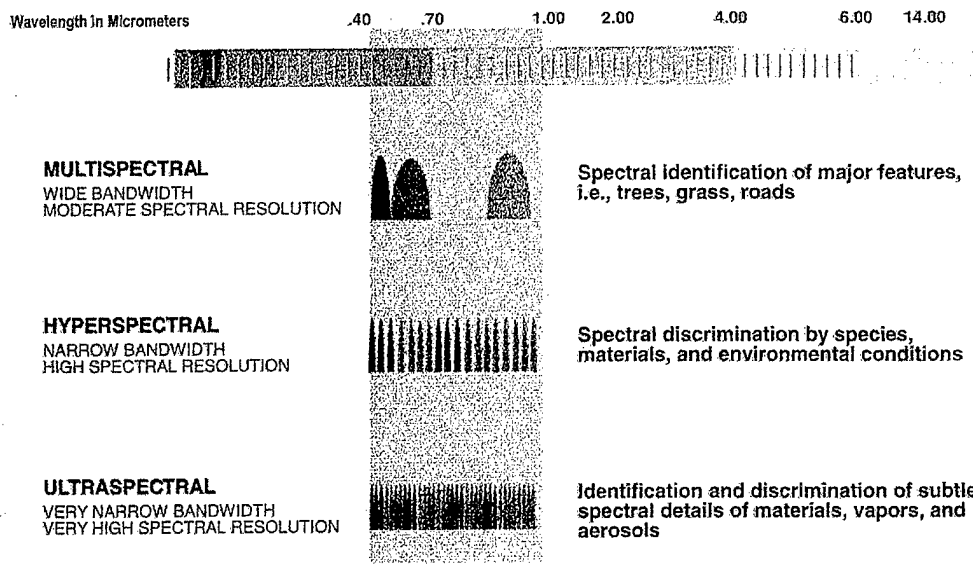


Figure 2.4. Spectral Imaging Types (From MUG, 1995)

a. Data Presentation

Hyperspectral imaging is generally described as a measurement of energy from both natural and man-made surfaces. The measured intensity as a function of wavelength (λ) creates a spectral record of a given material in hundreds of contiguous bands within a specific portion of the EM spectrum. For reflected solar energy this spectral record is based upon the variations in reflectance between $.4 \mu\text{m}$ to $2.5 \mu\text{m}$, and is typically represented by either a 2-dimensional graphical plot or a 3-dimensional image cube. Figure 2.5 illustrates the line spectra and image cube concept. The ordinates of the 2-dimensional line spectral plot are percent reflectance (R) versus wavelength. The 3-dimensional image cube is formed from a stack of images whose spatial axes correspond to the physical location and structure of the imaged objects. The third axis corresponds to the number of wavelength bands of the sensor.

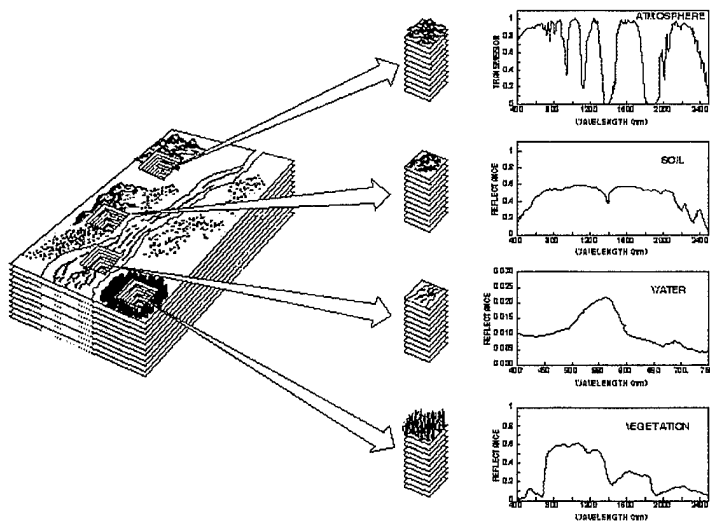


Figure 2.5. Hyperspectral Concept (From AVIRIS Advertisement, 1992)

b. Information Extraction

Hyperspectral imaging has a wide range of applications in the fields of geology, botany, oceanography, and phenomenology. The intent is to record spectral variations over a broad range of wavelengths in order to spectrally detect, classified, and identified materials of interest. The power of this concept came be seen in Figure 2.6, where the line spectral plot of three clay minerals (Kaolinite, Montmorillonite, and Muscovite) and two carbonate (Calcite and Siderite) are superimposed. Observe that each material can be clearly identified by its own unique spectral signature. Kaolinite, for example, can be identified by the two strong, single absorption features located at $1.4\text{ }\mu\text{m}$ and $2.3\text{ }\mu\text{m}$. The Montmorillonite also has two equally strong features at $1.4\text{ }\mu\text{m}$ and $2.2\text{ }\mu\text{m}$, and one significant feature at $1.9\text{ }\mu\text{m}$, while Muscovite exhibits a very small feature at $1.4\text{ }\mu\text{m}$ and a strong one at $2.2\text{ }\mu\text{m}$. Calcite, on the other hand, exhibits a strong double absorption feature at $2.2\text{ }\mu\text{m}$, and has a relatively uniform reflectance from $0.8\text{ }\mu\text{m}$ to $2.1\text{ }\mu\text{m}$. Also note that the Siderite has virtually no reflectance value at $1.0\text{ }\mu\text{m}$, but increases

rapidly to its maximum reflectance value at $2.1\text{ }\mu\text{m}$. Siderite also shows a significant absorption feature at $2.3\text{ }\mu\text{m}$.

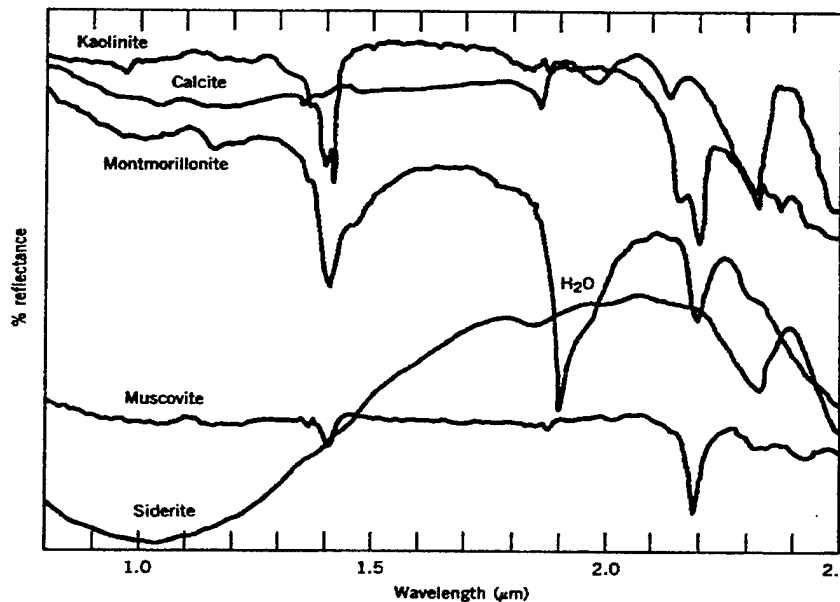


Figure 2.6. Mineral Surface Reflectance (From Rinker, 1990)

In addition to these spectral features, the variation in percent reflectance (albedo) between these five materials provides another measure of spectral separability. The spectral reflectance characteristics of a mineral is heavily influenced by a number of factors. The shape or structure of the spectra at wavelengths near $0.92\text{ }\mu\text{m}$ is dominated by electronic transitions in the d-cell electrons. At $1.0\text{ }\mu\text{m}$, vibrational absorption occurs due to the presence of bound and unbound water molecules in the material. Absorption in the $2.1\text{ }\mu\text{m}$ to $2.4\text{ }\mu\text{m}$ region is attributed to combination bending-stretching overtones in OH vibrations (Vane et al., 1993). Knowledge of these physical processes allows us to understand the variations in spectra observed in natural materials.

Reflectance curves of vegetation are inherently less structured than those of minerals in the $0.4\text{ }\mu\text{m}$ to $2.5\text{ }\mu\text{m}$ range, and show even more natural variability.

Figure 2.7 shows a typical reflectance spectra for green vegetation from $0.4\text{ }\mu\text{m}$ to $0.9\text{ }\mu\text{m}$. The visible portion of the spectrum is dominated primarily by absorption associated

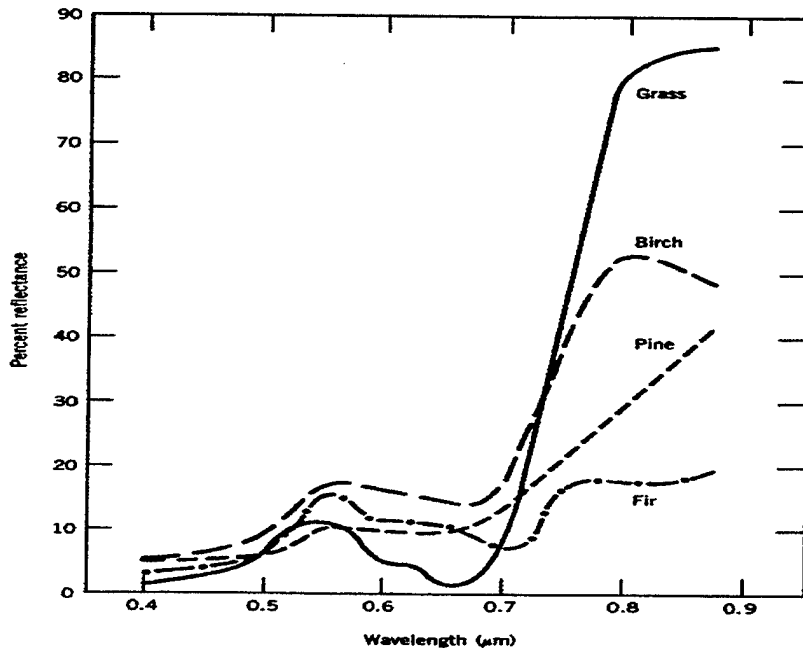


Figure 2.7. Vegetative Reflectance Curves (From Richards, 1995)

with the vegetation's chlorophyll pigment. In the NIR region, reflectance increases sharply at wavelengths longward of $0.7\text{ }\mu\text{m}$. This region is termed the red edge of the chlorophyll band. Absorption in the MWIR region is dominated by the extremely high water content typically found in green leaf vegetation. These spectra vary in this region since the water content varies substantially in healthy vegetation (Hoffer et al., 1978).

The diagnostic study of spectral signatures and absorption features can generally be divided into the three categories: detection; classification; and identification. Detection is primarily accomplished by observing and identifying pixels of different reflectance values. Changes in these values can be attributed to various changes in a material's albedo, physical structure, chemical composition, or illumination geometry. After an object is detected, the next step is to classify the object as a target type. Target

classification can be accomplished by grouping all pixels possessing the same brightness values, specific absorption characteristics, or overall spectral features into the same class. The final and most difficult step is to spectrally identify the material. The difficulty here is that material identification is more like a "black art" than an exact science. Final identification is typically based upon the experience level of the analyst, rather than a single analytical technique (Elachi, 1987).

c. Technological Limitations

The primary limitation associated with observing subtle spectral variations is determined by the total number of spectral bands supported by a sensor. The LANDSAT systems, for example, acquires data in a relatively small number of non-contiguous spectral bands (MSS - five and TM - seven), each band having a nominal bandpass between 60 to 100 nanometer (nm). This low number of spectral bands, coupled with the rather broad bandwidth, precludes resolution of many common absorption features at certain wavelengths. Figure 2.8 shows the MSS and TM coverage of six spectra to illustrate how the gap in spectral coverage could possibly lead to

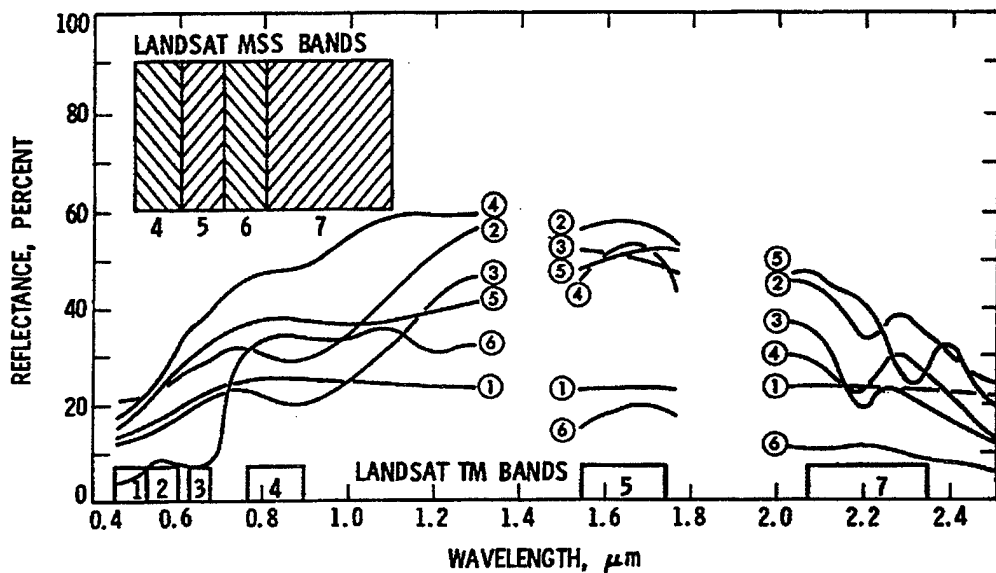


Figure 2.8. LANDSAT MSS and TM Coverage (From Vane et al., 1988)

ambiguities and misidentification. Also observe that two major atmospheric water absorption features appear at $1.4\text{ }\mu\text{m}$ and $1.9\text{ }\mu\text{m}$, rendering these regions completely unusable. The more sophisticated hyperspectral imagers enable sampling in hundreds of narrow, contiguous spectral bands. The value of this capability lies in the sensor's ability to resolve these ambiguities by acquiring a complete reflectance record across the entire spectrum.

The collection system determines the size of the smallest recognizable object in an imaged scene. This spatial resolution is typically referred to as ground resolution or ground sample distance (GSD), and will vary significantly depending on the sensor's design and viewing geometry. GSD is defined as the distance between the centers of adjacent pixels. Varying the altitude of the sensors is the easiest method of achieving different spatial resolutions and swath widths of the resulting imagery. Figure 2.9 uses a football field to compare the GSD of various multispectral sensors in use today. The lower resolution instruments (e.g., 10 to 30 meters (m)) will not normally facilitate literal detection of objects less than 5 m in size. It will, however, provide broad

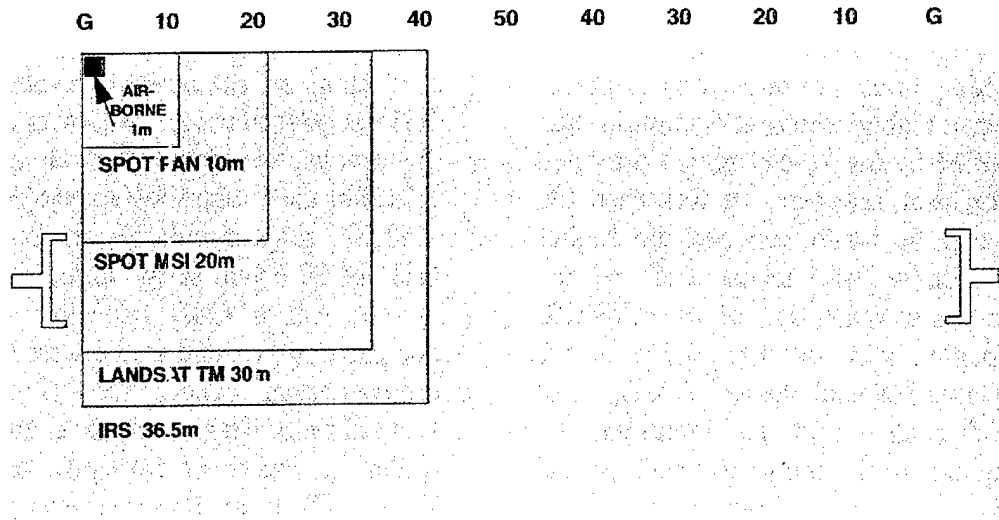


Figure 2.9. Spectral Resolution of Common Sensors (From MUG, 1995)

area coverage to detect large geographic formations and linear features like roads and bridges. The HYMSMO program is currently exploring several non-literal exploitation techniques potentially capable of detecting the presence of military relevant targets at the subpixel level. However, high resolution of smaller areas is preferred for detection and identification of most targets of interest. The HYDICE sensor can obtain a 1 m GSD when operated at an altitude of 1100 m or less.

Another characteristic that limits data collection is the instrument's scanning mechanism. The earlier MSS and TM instruments used an optomechanical system that recorded reflected radiance in a small number of discrete detector elements. These systems collected spatial information by sweeping the optics back and forth in a "whisk broom" motion perpendicular to the flight path (Figure 2.10.a). This technique was seriously limited by the short residence time of the detector's instantaneous field of view (IFOV). Subsequent MSS and TM designs increase this residence time by employing line-array detector elements (Figure 2.10.b). In this configuration each cross-track pixel had its own detector element in the array, increasing resident time to the interval needed to move one IFOV along the flight path. This too, however, had its own limitations in that each array would require its own spectral bandpass filter. Another approach resembling this design involved the addition of a dispersion element to split the reflected energy of each pixel into as many wavelengths as there are detector elements (Figure 2.10.c). This design was also limited to the slower airborne collection missions until improvements to the optomechanical mechanism could be made. The preferred configuration for spaceborne applications is the two-dimensional area-array detectors which collects radiance data using a "pushbroom" imaging approach (Figure 2.10.d). This technique obviated the need for a scanning device by providing an entire column of detector elements for each cross-track pixel, which increases the exposure time for each pixel. In pushbroom imaging, the image is formed by acquiring data through a slit in the foreoptics and dispersing it onto the area-array detector. The main problem associated

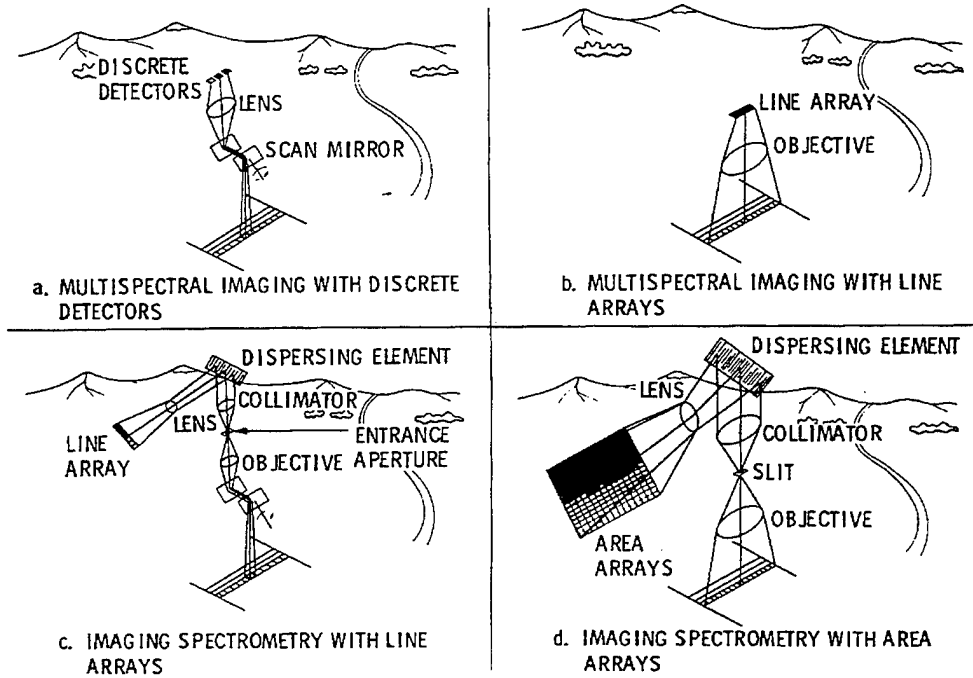


Figure 2.10. Four Approaches to Spectral Scanning: (a) Discrete Line Detectors; (b) Line Arrays; (c) Line Arrays With Dispersing; and (d) Area Arrays. (From Goetz et al., 1985)

with this configuration is that the optical system must maintain the necessary spatial field and spectral dispersion throughout the collection process, and variations in sensor response across the array must be compensated for (Goetz et al., 1985; Herring, 1987).

3. Imaging Spectrometry Development

To answer the ever-increasing calls for terrestrial analysis, the complexity of airborne and spaceborne instruments have increased significantly with each successive generation. Two specific types of sensors have had a marked impact on the development of the HYDICE imager. These include (1) airborne instruments with both high spectral and spatial resolution, and (2) spaceborne sensors with high spatial resolution but low spectral resolution. Some of the more notable imaging systems that contributed to the development of this sensor and a few that are currently being evaluated are detailed below.

a. Evolution

The origins of spectral sampling of the EM spectrum can be traced as far back as World War I (WWI), when even the most crude comparison techniques proved useful to imagery analysts. The first concerted effort to divide the EM spectrum into discrete spectral bands were conducted during World War II (WWII). Termed multiband photography, researchers successfully developed the means to separate the spectrum into 60 to 100 nm bands through a combination of different photographic emulsions and filters. These efforts, while rudimentary by today's standards, represented a significant advance to improving the targeting and terrain mapping techniques of that era.

The emergence of digital electronic imaging was an extremely important advance in spectral imaging. The LANDSAT Multispectral Scanner (MSS) was the first of these satellites to be deployed in 1972. This sensor recorded five, 100 nm wide bands: two in the visible (red and green); two in the NIR; and one the LWIR. The LANDSAT program continued to advance with the development of the Thematic Mapper (TM) design. TM divided the EM spectrum into seven, 60 nm wide channels: three in the visible (blue, green and red); one in the NIR; two in the MWIR; and one in the LWIR. The concept of dividing the EM spectrum into narrower and narrower, discrete spectral bands continued into the late 1970s with the development of the Shuttle Multispectral Infrared Radiometer (SMIR) and the Thermal Infrared Mapping Sensor (TIMS) . Each of these instruments, however, still lacked the spectral resolution needed for more precise surface studies.

The next major development in instrument design facilitated the acquisition of spectral data over hundreds of discrete, contiguous spectral bands. These instruments, referred to as imaging spectrometers, ushered in a new era in multiband imaging. The Airborne Imaging Spectrometer (AIS) was the first of these new systems to emerge. The AIS multispectral instrument separated the $1.2 \mu\text{m}$ to $2.4 \mu\text{m}$ region of the spectrum into 128 contiguous bands, each having a nominal bandpass of less than 10 nm. The Airborne Visible/Infrared Imaging Spectrometer (AVIRIS) was the next major imaging sensor to be put into operation. This instrument divided the spectrum into 224

contiguous spectral bands from 0.4 μm to 2.5 μm , each channel having a 10 nm wide bandwidth. This increase in spectral coverage and resolution was instrumental in bringing this technology to a wide range of military applications, to include terrain analysis, targeting, and intelligence gathering. The AVIRIS sensor is considered the archetype hyperspectral imager. The HYDICE instrument is one of the latest generation of airborne hyperspectral imagers. The HYDICE instrument operates in the 0.4 μm to 2.5 μm region, and collects signature data across 210 contiguous spectral bands in 10 nm wide bandwidths. HYDICE was the first imaging spectrometer specifically designed and built to determine the utility of hyperspectral technologies to SMO. The Portable Hyperspectral Imager for Low Light Spectroscopy (PHILLS) instrument is the latest imaging technology to be placed into operation.

b. LANDSAT MSS and TM

The LANDSAT MSS (Figure 2.11) series satellites went into operation with the launch of LANDSAT-1 in 1972, followed by LANDSAT-2 (1975), and then LANDSAT-3 (1978). These earth observing satellites were developed under the auspices of the National Aeronautical and Space Administration (NASA) with the intent to provide complete, continuous coverage of the earth's surface. The spacecraft were placed in a near-polar, sun-synchronous orbit, crossing the sample point on the surface of the earth at the same local time each day. At an orbital altitude of 920 kilometers (km), the MSS scanned across the earth in one direction perpendicular to the flight path of the spacecraft. LANDSAT-1 and -2 used four discrete detector elements to record the reflected energy, and then converted it to machine-readable electronic signals (Figure 2.10.a). LANDSAT-3 used 5 discrete detectors to perform this function. Each detector records the Earth-reflected sunlight at discrete wavelength bands. As mentioned earlier, the MSS sensor responds to two wavelengths in the visible (red and green) spectral region and two in the reflected IR. LANDSAT-3 had an additional band that responded to the thermal IR. These three sensors are no longer operational.

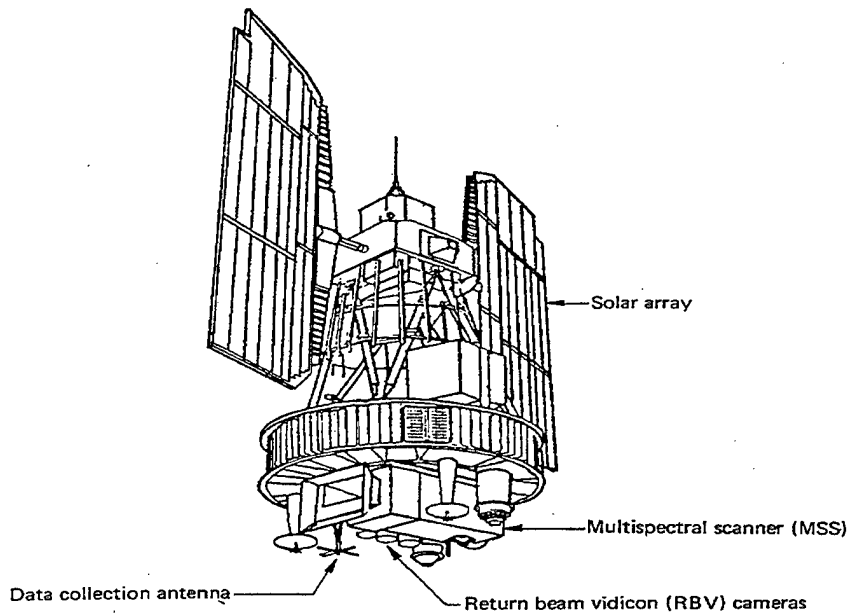


Figure 2.11. LANDSAT MSS (From LANDSAT Advertisement, 1985)

The LANDSAT-4 and -5 satellite series are second generation spacecraft and carry both the MSS and the more capable TM instrument (Figure 2.12). The spacecraft were placed in the same orbital plane as the earlier version, but at a lower altitude of 705 km. This lower altitude provides a spatial resolution of 30 m for the visible and 120 m for the thermal IR. The enhanced TM expands spectral coverage to detect reflected radiation in seven wavelength bands at key positions in the spectrum: three visible (blue, green, and red) bands; one in the NIR, two in the MWIR, and one in the LWIR. The TM scans with sixteen lines in both directions across the same 185 km swath width, using a modified scanning approach. Both LANDSAT-4 and -5 have already exceeded their operational life expectancy, but continue to operate to this day.

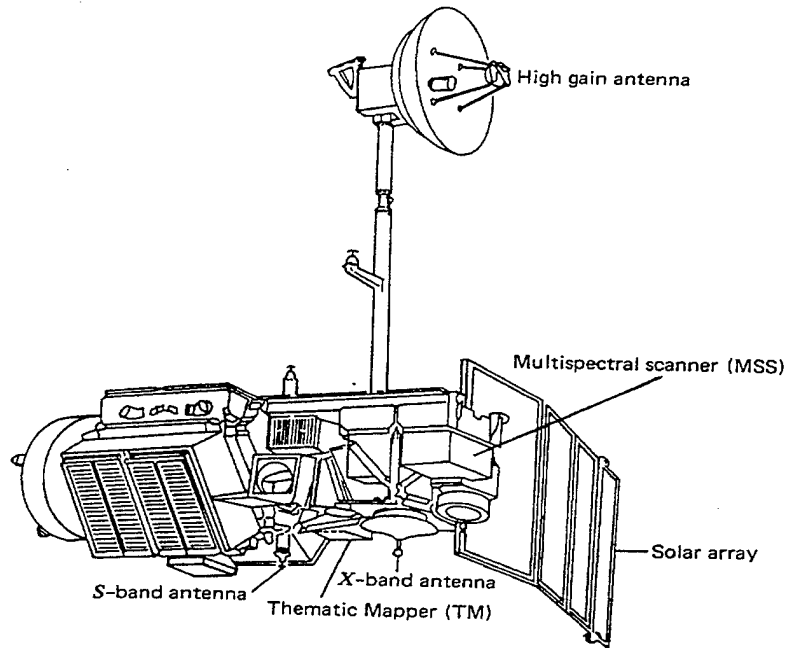


Figure 2.12. LANDSAT TM (From LANDSAT Advertisement, 1985)

c. Airborne Imaging Spectrometer (AIS I/II)

The Airborne Imaging Spectrometer I (AIS I) was the test bed for future spaceborne infrared collectors and operated at substantially higher spectral resolution than previous instruments (Figure 2.13). The AIS I instrument flew in 1984 and 1985. The sensor exceeded all program expectations and quickly became in great demand throughout the remote sensing community. Its first flight was conducted aboard a DC-3 aircraft and later flew exclusively aboard a NASA C-130. AIS successfully recorded over 7,000 miles of imagery data in the United States, Australia, and Europe during its two years of operation (Vane, et al., 1988). The sensor collected radiance data in 128, 9.3 nm wide spectral bands from $1.2 \mu\text{m}$ to $2.4 \mu\text{m}$. This sampling interval provided sufficient spectral resolution to identify fine material absorption features previously left unrecorded by the earlier instruments. The aircraft flew at a nominal altitude of 4.2 km, producing a GSD of approximately 8 m. The instrument was primarily designed as a test bed for detector development and was the first to operate using a two-dimensional 32X32

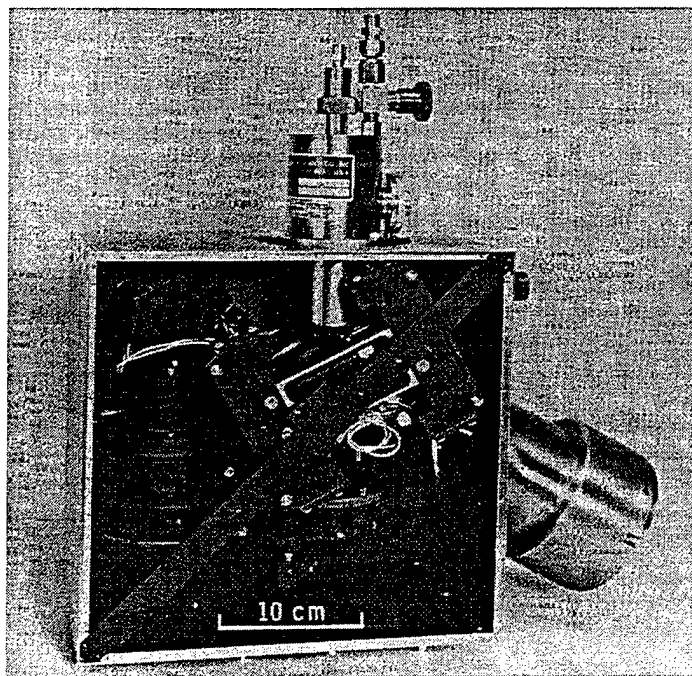


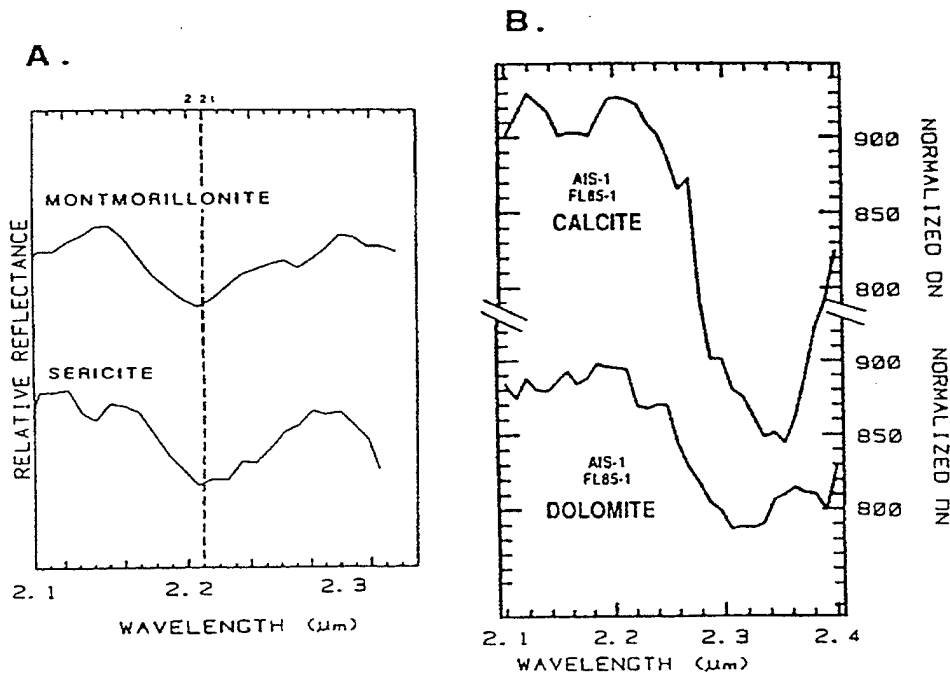
Figure 2.13. Airborne Imaging Spectrometer (From Vane et al., 1988)

element detector array (Figure 2.10.d). This mode of operation obviated the need for a scanning mechanism and made high speed collection possible. AIS II was the next generation of sensors to fly in 1986. The AIS II was designed to collect data in 160 contiguous, 10.6 nm wide spectral bands from 0.9 μm to 2.4 μm . It too utilized the same detector scheme, but developers expanded the detector array to a total of 64X64 elements (Goetz et al., 1985).

AIS acquired data of the northern Grapevine Mountains on the border between Nevada and California, from 1984 to 1986. A total of seven collection experiments took place over the study area. The goal here was to analyze hydrothermally altered rock formations to better define the alteration zones and provide alteration intensity information. Reflectance spectra was collected using only the last 32 bands ($\sim 2.1 \mu\text{m}$ to $2.4 \mu\text{m}$) of the sensor. These regions were selected because they contain the majority of the absorption characteristics associated with most naturally occurring

minerals. The strongest absorption features in the material's spectra was defined as the wavelength of the bandpass position, and then mapped into a single plane, hue, saturation, intensity (HSI) color image. This technique facilitated identification of several mineral groups throughout the test site, as shown in Figures 2.14a and 2.14b.

The AIS data positively identified Sericite by its absorption features at 2.21 μm , 2.25 μm , and 2.35 μm . Montmorillonite was found based on its modest absorption features at 2.21 μm and 2.35 μm . Calcite and Dolomite were also identified their absorption features at 2.32 μm and 2.34 μm . Figure 2.15 maps the mineral distribution based upon the results of the study. This AIS generated map was later compared to an *in situ* produced map of the test site and was found to be very accurate (Kruse, 1987).



Figures 2.14a and 2.14b. Material Spectra: (a) Montmorillonite and Sericite; and (b) Calcite and Dolomite (From Kruse, 1987)

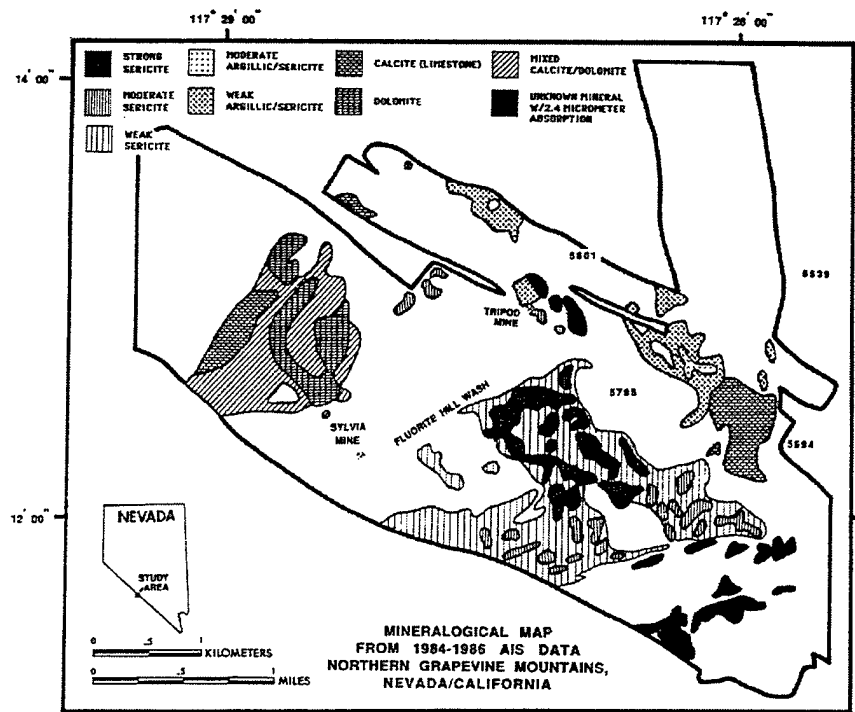


Figure 2.15. Mineralogical Map of Northern Grapevine Mountains (From Kruse, 1987)

d. Airborne Visible/Infrared Imaging Spectrometer (AVIRIS)

The Airborne Visible/Infrared Imaging Spectrometer (AVIRIS) was designed by Jet Propulsion Laboratory (JPL) with the intent of becoming the first spaceborne hyperspectral imager (Figure 2.16). The AVIRIS first flew aboard NASA's U2 and ER2 aircraft in 1987 to simulate future spaceborne operations. The normal airborne operating altitude is approximately 20 km. At this operating altitude the sensor generates a ground-swath of over 10 km (614 pixels) wide and provides a spatial resolution of nearly 20 m. The AVIRIS instrument provides coverage from $0.4 \mu\text{m}$ to $2.5 \mu\text{m}$ in 224 contiguous bands, each having a nominal bandwidth of 10 nm. AVIRIS's ability to acquire data in 224 narrow channels represented a quantum leap forward in imaging spectrometer design. This increase in spectral resolution provides a means to conduct detailed diagnostic studies of fine absorption features. The AVIRIS records the collected

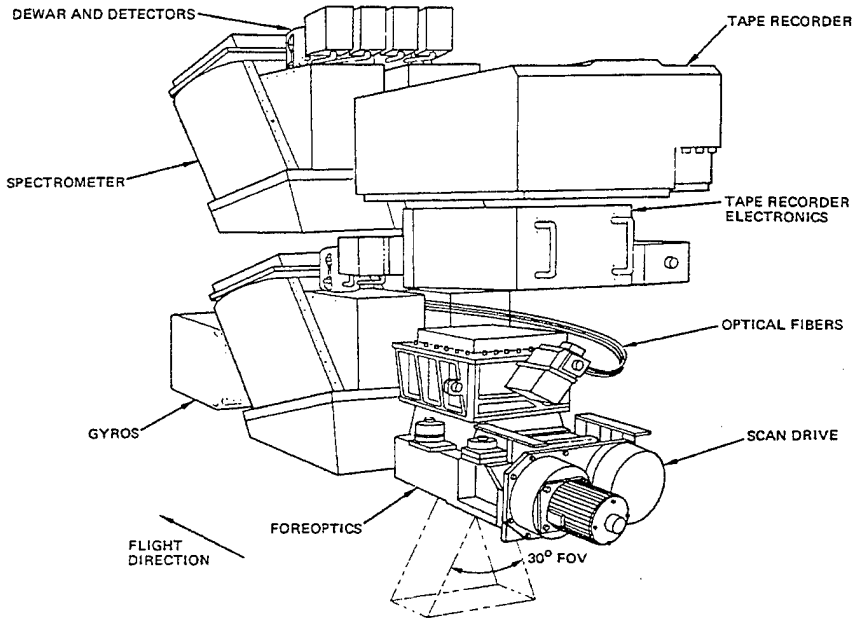


Figure 2.16. AVIRIS Sensor (From Vane, 1987)

energy on an array of discrete detectors (Figure 2.10.c), mechanically scanning the ground in a whisk broom motion. Designers improved on the earlier approach by providing four line-array detectors for each visible, NIR, and two IR portions of the spectrum, to achieve simultaneous imaging in all 224 bands (Porter et al., 1987).

In 1992, NASA conducted three overflights of Stanford University's Jasper Ridge Biological Preserve (JRBP), located along the central California coast. The intent was to collect AVIRIS data in order to discern the fractional changes in foliage and soils over the growing season. The data was obtained from the test site on June 2, September 4, and October 6, 1992, to collect a representative sample of the entire growing season. The raw image data was calibrated to apparent surface reflectance using an atmospheric scattering model and analyzed with a spectral mixture analysis technique using library endmembers. Scene observables consisted of six different types of vegetation typical of the central coast: serpentine grassland; greenstone grassland;

chaparral; evergreen woodland, deciduous woodland; and wetland. Figures 2.17, 2.18, and 2.19 show the green fractions for June, September, and October, respectively.

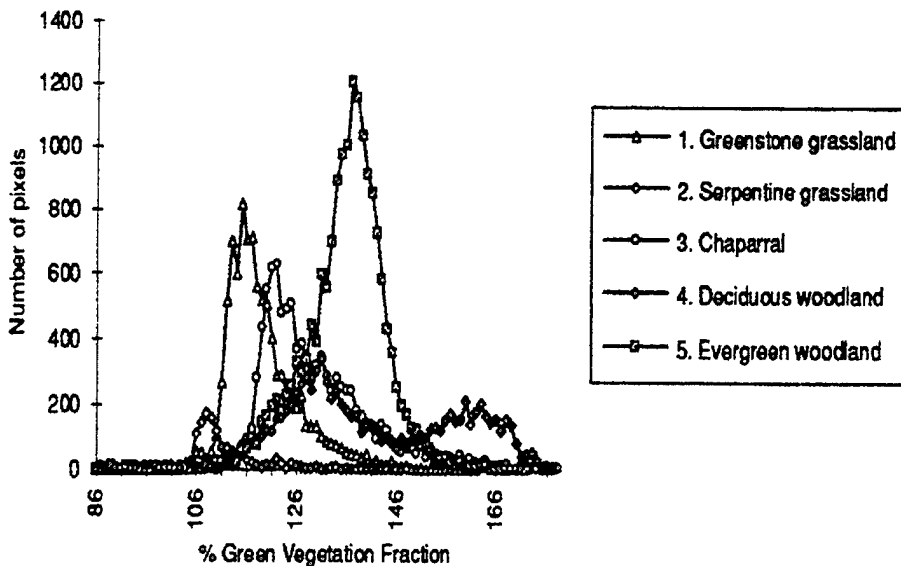


Figure 2.17. Green Vegetation Fractions for June, 1992 (From Ustin et al., 1994)

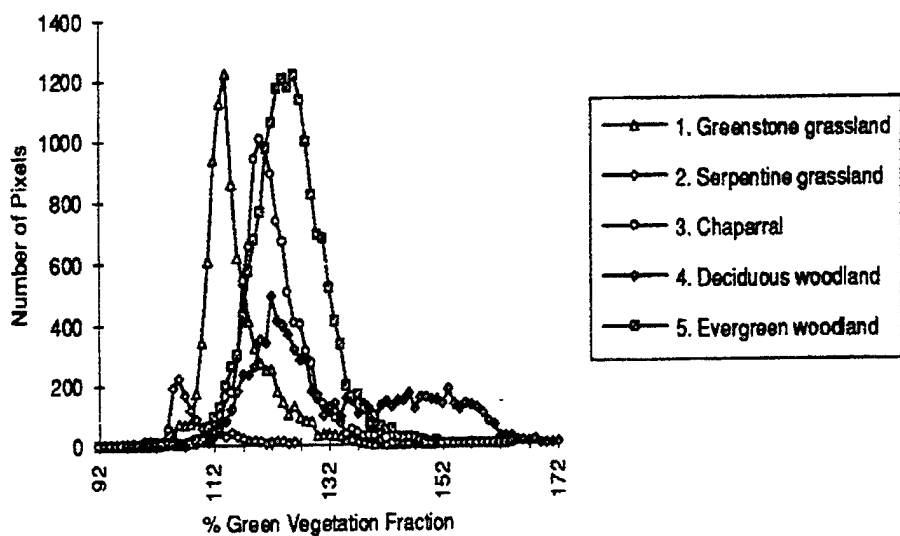


Figure 2.18. Green Vegetation Fractions for September, 1992 (From Ustin et al., 1994)

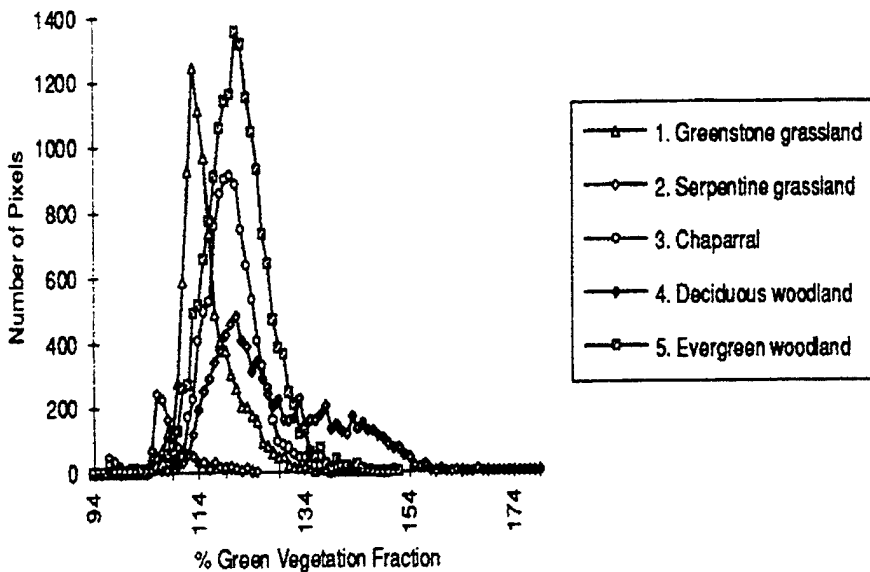


Figure 2.19. Green Vegetation Fractions for October, 1992 (From Ustin et al., 1994)

The spectral differences between plant species are readily apparent. However, the figures also show that the fraction of green vegetation decreased from June to October. These findings are consistent with the California ecosystem during the summer months. For example, the grasslands were dry during each of the collection overflights, and each figure shows a high fraction of dry grass and soil. The general pattern on all three dates shows a fractional decrease in green foliage, and a corresponding increase in dry plant and soil endmembers (Ustin et al., 1994).

This application of hyperspectral imaging illustrates the ability to detect subtle feature characteristics in a spectral signature. This investigation depicts the application of change detection and monitoring by providing information about the terrain. This capability to remotely discern information about composition and conditions of the soil and vegetation has direct military applications. Further, target detection and, hopefully, identification depends upon reliable, detailed information about the unique spectral features of a target source which differ from the surrounding background. The more imaging bands available to examine the image scene, the higher the chances are of detecting and identifying anomalous objects in a natural environment.

e. Moderate Resolution Imaging Spectroradiometer (MODIS)

The Moderate Resolution Imaging Spectroradiometer (MODIS) is the next generation of spaceborne imaging spectrometers (Figure 2.20). MODIS was designed to be deployed aboard NASA's Earth Observing System (EOS) spacecraft. MODIS will be the central instrument on board the spacecraft and is currently scheduled for launch in 1998 (Pagano and Durham, 1993). MODIS will provide broad spectral coverage in the 0.4 μm to 14.0 μm region of the spectrum. The spectral resolutions vary from 10 nm at 0.4 μm , to as much as 500 nm at 12.0 μm . The spacecraft is expected to be launched in a near-polar, sun-synchronous orbit at an altitude of 705 km. Spatial resolutions at this high altitude orbit will correspond to approximately 250 m, 500 m, and 1000 m from nadir. The MODIS instrument is expected to be launched on several EOS spacecraft to

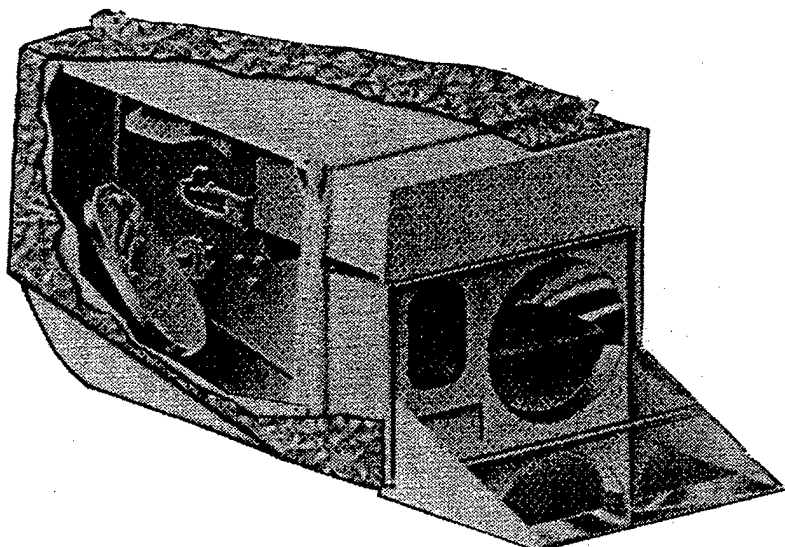


Figure 2.20. MODIS Sensor (From Pagano, 1993)

provide scientists with needed information to understand the Earth-system in enough detail to discern changes at a global scale. The relatively large spatial resolutions will

still provide sufficient dynamic range to permit the study of a wide range of land, ocean, tropospheric, and stratospheric phenomena (Panano and Durham, 1993).

f. Portable Hyperspectral Imager for Low Light Spectroscopy (PHILLS)

The Naval Research Laboratory's (NRL's) Portable Hyperspectral Imager for Low Light Spectroscopy (PHILLS) system is one of the latest imaging spectrometer to be put into operation. PHILLS is designed to record radiance data in the $0.2\text{ }\mu\text{m}$ to $14\text{ }\mu\text{m}$ region in 250 to 1024 spectral bands, each with a nominal 0.5 nm to 3 nm bandwidth. This broadband, high resolution capability is a powerful tool for resolving ambiguities in composition and distribution of reflective and thermal energy emissions. The sensor was constructed entirely from commercial off-the-shelf components, resulting in a comparatively low cost. Its imaging modules use a flat field diffraction grating which allows for the application of a spectral unmixing algorithm on raw data. The system is has no moving parts and is ruggedized for airborne operations.

The Optical Real-time Adaptive Signature Identification System (ORASIS) is also integrated with the PHILLS system. ORASIS is a data compression algorithm designed to reduce the large data rate without significant degradation to the spectral signatures. This data compression algorithm provides unsupervised, real-time endmember determination and spectral unmixing of the image scene without *a priori* information. It is capable of real-time processing because it uses a pattern recognition technique to identify spectral signatures, vice the more statistic-intensive methods like Principle Components Analysis. Its non-statistical approach facilitates target recognition of objects that do not occur frequently in the image and does not require a spectral library file of the endmembers. The algorithm produces an approximate list of endmembers that characterize the materials in the image scene (Palmadesso et al., 1995). The PHILLS/ ORASIS system is currently undergoing an operational evaluation onboard the *Predator* Unmanned Aerial Vehicle (UAV) in support of U.S. forces deployed in Europe.

4. Development Summary

Table 2.1 summarizes the growth and change in multispectral, hyperspectral, and ultraspectral imaging sensors over the last two decades. The sensors are listed in order of development and are shown here to enable the reader to compare their design characteristics.

Sensor	Bands	Spectral Range (μm)	Bandwidth (nm)	Ground Sample Distance (m)
LANDSAT MSS	5	0.5-0.6 0.6-0.7 0.7-0.8 0.8-1.1 10.4-12.6	100	79
LANDSAT TM	7	0.45-0.52 0.52-0.60 0.63-0.69 0.76-0.90 1.55-1.76 2.08-2.35 10.40-12.50	70	30
AIS I	128	1.2-2.4	9.3	11.4
AIS II	128	0.8-2.4	10.6	12.3
AVIRIS	224	0.4-2.5	10	20
MODIS	36	0.4-15.0	Varies	250,500,1000
PHILLS	250-1024	0.2-14.0	0.5-3	Varies

Table 2.1. Characteristics of Multispectral, Hyperspectral and Ultraspectral Sensors

B. EXPLOITATION SOFTWARE

Two primary software packages currently being used by the spectral imaging industry were applied here: Spectral Image Processing System (SIPS) and Environment for Visualizing Images (ENVI). Both of these imaging packages run as applications under the Interactive Data Language (IDL). In addition, the HYDICE Starter Kit is an extension of the SIPS image processing systems and incorporates an array of statistic-oriented exploitation algorithms not available in SIPS (i.e., Orthogonal Subspace Projection (OSP), Low Probability of Detection (LPD), and Constrained Energy Minimization (CEM)).

1. Spectral Image Processing System (SIPS)

The Spectral Image Processing System (SIPS) software package was developed by the Center for the Study of Earth from Space (CSES) at the University of Colorado, for the purpose of analyzing spectrometer-derived image data. The software was originally designed to support only AVIRIS and High Resolution Imaging Spectrometer (HIRIS) data sets, but had later proved itself extremely valuable in exploiting data sets from LANDSAT and HYDICE. SIPS was developed using the Interactive Data Language (IDL) and provides a wide array of user-friendly spatial and spectral analysis techniques. The SIPS software consists of three primary modules: SIPS View; SIPS Utilities; and SIPS Analysis. The SIPS View is an interactive image viewer that allows the user to analyze a given data set spatially and spectrally through a windows environment. Spectra can be extracted, displayed, and manually or automatically examined real-time using various on-line analytical tools. The SIPS Utilities module provides a capability to extract data from the storage tape, format it, to convert it from a radiance value to an apparent surface reflectance. The SIPS Analysis function is comprised of an array of programs that facilitate complete analysis of the image cube. The programs are extremely math-intensive and require an inordinate amount of CPU processing time. Most of these programs are not suited to real-time image processing or analysis (Kruse et al., 1993). The HYDICE Starter Kit was developed by HYMSMO program office to facilitate the use of SIPS, and to incorporate additional algorithms.

2. Environment for Visualizing Images (ENVI)

Environment for Visualizing Images (ENVI) is a highly sophisticated image processing system designed to view and analyze various types of remote sensing data. ENVI was also developed using IDL and incorporates an array of image processing functions in one software package. This commercial package is marketed by Research Systems Inc. Spectra extraction and processing functions are fully supported and endmember selection is available in n-dimensional space, without limitations on the number of bands. The software also includes a variety of functions that facilitate

processing of multi-frequency radar image data sets. ENVI functions provide numerous interactive processes that include a dynamic image display capability, histogram and spectral library building, automatic and manual contrast stretching, profiling, spectra extraction, image linking, and interactive scatter plot generation, to name a few. These analytical tools combine to provide an extremely powerful tool in which to analyze data spatially and spectrally. This software package was used extensively during the author's research and was found to be very user-friendly and remarkably versatile.

C. SELECTED ALGORITHMS

This investigation required the use of each software package and implemented three algorithms to obtain a per-pixel spectral response to describe the spectral relationships in the scene. These anomaly detection and classification algorithms include the Principal Component Analysis (PCA), Low Probability of Detection (LPD), and Spectral Angle Mapper (SAM).

1. Principal Component Analysis (PCA)

The PCA method is a statistical technique that decorrelates the image bands by projecting the data into a new space defined by the eigenvectors of the data covariance matrix. The purpose of the PCA technique is to examine the fundamental structure of the data in order to estimate the intrinsic dimensionality of the image cube. The transform can be applied to raw data, calibrated radiance or apparent surface reflectance data sets. The PCA image consists of an array of n spectra ($n <$ total number of image bands) at m distinct wavelengths. Experience has shown that as few as three eigenvalues can account for over 90% of the total variance in a scene, reducing a large number of wavelengths to a nominal three-parameter data set. This reduces the inherent dimensionality of the data and in principle eliminates the substantial redundancy in any given hypercube. This technique provides a basic understanding of the data properties, and can reduce the total volume of data viewed. The principal component bands are oriented from highest to lowest percentage of variance within the image scene (Richards, 1995).

2. Low Probability of Detection (LPD)

The LPD method is a statistical-based scene-dependent anomaly detection technique. The LPD technique is a variant in the general class of Orthogonal Subspace Projection (OSP) operators (Harsanyi and Chang, 1994). This technique creates a projection operator which contains the majority of the scene eigenvectors. In practice, this is done by means of a principal component transform, establishing the primary eigenvectors which define the scene's total variance. (Fifteen eigenvectors were used in the work shown here). The OSP operator thus constructed, in combination with a known target spectrum, can be used to estimate the target abundance in each pixel. Theoretically, most any spectrum not contained in the “background” eigenvector set will be brought out with this technique (Farrand and Harsanyi, 1995).

3. Spectral Angle Mapper (SAM)

The SAM algorithm takes advantage of spectral similarities shared between an endmember and each test pixel in the image cube. This method is a statistical technique that calculates the angle (Θ) between the target and test spectra, with complete indifference to their relative brightness values. The SAM calculates the angle by treating each spectra as a vector and applying equation 2.1:

$$\Theta = \arccos \left[\frac{\bar{\mathbf{t}} \bullet \bar{\mathbf{r}}}{\|\bar{\mathbf{t}}\| \bullet \|\bar{\mathbf{r}}\|} \right] \quad (2.1)$$

where \mathbf{r} is the endmember spectra, and \mathbf{t} is each of the test spectra. The algebraic result represents the angular difference between the selected endmember and pixel spectra. Figure 2.21 graphically illustrates how an endmember and test spectra are plotted in two dimensions with their values for band 1 and band 2. The angle is measured in units of radians and range from 0 to $\pi/2$. Small spectral angles correspond to materials of high

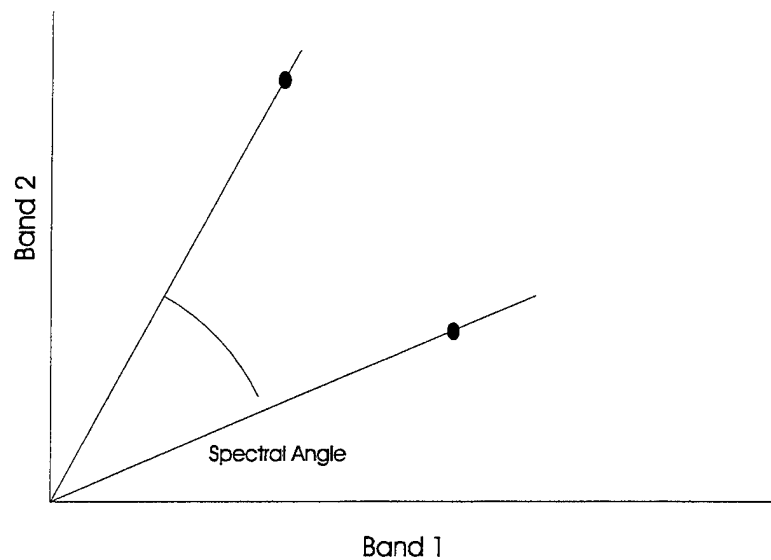


Figure 2.21. Two Spectra Plotted For Bands 1 and 2

similarity, and are displayed as brighter gray levels. Larger angles indicate less similar spectra, and are shown in darker gray levels.

III. MILITARY APPLICATIONS

A. CLASSES OF APPLICATIONS

Military commanders must be prepared to operate at each of the three levels of warfare - Strategic, Operational and Tactical. The trend in ultraspectra, hyperspectral, and multispectral imaging technologies is toward increased ability to discern an adversary's capabilities and possible intentions to support planning and operations at any level.

1. Strategic Level

Strategic intelligence relates to evaluated information used in the formation of national and international strategy, policy, and military plans (U.S. Joint Chiefs of Staff, 1995). At this level of warfare focus is placed on identifying an adversary's capabilities and intentions to support senior civilian and military decisionmakers. Nationally oriented imagery requirements are not considered time-sensitive and typically do not necessitate high quality spatial resolution to be useful to the decisionmaker. It is for these reasons current multispectral imaging programs (i.e., the U.S. LANDSAT and the French SPOT - - Satellite Probatoire d'Observation de la Terre (Exploratory Satellite for Earth Observation)) that provide broad-area coverage and moderate spatial resolution can have a potential strategic applicability. For example, LANDSAT and SPOT imagery can provide information to assist governmental agencies in responding to natural disasters such as floods, volcanic eruptions, and forest fires. Figure 3.1 illustrates this capability by comparing a true color image and a multispectral false-color image of an area burned near Malibu, California in 1993. The orange-red area in the bottom LANDSAT composite (bands 7-4-2) image depicts the region most affected by the fire.

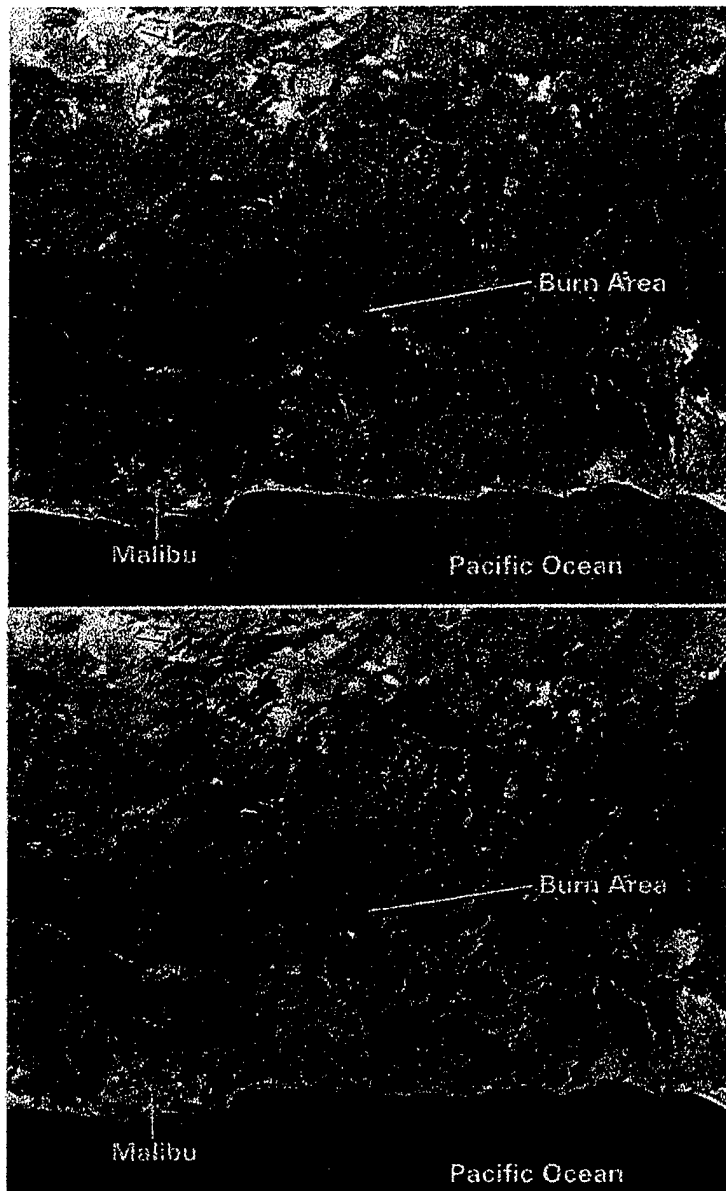


Figure 3.1. Malibu, California Fire Damage Assessment (From MUG, 1995)

2. Operational Level

Operational intelligence relates to information required for planning and executing major operations within a theater to accomplish the strategic objectives (U.S. Joint Chiefs of Staff, 1995). At this level of warfare focus is placed on the collection, identification, location, and analysis of an adversary's centers of gravity. Operationally oriented

requirements necessitate a detailed analysis of information to identify critical vulnerabilities, and to assist the commander in making decisions concerning the optimal use of force. For instance, LANDSAT and SPOT satellite images provided U.S. Navy planners with information on the water depths off the coast of Kuwait prior to the Persian Gulf War. This information was fully integrated into the planning of the intended U.S. amphibious operations. Figure 3.2 illustrates this capability for the waters near Bandar Abbas, Iran. The light blue color indicates shallow water areas and the dark blue shows the deeper regions.

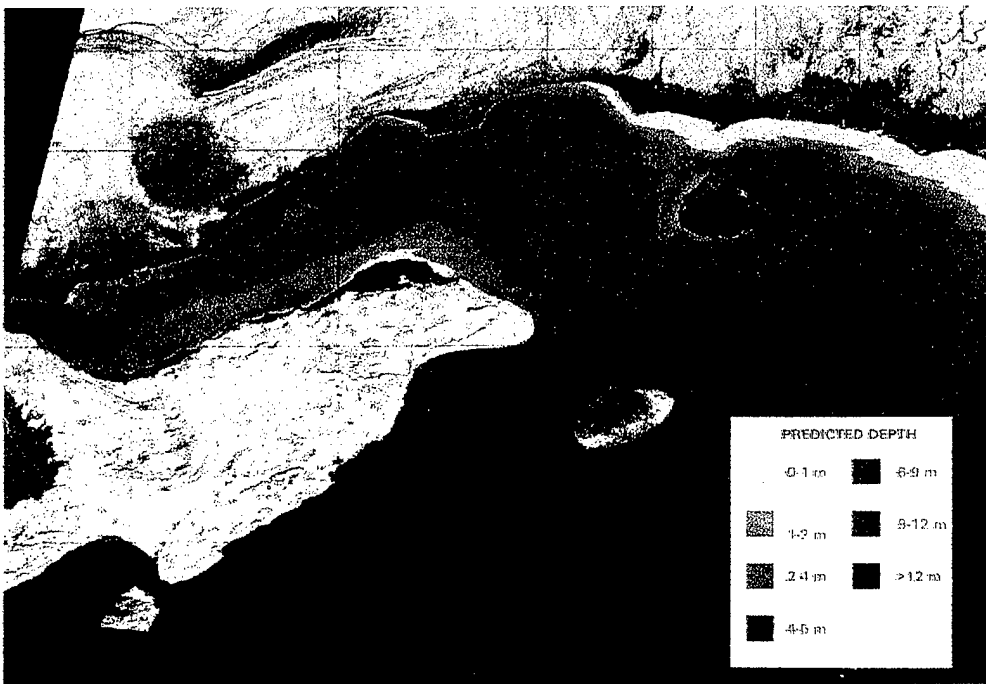


Figure 3.2. Bathymetry Image of Bandar Abbas, Iran (From MUG, 1995)

3. Tactical Level

Tactical level information is required for the planning and execution of tactical operations at the component level (U.S. Joint Chiefs of Staff, 1995). Tactical intelligence is oriented towards discerning the capabilities and immediate intentions of a potential adversary. Figures 3.3 and 3.4 illustrate a tactical application of spectral imaging

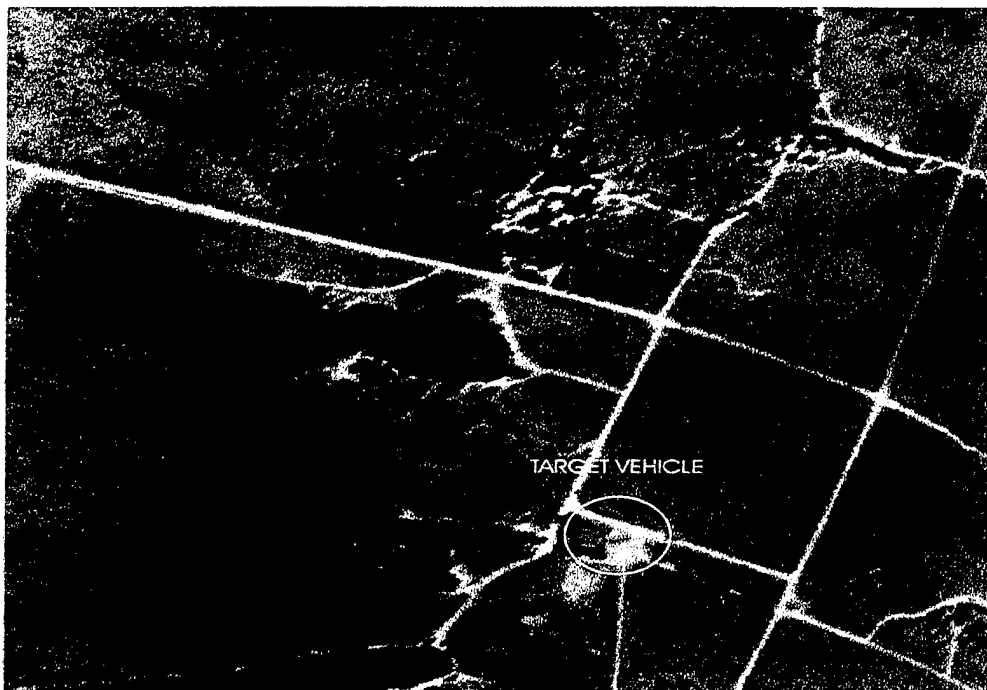


Figure 3.3. True Color Image of a Military Vehicle (From MUG, 1995)

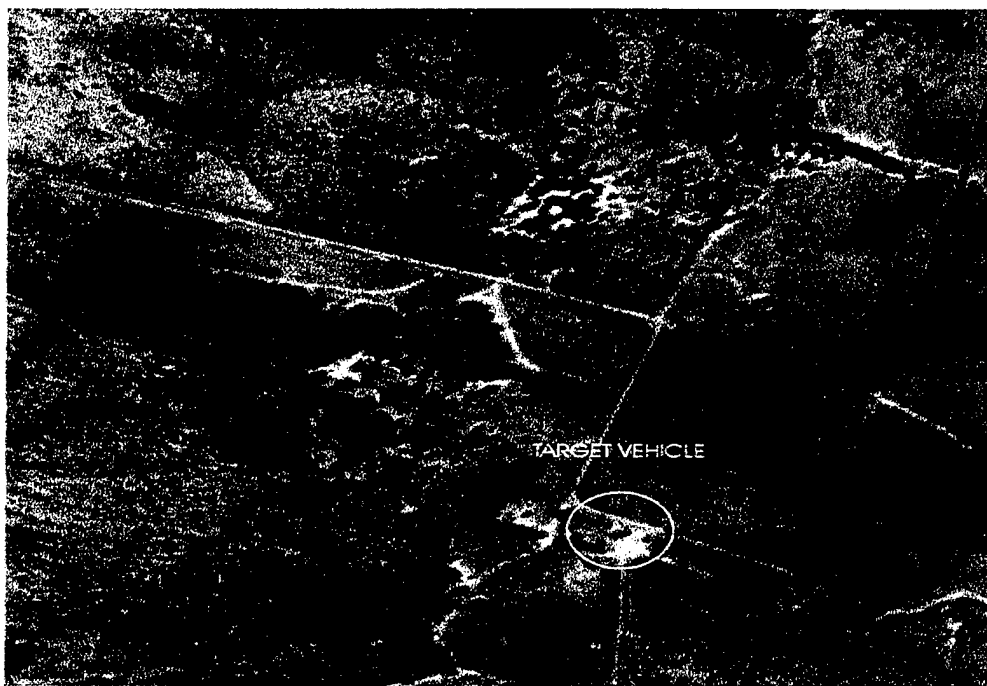


Figure 3.4. Multispectral Image of a Military Vehicle (From MUG, 1995)

by comparing the discrimination capability of panchromatic and multispectral images. In Figure 3.3, for example, the vehicle does not standout against the surrounding background. The opposite of which is true for the multispectral composite image (Figure 3.4).

B. TACTICAL UTILITY

More than at any other level, U.S. warfighting capability is predicated on the timely delivery of processed image data to the tactical commander. Marshall [1994] quotes General Norman Schwarzkopf, commander of the coalition forces during the war, as commenting to the Senate Armed Services Committee on the shortfalls of U.S. tactical reconnaissance capabilities:

One of the shortcomings we found is that we just don't have an immediate responsive intelligence capability that will give the theater commander near-real-time information that he personally needs to make a decision.

The rigorous pace and intensity of present-day combat operations has caused the military to seek out new, highly sophisticated reconnaissance, surveillance, and target acquisition technologies. Today's U.S. precision guided munitions require timely, detailed, accurate targeting information for optimal employment. Some recent successes in the area of hyperspectral research have provided significant advances in improving our ability to view the battlefield.

1. Gulf War Problem

One of the more vexing problems our military leaders faced during the Persian Gulf War was the detection and destruction of Iraq's mobile SCUD launcher inventory. Figures 3.5 and 3.6 are photographs of a Transportable Erector Launcher (TEL) and its associated SCUD ballistic missile. The majority of the missiles were fired from pre-surveyed launch positions located in west and southwest Iraq - an area spanning

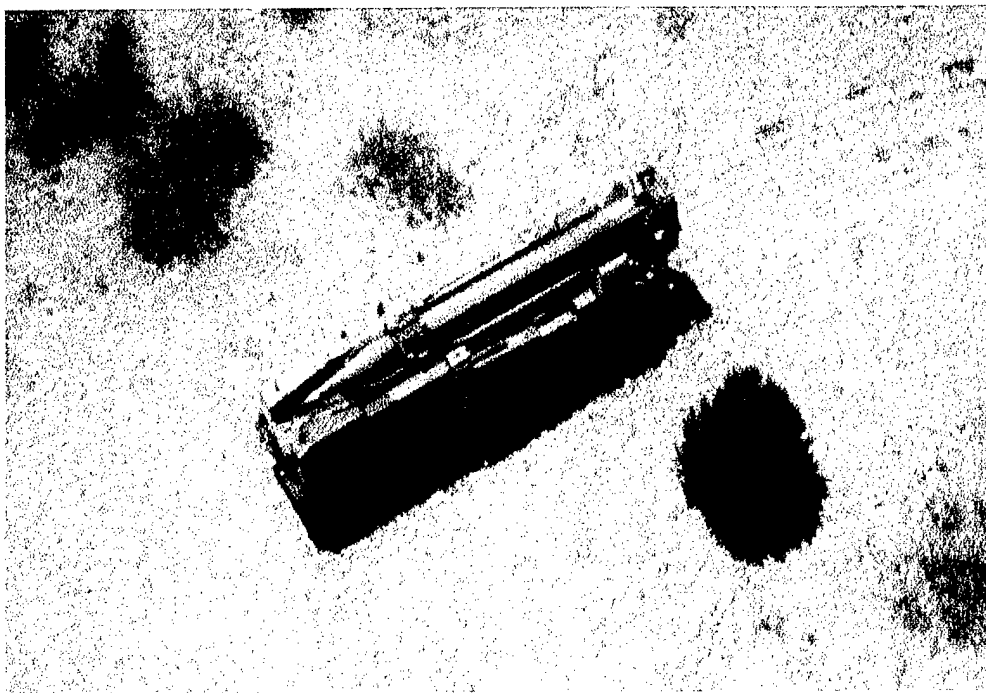


Figure 3.5. Mobile TEL and SCUD Missile (Courtesy of TRW, 1995)

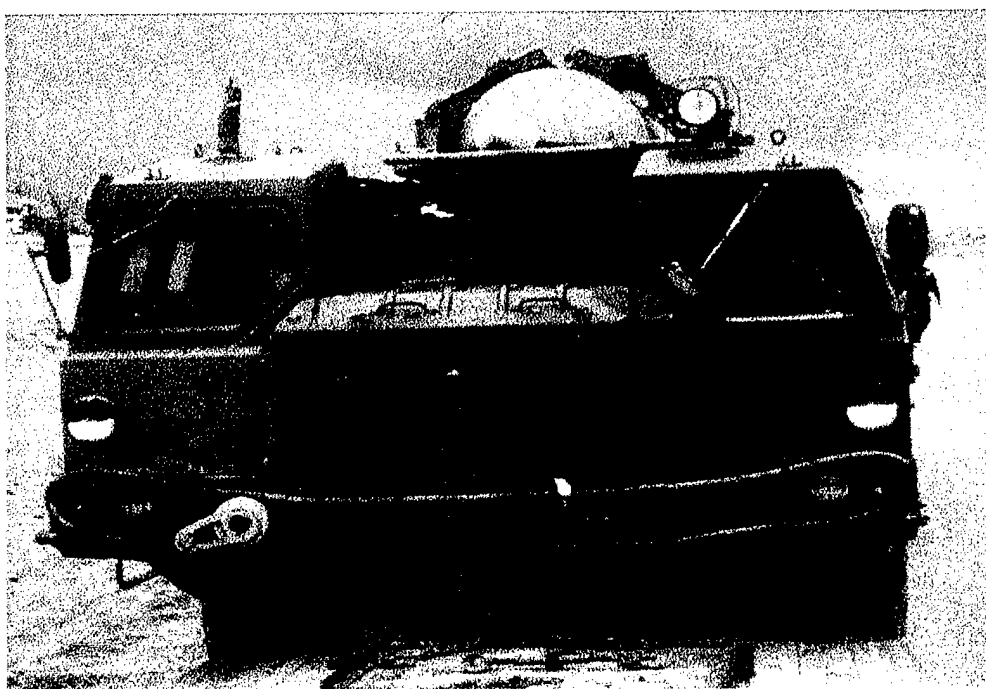


Figure 3.6. Mobile TEL and SCUD Missile - Front View (Courtesy of TRW, 1995)

thousands of square miles. These launch sites were typically located in rugged terrain where SCUD crews could easily conceal themselves before and after a launch. Typically, launch crews would seek cover from coalition reconnaissance assets by hiding under camouflage netting or in ravines and coverts. SCUD suppression efforts were a high priority mission throughout the conflict. As more intelligence resources were brought to bear on the SCUD problem, analysts were able to reconnoiter some suspected operating areas. Most of these search areas were extremely large so target detection remained a daunting challenge. Initial counter-SCUD efforts were regarded as successful, but post-war reports have cast doubt on the actual number of missiles destroyed. It's been suggested that some of the missiles reportedly destroyed may have been large trucks or decoys constructed of a hollow cardboard material.

2. Lessons Learned

Lessons learned from this experience tells us that future tactical reconnaissance and surveillance systems must be in sync with the operation. A firm link between the mission and the supporting system needs to be established if intelligence is to be responsive to the situation. An imperative to the SCUD problem is the timely detection and destruction of the TEL. Figures 3.7 and 3.8 compare the ability of panchromatic and hyperspectral images to detect the presence of a SCUD system in a natural desert environment. While the SCUD is not easily discernible in the panchromatic image, it is clearly noticeable in the spectral composite image. A TEL can travel approximately nine miles in any direction within fifteen minutes after firing. This localization problem was further exacerbated by our inability to quickly re-orient national-level imagery assets upon demand. The lack of tactical control over these assets hindered our ability to respond to the problem at the speed and detail required. Theater-level assets like the U2 reconnaissance aircraft was also deployed in response to the detection problem, but it lacked the level of tactical reporting capability needed. Military planners require an intelligence architecture that will enable TEL destruction within 10 minutes of detection,

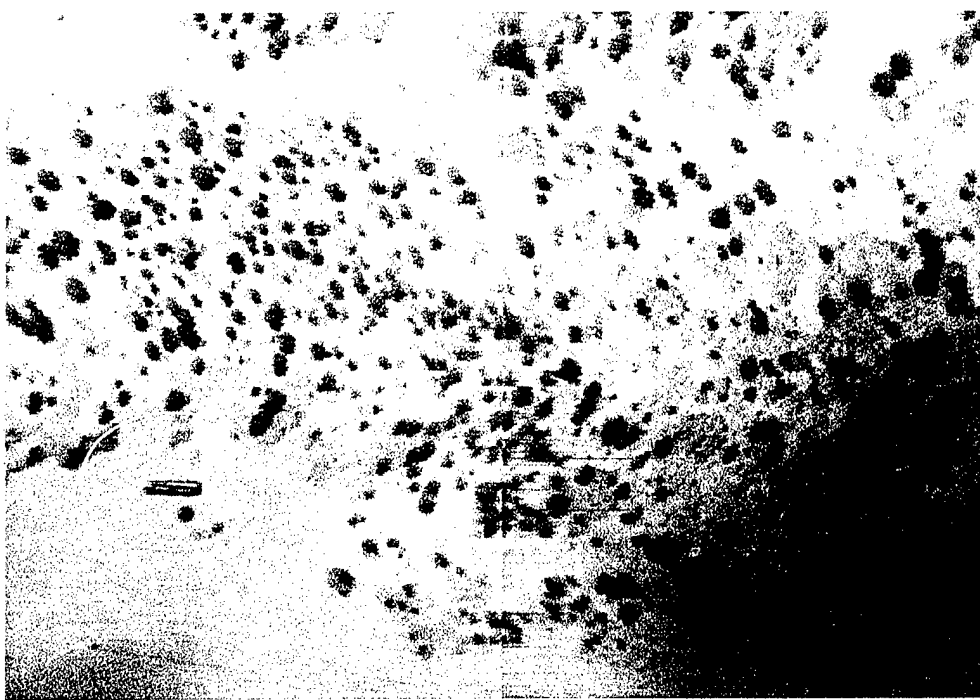


Figure 3.7. True Color Image of a TEL and SCUD Missile (Courtesy of TRW, 1995)

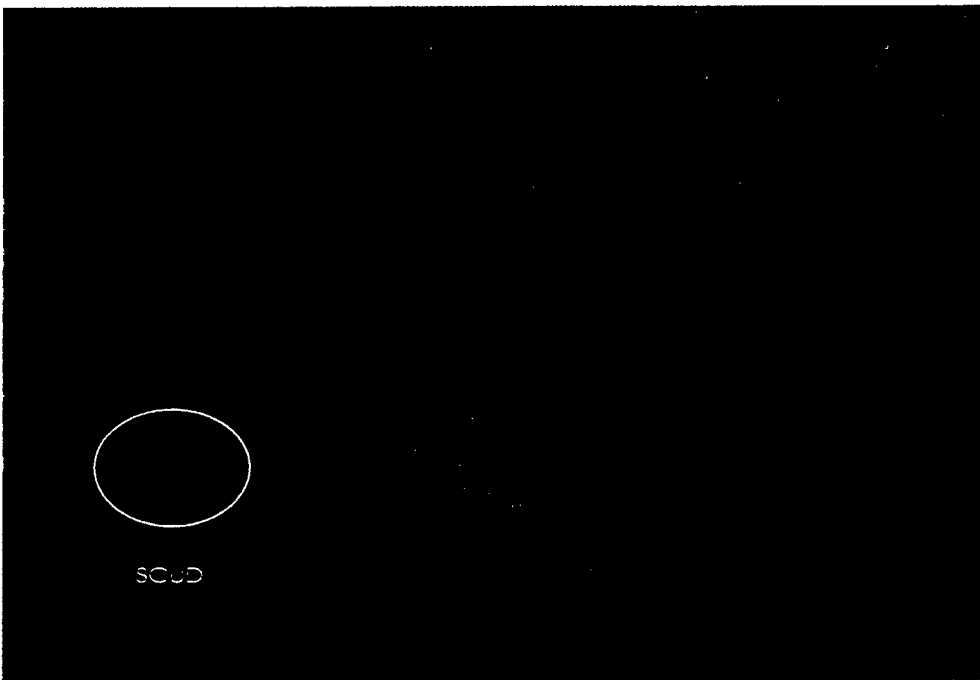


Figure 3.8. Hyperspectral Image of a TEL and SCUD Missile (Courtesy of TRW, 1995)

and targeting accuracy is essential. One of the most important lessons learned from the was the operational need for a family of UAVs to attack the problem.

3. Current and Future Capabilities

One of the primary challenges the HYMSMO program faces is providing timely support to the warfighter using a technology that was not specifically designed to satisfy tactical requirements. The technology validation phase of the program is well underway, and early findings show the technology to be very versatile. Recent findings indicate that a future capability to autonomously detect and geolocate military relevant tactical targets in various types of background clutter in near-real-time is feasible.

a. Application Examples

A major advantage of hyperspectral imagery data is the capability to record reflected solar energy beyond the visible portion of the spectrum. A quantitative measure of its military benefits can be found by examining the spectral signatures of camouflage materials relative to a natural vegetative background. Figure 3.9 is an

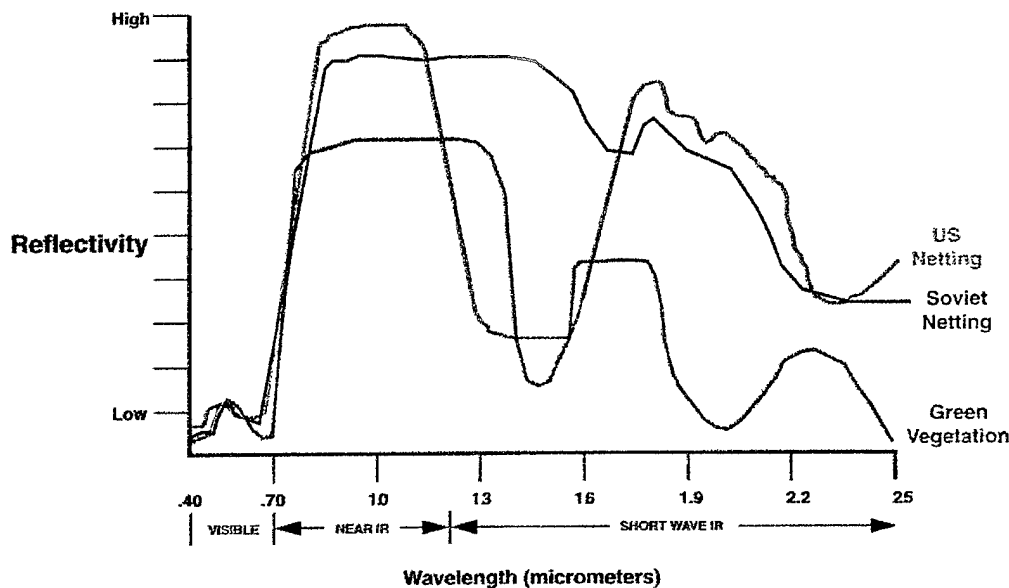


Figure 3.9. U.S. and Russian, Camouflage and Green Vegetation (From MUG, 1995)

example of how hyperspectral imagery can defeat U.S. and Russian woodland camouflage netting deployed in a healthy green vegetative environment. Camouflage is considered to be a form of concealment created through artificial means. Its purpose is to break up the outline of an object and make it indistinguishable from the background environment. In the visible region of the spectrum the camouflage netting and healthy green vegetation are almost identical. In the NIR and SWIR regions, however, the spectra of the man-made materials and natural vegetation differ dramatically. Figures 3.10 and 3.11 are 5 m GSD panchromatic and multispectral images of five camouflaged objects. Note that the camouflaged objects are easily detected in the multispectral image, shown here in red, but are not as obvious in the true color image.



Figure 3.10. Panchromatic Image of Camouflage Netting (From MUG, 1995)

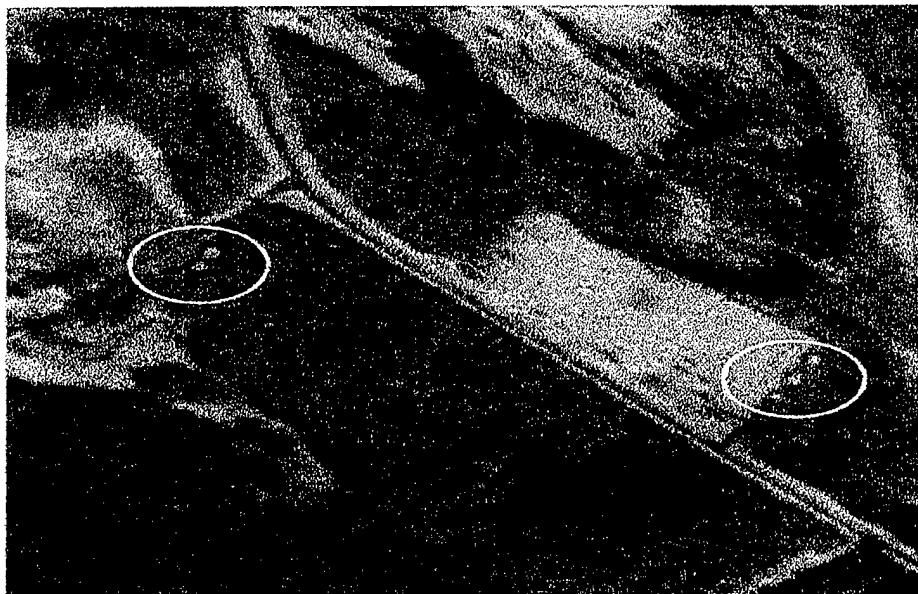


Figure 3.11. Multispectral Color Image of Camouflage Netting (From MUG, 1995)

Hyperspectral data is also sensitive to changes in the moisture content of soil and natural vegetation. The changes can be used to detect stress caused by lack of water, disease, or disturbances caused to the terrain. When a vehicle traverses over soil, sand, or grass, the terrain is disturbed. Depending on the type and condition of the soil and foliage, both mechanical damage to the plants and the overturning of the underlying soil will contribute to the spectral signature. Figure 3.12 compares the spectra of stressed, severely stressed, and healthy vegetation samples. The detection of stressed vegetation and disturbed earth can provide evidence of a potential adversary's movement, and give insight to their intentions. Other military examples of stressed plant life are that cut vegetation is sometimes used to conceal tactical vehicles, and stresses caused by disturbances to the ground can be an indication of sub-terrestrial construction.

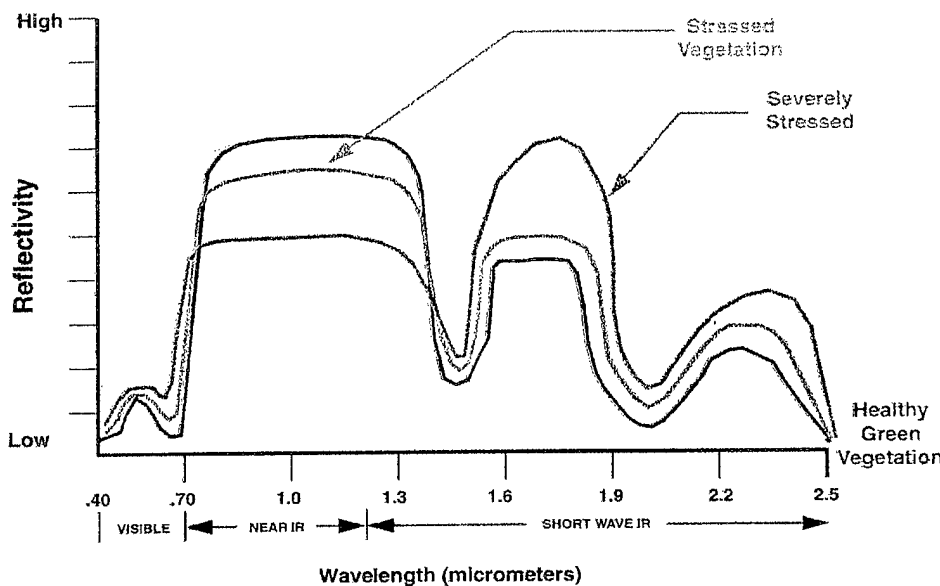


Figure 3.12. Severely Stresses, Stressed, and Healthy Vegetation (From MUG, 1995)

There are a number of hyperspectral applications which support military operations being used today. These additional applications provide a representative example of several military related uses of ultraspectral, hyperspectral, and multispectral image data sets. Below is a list (not all inclusive) of these potential applications:

- Target/Decoy Discrimination
- Change Detection
- Bathymetry
- Image Map Supplements
- Mission Planning
- Perspective Views
- Terrain Categorization
- Disaster Assessment and Relief Assistance

b. Cross-Cueing

Autonomous cueing is the passing of detection, geolocation, and targeting information to another sensor or target acquisition system without a human interface. For cross-cueing to be effective, each sensor must be able to autonomously alert another

sensor to the presence of a target of interest. Each sensor needs to leverage from the other sensor's unique strengths to provide economy of effort and to enhance the overall system's detection capability (Marshall, 1994). By incorporating more than one sensor into a single reconnaissance platform we can exploit the individual strengths of a sensor while minimizing its weaknesses. For example, consider an airborne collection platform carrying both a Signals Intelligence (SIGINT) system and a panchromatic imaging sensor. A SIGINT system can provide timely indications and warnings (I&W) information over a broad geographic region, but can give only rough locating data until multiple intercepts can be gained. An imagery system can provide very accurate geolocating data, but is typically limited to a small geographic area. By working in concert the SIGINT system can pass rough geolocating data to the imager so the optics can be trained to the specific area of interest. The addition of a hyperspectral system (with automated procedures like ORASIS) can provide a spectral dimension to the overall system to increase the detection and identification capability of the system.

c. Automatic Target Recognition

One of the key components to be used on future hyperspectral systems is an automatic target recognition system. Extensive research is being conducted on the use of automatic target detection and identification techniques to reduce the analyst's workload and increase target detection speed. At present, however, automated target detection capabilities are restricted to the research and development arena and have only recently been employed in operational practice. The goal here is to remove the human from the process of target recognition, while increasing the performance of the functions to real-time. Automation is desirable because most systems that have a human element in the loop are generally slow and potentially unreliable in dealing with real world problems. The military relevant target sets currently being evaluated consist of tanks, TELs, trucks, armored personnel carriers, etc. This ability to automatically process raw hyperspectral data also has the potential for reducing the amount of data transmitted to the tactical commander, thus improving upon the timeliness of the information. At this stage of

development it remains unclear if current data transmission capabilities will support wide area surveillance.

d. Tactical Support Platform

The best quantitative measures for assessing the tactical utility of hyperspectral imagery is timeliness. One of variables affecting the timeliness of remote sensing imagery is product delivery time. The image delivery time refers to the time it takes to collect, exploit, and deliver finished imagery to the tactical commander. Collection timeliness is directly correlated to the revisit frequency of the collector. The more frequent the revisit time the faster the information can be provided to the warfighter. The revisit frequency of current multispectral satellite systems to over-fly the same point on the earth can take upwards of days. The actual delivery time of the final imagery product can take nearly a week. During Desert Storm, for example, LANDSAT images were delivered to the theater commander between five and twelve days after a request was submitted (U.S. Joint Chiefs of Staff, 1995).

Technological advances in UAVs presents an attractive alternative to the space-based reconnaissance and surveillance assets. The Medium Altitude Endurance (MAE) UAVs can give near-continuous, on-demand situational awareness of the battlefield. The MAE UAV is designed to provide a long range, extended dwell capability to satisfy the reconnaissance and surveillance mission requirements. The Predator vehicle has demonstrated an endurance of 40+ hours and currently has a Ku-band data link for SATCOM operations. UAV payloads currently include electro-optical (EO) and infrared (IR) imagers, foliage penetrating radars, communications links, and support only limited onboard processing capabilities. There is an initiative underway to optimize the Predator MAE UAV to carry a variety of advanced sensor suites. The Predator program is presently evaluating technologies such as the PHILLS ultraspectral sensor, SIGINT and LASER designator/ranging systems, and advanced communications packages for future deployments. Figure 3.13 illustrates the Predator's concept of operations.

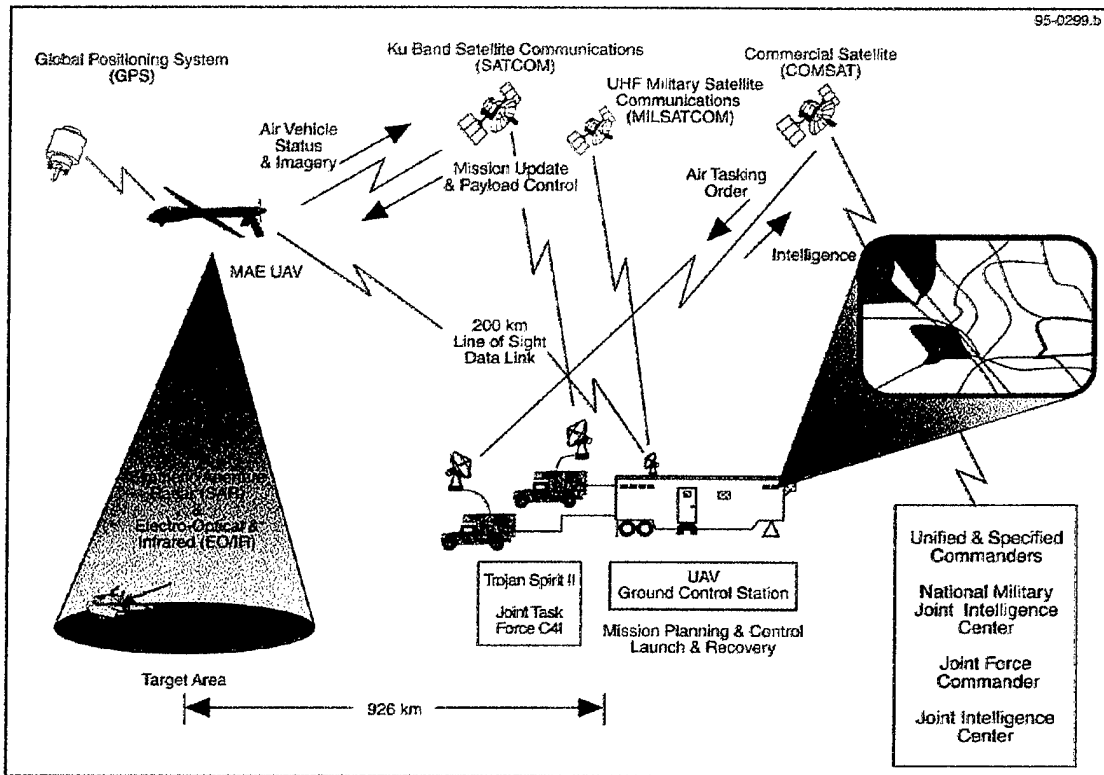


Figure 3.13. UAV Concept of Operation (From Unmanned Aerial Vehicles, 1995)

IV. EXPERIMENT DESCRIPTION

A. GENERAL METHODOLOGY

The HYMSMO program office is conducting a series of applied remote sensing experiments during FY-94 through FY-98 designed to demonstrate the capability of hyperspectral spectrometers and exploitation techniques to satisfy time-sensitive intelligence requirements. To that end, collection and exploitation experiments are designed to examine the physics and phenomenology of various military target classes under different environmental conditions.

1. Levels of Information (LOI)

These time-sensitive SMO requirements, termed “Levels of Information” (LOIs), were identified through a Defense Intelligence Agency (DIA) sponsored survey known as Assured Support to Operational Commanders (ASOC). LOIs evaluated with respect to the Forest Radiance collection and exploitation experiment are comparable to those requirement levied on other types of intelligence gathering platforms. These vetted SMO requirements include spectral characterization (CH), detection (DE), geolocation (GE), classifying (CL), discriminating (DI), identifying material (MI), and quantifying materials (QM) of mobile and fixed objects and decoys in progressive states of concealment. Spectral Taggants (TG) is another LOI category (not originally identified in the survey) being examined to determine if a spectrally tagged target object can be discriminated from an object that has not had the material applied to it (Anderson, 1995).

2. Guidance

HYMSMO experiments leverage from existing spectroradiometric programs and data sets in order to assist designers in maximizing collection opportunities and defining their objectives. The following experimental objectives were defined for FY-95 program:

- “Design experiments that address high priority Levels of Information (LOIs) which provide a technical basis for the HYMSMO collection and exploitation program;
- Refine ground- and sea-truth protocols to support HYMSMO experiments;
- Understand airborne sensor characteristics and performance requirements relative to military targets and backgrounds;
- Exercise and improve non-linear exploitation algorithms, models, software, techniques, and measures of effectiveness (MOEs) for utility assessments;
- Develop error propagation techniques to design experiments and predict performance; and
- Quantify and demonstrate the potential military utility of hyperspectral imagery data in support of time-sensitive military operations, as well as critical intelligence applications.” (Anderson, 1995)

B. OPERATION FOREST RADIANCE I

Operation Forest Radiance I was the third in a series of HYMSMO program-sponsored collection and exploitation experiments. The intent was to expand upon the knowledge and experience gained from the Desert Radiance I and II experiments, conducted in CY-94 and CY-95. As their names suggest, Forest Radiance I was conducted in a woodland environment, whereas the Desert Radiance experiments were conducted in a desert setting.

1. Background

The Desert Radiance I experiment was conducted in October, 1994, at the U.S. Army’s White Sands Missile Range in New Mexico (NM). This operation placed its highest priority on examining completely exposed mobile objects, with subsidiary emphasis on fixed objects and geographic features. The Desert Radiance II experiment was conducted in June, 1995, at the U.S. Army’s Yuma Proving Grounds in Arizona

(AZ). Here, fully exposed mobile and fixed objects were examined, but research was expanded to include the analyses of camouflage, concealment, deception, and spectral taggants. The Forest Radiance I experiment was conducted in August, 1995, at the U.S. Army's Aberdeen Proving Grounds in Maryland (MD). The intent here was not only to emphasize the spectral analyses of these same target classes, but to expand the scope to explore progressive states of concealment (exposed, shadowed, concealed) and camouflage conditions. The Forest Radiance I operation was the program's first attempt at examining the non-linear effects caused by shadow and natural canopies.

2. Airborne Data Collection Objectives

The Forest Radiance I tests were staged exclusively at the Aberdeen Proving Ground's H-Field from 17 to 31 August 1995. The H-Field range proved to be an ideal physical environment to satisfy all of the experiment's priority LOIs. Other targets of opportunity were available at the range included the U.S. Army Tank Museum and a hazardous waste disposal area (Superfund Site); however, overflights of the Superfund target was removed from the collection plan due to the safety concerns expresses by the H-Field Control Center. Prior to executing the plan, collection guidance and direction was promulgated via the Forest Radiance I Collection and Exploitation Operations Plan (CEOP-3). Secondary collection efforts were conducted against urban areas in Washington, D.C. (U.S. Capital Building) and Baltimore, Maryland (3 sites). The Washington D.C. area provided the necessary data to examine the rich material diversity of an urban environment. The Baltimore site provided a waterfront setting, in addition to urban data, to further explore material identification and spectral tagging techniques. For additional information concerning this portion of the experiment, refer to URBAN RADIANCE I CEOP-5. As a complement to these spectrometer overflights, national-level collection assets were also tasked to support the experiment's objectives.

3. H-Field Site Description

The H-Field Range is located on Edgewood Peninsula approximately 20 miles northeast of Baltimore, MD. The H-Field setting provided three distinct environments in which to deploy the target arrays: 1) a large open field, to deploy a total of 77 completely expose military vehicles and target panels; 2) a road adjacent to both the field and wooded treeline, to ease target re-deployment and facilitate exploring the non-linear effect due to shadow; and 3) a woodland forest, to evaluate the effects caused by partially concealed objects under canopy. Figure 4.1 shows the location of the Aberdeen Proving Ground's H-Field Range. Figure 4.2 shows the flight-path used by the aircraft, which

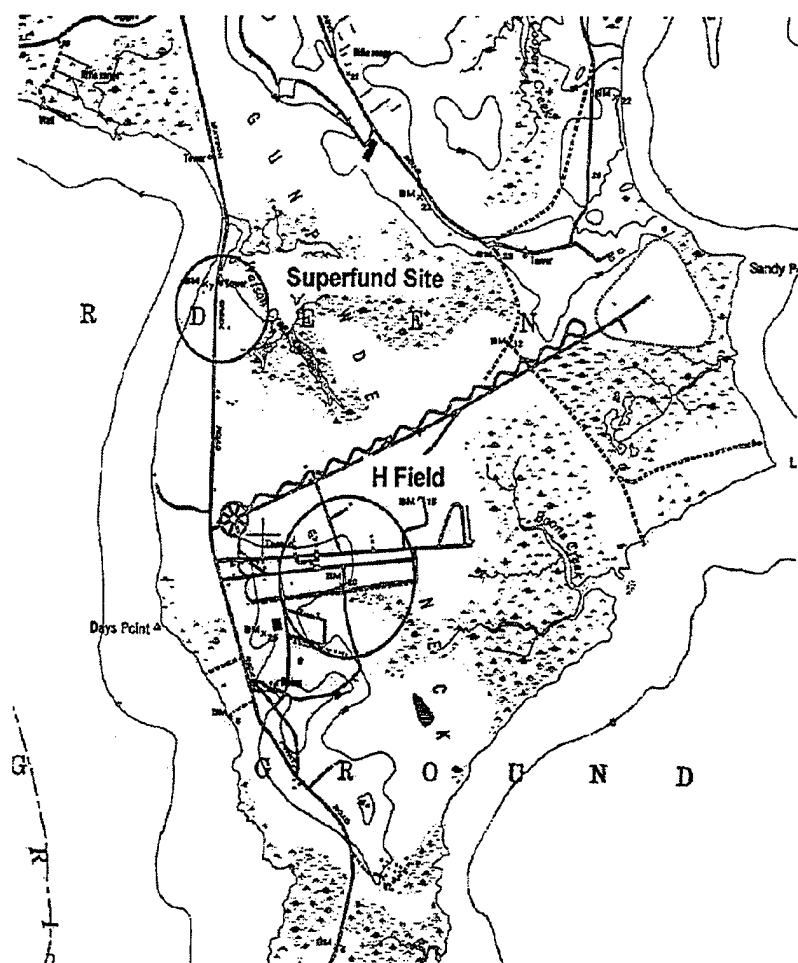


Figure 4.1. Edgewood Peninsula (From Anderson, 1995)

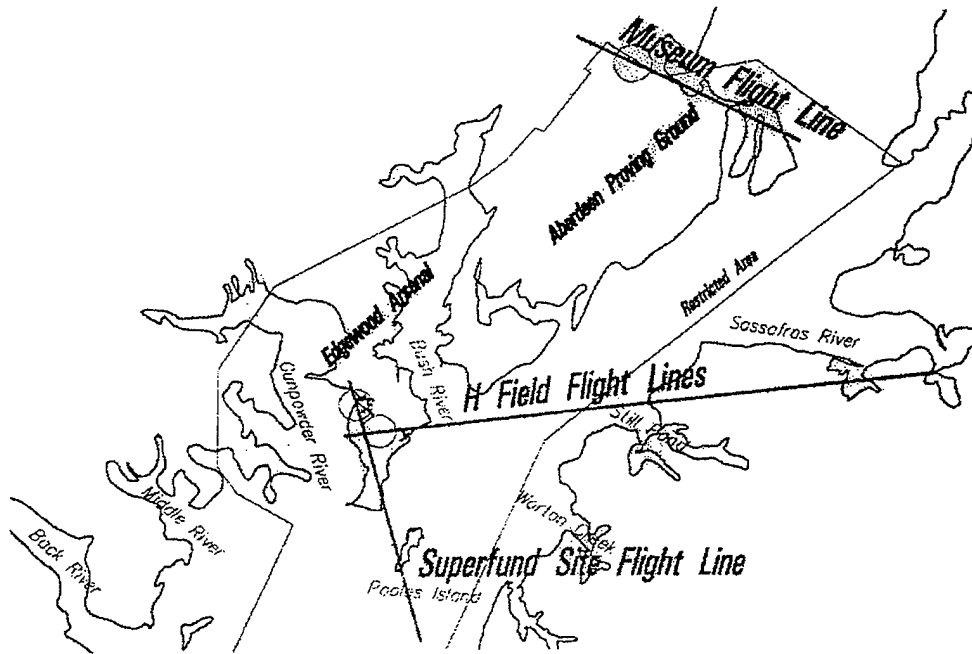


Figure 4.2. Forest Radiance I Flight Lines (From Anderson, 1995)

consisted of a 20 mile ingress/egress and 3 mile of target array. This figure also shows the flight-line for other target areas at the Aberdeen Museum (canceled) and Superfund Site (canceled).

4. Experiment Design

The H-Field site was specifically selected to provide a realistic forest environment to satisfy five priority LOIs identified for exploitation (e.g., spectral characterization, material identification, subliteral detection, time quantification, and spectral taggants). H-Field was ideally suited to this experiment because both mobile and fixed objects could be deployed in exposed, shadowed, and canopy areas at a single location. The experiment was executed in three separate phases, each employing a progressive state of concealment. The first phase, Phase I, emphasized a suite of overtly exposed vehicles, decoys, and target panels. In Phase II, the observables were re-deployed to the shadowed area adjacent to the treeline. In Phase III, the objects were again re-deployed under

canopy for partial concealment. The target classes and site configurations for each phase are listed in Table 4.1, and are discussed in detail in the ensuing sections. Throughout the experiment target spectra, illumination effects, and atmospheric depth were evaluated at three altitudes (5,000, 10,000, and 20,000 ft) and varying sun angles (mid-morning, local noon, mid-afternoon). Varying the overflight altitudes provided a range of subpixel and multipixel data sets, which were comprised of a mixture of target and background material radiance spectra.

Target Type	Site Configuration	Phase
Material Panels	Exposed w/uniform background	I
	Partial shadow w/variable background	II
	Partial to full concealment w/forest canopy	III
Vehicles / Decoys	Exposed w/uniform background	I
	Partial shadow w/variable background	II
	Partial to full concealment w/forest canopy	III
Camouflage Defeat	Camouflage with / without vehicles	I
	Reference materials under camouflage	II
Calibration Panels	Exposed w/uniform background	I, II, III
Downed Pilot	Parachutes in trees	I, II, III
	Downed pilot simulation	I
Stressed Vegetation	Tank track w/uniform high grass	I, II

Table 4.1. Forest Radiance I Experiment Summary (From Anderson, 1995)

a. Target Objects

A variety of reflectance calibration targets were deployed to aid radiance calibration to apparent surface reflectance. These calibration panels, summarized in Table 4.2, provided a spectrally near-homogeneous medium in which a baseline spectral library could be established. This spectral database also provided a useful reference for the non-linear exploitation techniques explored during Phases II and III. Tables 4.3 through 4.5 summarize the target materials used during Phase I of the experiment. The spectral signatures extracted from these overtly exposed target objects were also used to exploit the data sets from Phases II and III. Tables 4.6 and 4.7 describe the vehicle, decoy, and camouflage target arrays deployed during all three of the phases. Using both

Target ID	Size meter (m)	Description
R1	9.1 X 9.1	2% reflectance
R2	" "	4% "
R3	" "	8% "
R4	" "	16% "
R5	" "	32% "
R6	" "	64% "
S1	" "	Type 1 spectral reflectance, 48% gray R5
S2	" "	Type 3 spectral reflectance, 100% cotton
S3	5.2 X 15.2	Type 4 spectral reflectance, green fabric w/polyethylene overlay

Table 4.2. Calibration Panels (From Anderson, 1995)

Target ID	Size (m)	Description
F2a	3 X 3	Desert BDU
F2b	2 X 2	" "
F2c	1 X 1	" "
F3a	3 X 3	Cotton (green)
F3b	2 X 2	" "
F3c	1 X 1	" "
F4a	3 X 3	Nylon (green)
F4b	2 X 2	" "
F4c	1 X 1	" "
F5a	3 X 3	Cotton / Nylon (green)
F5b	2 X 2	" "
F5c	1 X 1	" "
F11a	3 X 3	Green Tenting
F11b	2 X 2	" "
F11c	1 X 1	" "
F12a	3 X 3	Nomex Kevlar Camouflage
F12b	2 X 2	" " "
F12c	1 X 1	" " "
F13a	3 X 3	Light Green Parachute
F13b	2 X 2	" " "
F13c	1 X 1	" " "
F14a	3 X 3	Dark Green Parachute
F14b	2 X 2	" " "
F14c	1 X 1	" " "

Table 4.3. Fabric Materials (From Anderson, 1995)

Target ID	Size (m)	Description
F6	2.75 X 2.75	Tan Vinyl
F7	2.75 X 2.75	Rust Plastic
F8	2.75 X 2.75	Tan Fiberglass
P2	2.4 X 2.4	Brown CARC Paint on Aluminum
P3	2.4 X 2.4	Tan CARC Paint on Aluminum
P5	2.4 X 2.4	Green CARC Paint on Aluminum

Table 4.4. Plastic and Painted Metals (From Anderson, 1995)

Target ID	Size (m)	Description
T1a	3 X 3	Spectral taggant on green fabric
T1b	2 X 2	“ “ “ “
T1c	1 X 1	“ “ “ “
T2a	3 X 3	T1 reference fabric w/o taggant
T2b	2 X 2	“ “ “ “
T2c	1 X 1	“ “ “ “ “
T3/V6	1 X 2	Spectral taggant applied to the bed of HMMWV (V6)

Table 4.5. Spectrally Tagged Targets (From Anderson, 1995)

Target ID	Size (m)	Description
VF1	4 X 8	T72 Tank, woodland
VF2	“	“ “
VF3	“	“ “
VF4	“	“ “
VF5	3 X 6	BTR 60, APC, woodland
VF6	“	BTR 70, “ “
VF7	“	BTR 80, “ “
V1	4 X 8	M1 U.S. Tank, woodland
V2	“	“ “ “
V3	“	“ “ “
V4	“	“ “ “
V5	3 X 6	HMMWV, woodland
V6	“	“ “
V7	“	“ “

Table 4.6. Mobile Vehicle Targets (From Anderson, 1995)

similar and different vehicle types, spectral discrimination between the same target type and between different vehicle classes can be evaluated. A spectral taggant was also

applied to three green fabric panels and one HMMWV, in order to determine its spectral enhancement properties.

Target ID	Description
DV1	M1, 2-D aerial, woodland
DV3	HMMWV, inflatable, woodland
DV4	HMMWV, inflatable, desert
C3	U.S. woodland camouflage, ULCANS radar scattering
C5	U.S. woodland camouflage, ULCANS radar scattering
C6	U.S. woodland summer camouflage, radar scattering open weave

Table 4.7. Decoys and Camouflage Targets (From Anderson, 1995)

b. Phase I - Exposed Material and Vehicle Experiments

The first phase of the experiment was conducted from 24-25 August. It emphasized the collection of hyperspectral signature data from unobstructed target panels, military vehicles and decoys, and camouflage netting. All of the target objects were deployed in the configuration shown in Figures 4.3 and 4.4. The fully exposed

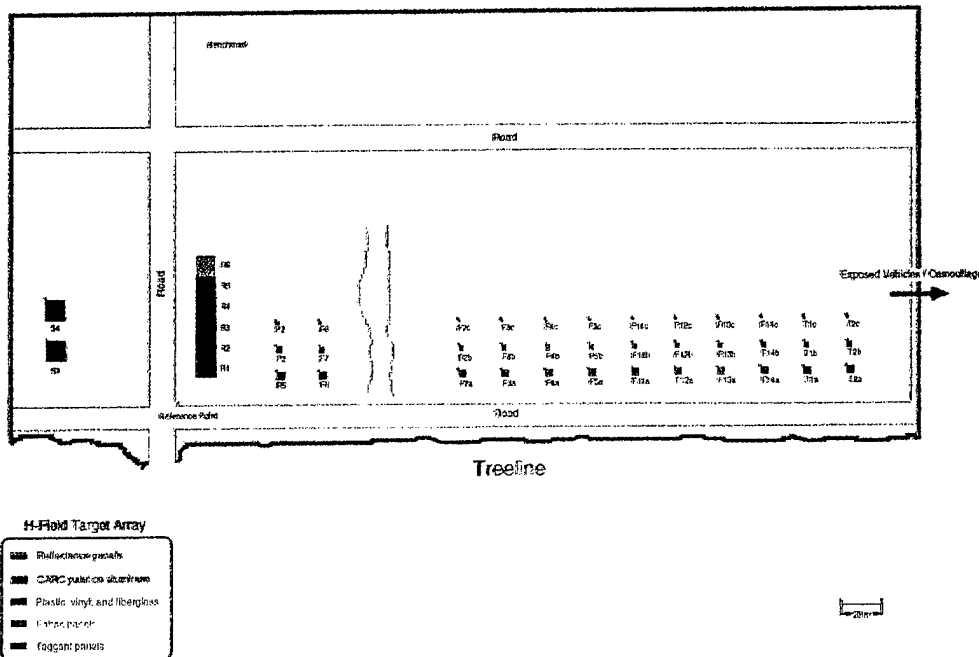


Figure 4.3. Forest Radiance I Exposed Target Array (From Anderson, 1995)

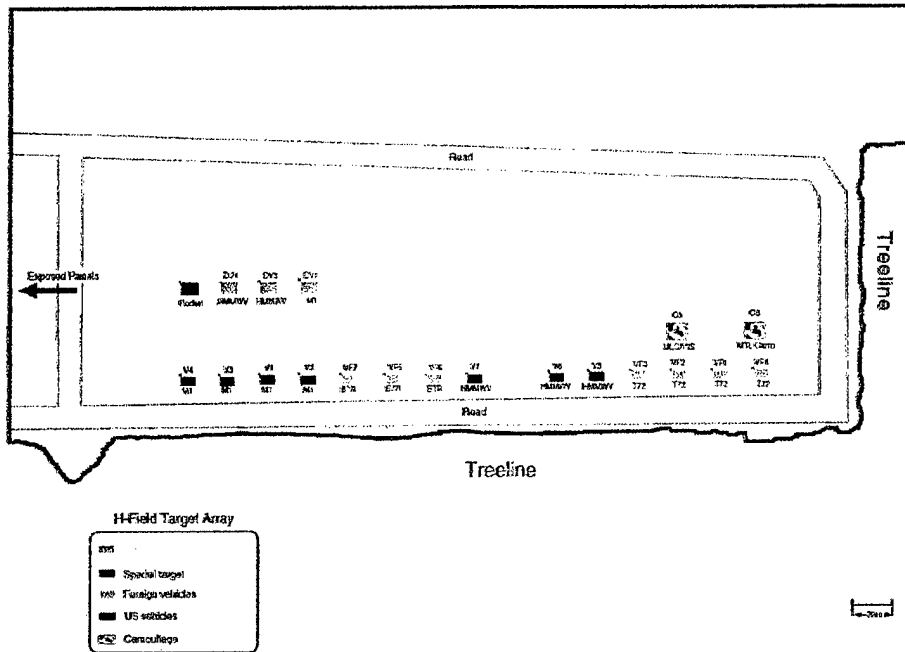


Figure 4.4. Forest Radiance I Exposed Target Array (From Anderson, 1995)

test area provided a uniform energy distribution on the target array, thus yielding quantitative surface condition results. This test area also provided a near-uniform grass background which enhanced the spectral contrast between the military relevant targets and the natural vegetative background. Two inflatable HMMWV decoys were also deployed in a fashion similar to that of the HMMWV. The primary thrust of the work presented here centers on discerning any spectral separability between the real HMMWVs and their decoys.

c. Phase II - Shadow and Adjacency Experiments

Phase II of the experiment was conducted on 26 August. It primarily addressed the complexity of collecting and analyzing hyperspectral signature data in a shadow environment. This phenomenon was explored by repositioning several targets to the shadowed region adjacent to the treeline, resulting in a decrease in illumination effects. These non-linear effects are attributed to changes in light quality (lack of direct sun or reflected sky light), which make target detection and spectral characterization

exceedingly more difficult. An array of three target panels were also positioned perpendicular to the shadowed objects in order to compare the panel reflectance in the exposed experiment to those influenced by adjacency effects. This low-illumination experiment represented the first of two phases in which the target concealment states increased using natural cover. The semi-exposed targets in Phase II likely received some reflected energy from the adjacent foliage, while Phase III of the experiment provided an even more challenging environment.

d. Phase III - Concealed Vehicle Experiments

Phase III was conducted on 29 August. This phase emphasized the detection and spectral characterization of targets in a dense forest environment. Figure 4.5 illustrates how the Sun's radiant energy first passes through breaks in the canopy before reflecting off the target objects and ascends towards the overhead sensor through a different opening.

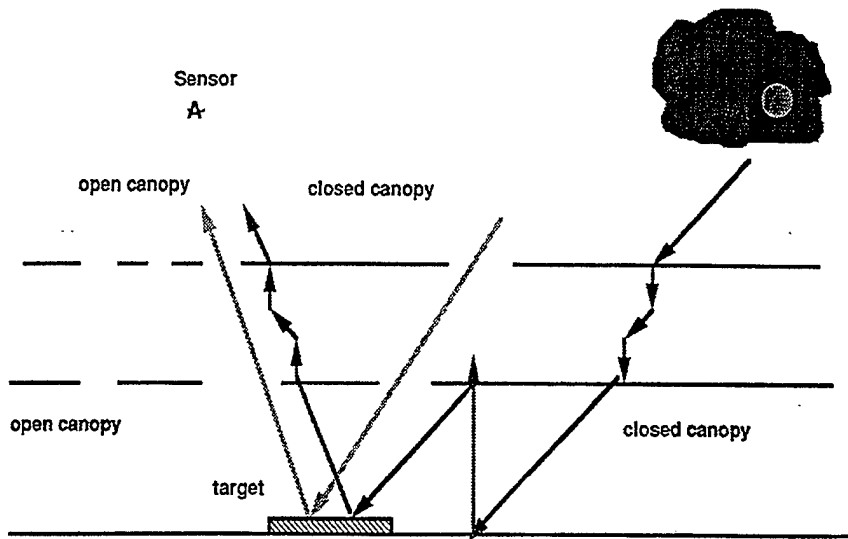


Figure 4.5. Canopy Geometry for Concealed Targets (From Anderson, 1995)

To simulate more realistic conditions, several of the target objects were repositioned to the heavy foliated area to study the non-linear effects due to canopy. This condition

provided only limited direct sun or reflected sky light, thereby reducing target illumination by a significant amount. A series of target configurations were employed to only partially conceal the target, and complete target obscuration was avoided. The target array was specifically designed and positioned to develop linear unmixing algorithms used to quantify the fraction of concealment. No actual or decoy HMMWVs were deployed in this phase of the experiment.

5. Ground-Truth Measurements

Each experiment included a dedicated “ground-truth” collection program. The U.S. Army Topographic Engineering Center (TEC), Ft. Belvore, VA, provided all ground-truth measurements in support of the Forest Radiance I experiment. This survey was conducted to minimize the complexities associated with natural surfaces, and to mitigate the atmospheric effects and spectral signature ambiguities that tend to limit hyperspectral imaging. The ground-truth measurements provided a means in which the true surface reflectance of a material can be related to the reflected radiance values observed at the sensor. This activity is necessary so that an apparent reflectance data set can be derived. This apparent surface reflectance is calculated by measuring atmospheric conditions, like spectral transmittance and scattering, and removing them from the image scene.

The total radiance (L_T) reaching the focal plane of the sensor is comprised of reflected surface radiance (L_{SR}), thermal surface radiance (L_{SE}), scattered atmospheric radiance (L_{SC}), and background reflected radiance (L_{BS}). These values are described algebraically in equations 4.1 and 4.2:

$$L_T = L_{SR} + L_{SE} + L_{SC} + L_{BS} \quad (4.1)$$

$$L_{SR} = (E \cos \Phi) * L_D * R * L_U \quad (4.2)$$

where E is solar irradiance, Φ is solar zenith angle, L_D is downward transmittance, R is surface reflectance, L_U is upwards transmittance, and $L_{SE} = 0$.

TEC ground-truth teams collected over 400 *in situ* spectral signatures using a GER Field Spectrometer. The measurements of the target panels and vehicles were collected from an average height of 1 m, while the larger camouflage materials were sampled using a truck mounted mechanical boom. The reflectance data was collected in the 0.35 - 2.5 μm range and their values calculated relative to the Spectalon 99% reflectance standard. Simple target objects were measured at least three times, while more complex materials like camouflage netting were measured several times. The signature data was recorded by a portable personal computer used to operate the spectrometer. The data was later down-loaded to a DOS formatted 3.5" diskette for dissemination to the exploitation teams (Anderson, 1995).

6. Sensor Characteristics

The Forest Radiance I experiment employed both remote sensing spectroscopic and imaging functions into a single integrated sensor. Therefore, considerable effort was made to select an advanced imaging spectrometer that addressed several long-standing limitations inherent to imaging spectroscopy (i.e., sensitivity and calibration accuracy, signal-to-noise ratio, spatial and spectral resolutions, number of spectral bands, and ability to process large amounts of data). The Hyperspectral Digital Imagery Collection Experiment (HYDICE) and Airborne Remote Earth Sensor (ARES), two high quality state-of-the-art spectroradiometers, were selected to correct for these deficiencies and to make the wide range of spectral measurements designed into the experiment.

a. *Hyperspectral Digital Imagery Collection Experiment (HYDICE)*

The HYDICE sensor was designed and developed by Hughes-Danbury Optical Systems, Inc., to provide high quality hyperspectral data to explore literal and nonliteral exploitation techniques for a wide variety of military and civil applications.

Figure 4.6 shows the HYDICE instrument. The sensor is fully integrated onboard a Environmental Research Institute of Michigan (ERIM) Convair (CV-580) aircraft and operates in accordance with HYPO tasking. The sensor is a nadir-viewing, 210 channel imaging spectrometer covering a spectral range from 0.4 μm to 2.5 μm ; visible through

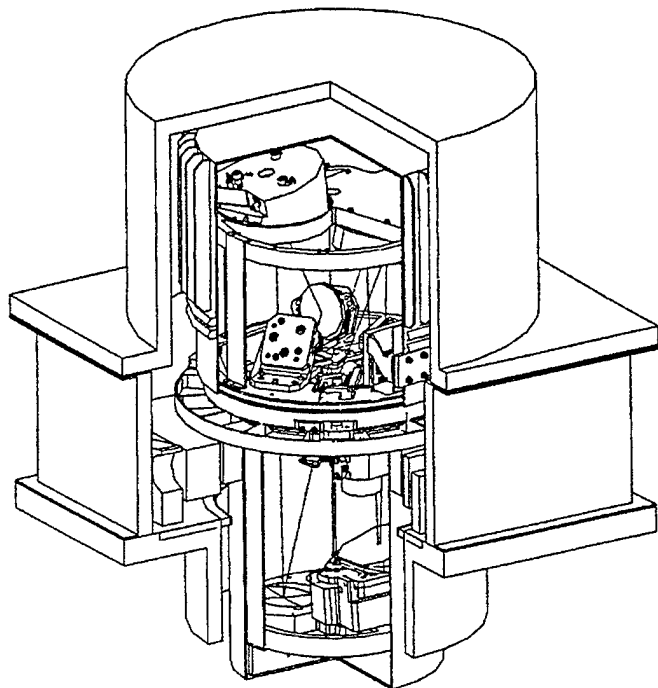


Figure 4.6. HYDICE Instrument (From Anderson, 1995)

the SWIR domain. The spectrum is sampled contiguously in 10 nm wide channels using a pushbroom technique. Light enters the sensor perpendicular to the flight path, and is then dispersed by a prism onto a single array detector. The sensor covers a swath width of approximately 1 km and provides a GSD ranging from 0.75 to 3 m, depending on its operating altitude. Table 4.8 summarizes the HYDICE sensor's characteristics.

Table 4.8. HYDICE Sensor Characteristics (From Anderson, 1995)

b. Airborne Remote Earth Sensor (ARES)

The Airborne Remote Earth Sensor (ARES) system is a high altitude imaging spectrometer mounted onboard a WB-57-F aircraft. The aircraft nominally operates at an altitude of approximately 60,000 ft, at speeds ranging from 120 to 400 kts.

The sensor is a nadir-viewing, 75 band spectrometer with a MWIR spectral range of 2.0 μm to 6.3 μm . The sensor operates using a mechanical sweeping, or scanning motion, and provides a nominal GSD of 20 m, depending on the altitude of the aircraft (Anderson, 1995). The spectral range of this instrument's data set is beyond the scope of this thesis. ARES characteristics are summarized in Table 4.9.

System Attribute	Specification
Platform	NASA WB-57F
Aircraft operating altitude	Sea level - 18,900 m (62,000 ft)
Optics	Dual Mode MWIR 2-D Scanning Imaging Spectrometer -- Afocal Reflective Slit Spectrometer Telescope -- 2-Element Ge-MgO Prism Assembly
Aperture diameter	50 mm
Focal length	95 mm
Swath FOV	3.0 X 3.0 degree scan & sweep
Swath width	45 pixels
IFOV	1.17 mrad (Spatial), 360 mrad (Slit)
Array size	45 X 90 pixels
Integration time	1-80 Hz selectable
Quantization	12-bit A/D Conversion
Detector Pitch	100 μm
Spectral Coverage	2.0 - 6.3 μm
Spectral Range	2.0 - 7.0 μm
Spectral Resolution	25 - 70 nm
Instrument operating temperature	Internal Optics 77°K, Detector 24°K
Si:IN focal plane array	BP Filters: none, 2.21-2.26, 2.71-2.97, 3.72-3.84, 4.41-4.56 μm ND Filters: none, 0.34, 0.0, 0.01, 0.001
Noise	<0.001 X Mean FPA Illum Level
Sensitivity	1.0 μW per $\text{cm}^2/\text{steradian}/\text{micron}$
Video Track Sources	Wide & Narrow Field TV Cameras PtSi short-wave-infrared Camera
Pointing Range	$\mp 90^\circ$ in roll, 30° fwd, 20° aft in pitch
Scanning Mirror	Sweep Slit Projection Across Target Range $\mp 1.5^\circ$, rate 0-6.0°/sec

Table 4.9. ARES Sensor Characteristics (From Anderson, 1995)

7. Ground Data Processing Subsystem (GDPS)

The Ground Data Processing Subsystem (GDPS) is physically located at the HYPO. The hardware configuration used to process large volumes of raw hyperspectral data consists of a Sun SPARC 2 630MP deskside server, 2 Gbytes of internal disk space, 2 8mm external disk drives, 1 AMPEX tape recorder, and a high quality laser printer. The AMPEX tape recorder is identical to the aircraft's "record only" device, but includes an additional playback feature to access the recorded data. The data is recorded onto the AMPEX tape during flight and stored in a binary format. The image data is collected and saved in minor frames (320 cross-track pixels by 210 bands) for the duration of the overflight. These minor frames are grouped into major frames (320 minor frames) and are preceded by a header block for quick identification. The function of the GDPS is to review data tapes from the aircraft, extract select portions of the data sets, convert the brightness values (DN) recorded by the sensor to radiance values, and then distribute the image data via 8mm tape to the exploitation teams for analysis. Analytical functions are carried out on an identical hardware configuration (less tape recorder). Final output images and spectral plots are transferred to a personal computer for annotation and document insertion (Kappus et al., 1996).

V. OBSERVATIONS AND ANALYSES

A. TECHNICAL OBJECTIVE

The H-Field range was divided into separate target areas to maximize probability of success for each individual mini-experiment. To satisfy the broad range of objectives, a wide array of target objects of varying shapes, sizes, and material types were deployed in different orientations throughout the test area. The primary objective of this report is to ascertain the utility of hyperspectral data and exploitation techniques to detect and discriminate the spectral signatures of exposed mobile vehicles (HMMWVs) and decoys, against the natural grass background. A thorough examination of the spectral variability inherent in these objects and on-line target and anomaly detection methods (i.e., PCA, LPD, and SAM) was conducted. This report defines an anomaly as a target of military interest.

B. DATA PROCESSING

In-flight processing and calibration to apparent reflectance has not met with a significant amount of success and is assessed as impractical in application. Post-flight data preparation, however, can be accomplished through a series of iterative steps with minimal effort. Here is how the Forest Radiance I data sets were obtained.

1. Post-Flight Processing

The first step is to create a “table of contents” which delineates the tape’s contents relative to the data’s location on the tape. The second step involves the extraction of a “quick look image” from the tape to assess the quality of the data collected during each of the runs. This evaluation is accomplished by a cursory review of the coverage area, image content, instrument artifacts, and distortions attributed to aircraft movement (pitch, yaw, etc.). This step also provides information necessary to determine the major frames of an image scene, which allows for quick access of only those data segments of interest.

The final step involves converting the data from instrument DN to a calibrated radiance levels. More detailed information concerning the radiometric calibration technique can be found in Aldrich et al., [1995].

2. Reflectance Conversion

Converting remotely sensed spectrometer data to apparent reflectance is widely considered the most important first step in the analysis of hyperspectral imagery. This transformation process seeks to approach the absolute reflectance of the scene's target materials without having to take spectral measurements in the field. Researchers have developed several post-flight calibration techniques that come close to the goal of recovering the true surface reflectance. The Empirical Line Method was used here to convert the radiance data sets to apparent surface reflectance.

a. Empirical Line Method (ELM)

The correction of the HYDICE data to apparent reflectance was accomplished using the Empirical Line Method (ELM). The ELM converts the radiance data to an apparent surface reflectance based on the internal characteristics of the data set. This method requires an *a priori* knowledge of the target area, and each scene must include a minimum of two regions (i.e., calibration panels) with a broad range of reflectance values. Ground-truth-derived spectra of the calibration panels are necessary and must also be acquired in the field. The next step is to manually select pixels from the scene that correspond to each target region to record their apparent reflectance values. A linear regression is then calculated to determine the gains and offsets for each band in the image cube using equation 5.1:

$$\text{DN} = \rho A + B \quad (5.1)$$

where DN is the digital number of a specific pixel; ρ is the reflectance of a the region of interest; A is the multiplicative term which represents a solar irradiance curve (gain); and B is the additive term which represents atmospheric path radiance (offset). Solving this system of linear equations for variables A and B also provides an estimate of the standard errors at each wavelength. The final step is to multiply the sensor-derived DN values by the calculated gain and then add its corresponding offset value to remove unwanted scattering, absorption, and attenuation effects caused by the atmosphere. This technique, while not perfect, does facilitate comparisons between remotely sensed spectra and field- or laboratory-derived spectral signatures (Farrand, 1992).

C. ANALYSES

This report describes a multi-step strategy that allows for the unexpected. To take full advantage of the data sets, both radiance and apparent reflectance images were examined; however, the results from the analyses showed no discernible difference between using radiance or apparent reflectance input data. Therefore, this report will refer to only apparent reflectance image scenes.

1. Forest Radiance I Data Set

A HYDICE-derived hyperspectral image scene, transformed to an apparent surface reflectance, analyzed in this thesis was selected from: Run 05, major frames 51-54, acquired on 950824 at an altitude of 5,000 ft above ground level (AGL) at 0910 local time (L). Reference endmembers or target spectra were either sampled directly from the image cubes being analyzed or selected from *in situ*-derived ground-truth measurements. In all, thirty nine (39) target signatures were selected for processing. Twenty (20) endmembers were scene-derived and selected based on the spatial context of three (3) actual HMMWVs (V5, V6, and V7) and two (2) decoy HMMWVs (DV3 and DV4); that is, four (4) spectra were extracted from each of these five (5) target vehicles. Five (5) mean spectra were derived by averaging the four (4) pixels from each of these same vehicles. This averaging technique was employed because exposed target pixels are

rarely homogeneous and averaging compensates for some of the spectral variability. The remaining fourteen (14) spectra were derived based on the available *in situ* ground-truth measurements of V5, DV3, and DV4. A qualitative analysis of these spectral signatures is conducted in Section D of this chapter.

Figure 5.1 is shown here to orient the reader and establish target position of the overtly exposed vehicles arrayed during the first phase of the experiment. All vehicles relevant to this investigation are prominently displayed and labeled to the right of the target array.



Figure 5.1. Overtly Exposed Target Vehicles of Interest

2. Methodology/Approach

A Principal Components Analysis (PCA) was first applied to the image cube to estimate the inherent dimensionality of the data sets being analyzed. This intrinsic dimensionality does not correspond to the exact number of bands in the data set since scenes typically have significant correlation between image bands. The intent is to compress the information content of the data set into a relatively few principal component (PC) bands. Low Probability of Detection (LPD) and Spectral Angle Mapper (SAM) target and anomaly detection techniques were then applied to physically highlight pixels found to have similar spectral characteristics as the target spectra. The LPD and SAM algorithms required the selection of an endmember spectra as a target signature, with the remaining image spectra being undesired. The search methods yield a resultant match relative to this target signature and is based on a non-arbitrary threshold of that measure.

D. FINDINGS

The LPD and SAM processing techniques serve to reduce the spectral dimensionality of the data set being analyzed. The number of bands in the output cube is equal to the number of target materials considered. All of the target spectra were acquired directly from the image scene. The results to be presented demonstrate the robustness of these techniques in detecting and discriminating HMMWV and decoy target vehicles.

1. Qualitative Analysis of Signatures

Figure 5.2 is a representative sample of the natural grass background featured in the scene. All four spectra were taken from an area that appeared to have a uniform distribution of healthy green vegetation. Note the substantial similarities in the four spectra. The spectral response in the visible portion of the spectrum is primarily in the green band between 0.5 μm and 0.6 μm . The reflectance for healthy green vegetation is usually around 10 to 15 percent. Here the grass has a reflectance values of about 8 percent. Reflectance increases rapidly in the NIR, reaching a maximum of around 30 to

40 percent. This is referred to as the chlorophyll IR band, and its steep slope is indicative of vegetal materials. The dips at $1.4\text{ }\mu\text{m}$ and $1.9\text{ }\mu\text{m}$ are due to atmospheric water absorption, which is not fully compensated for in the calibration process. Note that there is negligible signal in the data at these wavelengths.

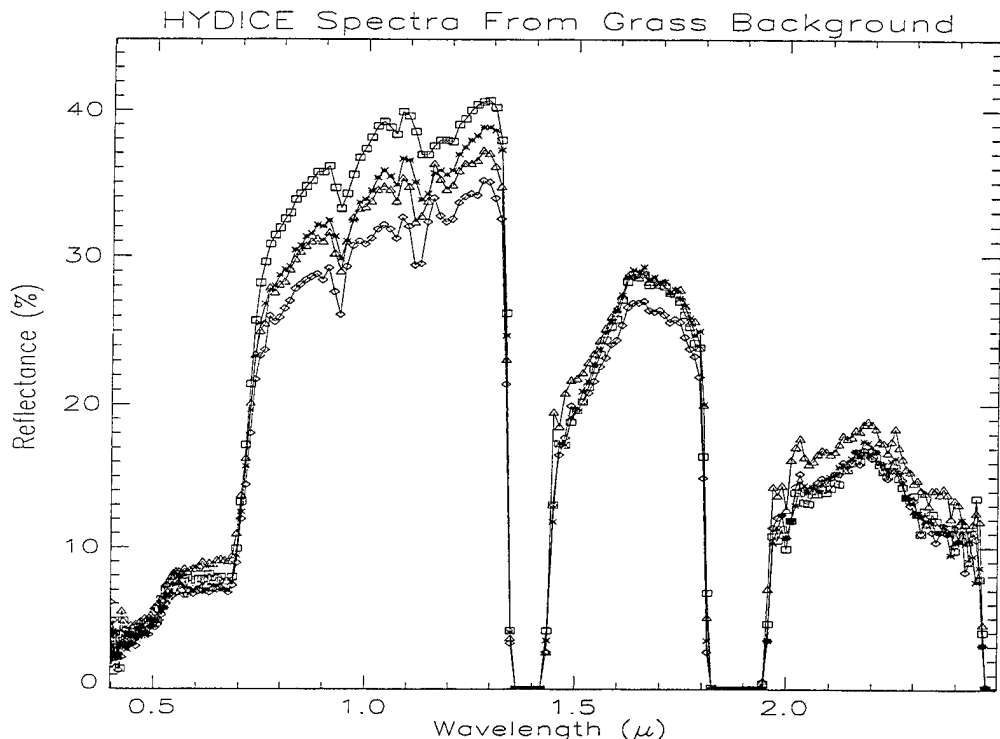


Figure 5.2. Scene-Derived Spectra From Natural Grass Background

Figure 5.3 shows the scene-derived spectra taken from V5. Observe that each spectra exhibits a chlorophyll response similar to the natural grass background. There are two plausible explanations for this very curious phenomenon. One possibility is that the materials used in the camouflage paint was manufactured to mimic natural vegetation in that portion of the spectrum. It is also feasible that the sensor recorded the photons that had first reflected off the adjacent tree-line or the surrounding grass before interacting with the vehicle. Further notice the significant amount of variation in the four spectra. Table 5.1 is provided to characterize V5's intra-spectra relationship, using as a measure

correlation coefficients. Note that the self-correlation values for the spectra range from 0.86 to 0.96. These statistical variances could be attributed to either the complex signature associated with the camouflage paint schemes, but may also be the result of specular scatter. An interview with one ground-truth team member indicated that the paint in the bed of at least one vehicle was extremely worn and the underlying metallic material was clearly exposed. Glint may have also resulted from solar energy reflecting off the windows of the real vehicle.

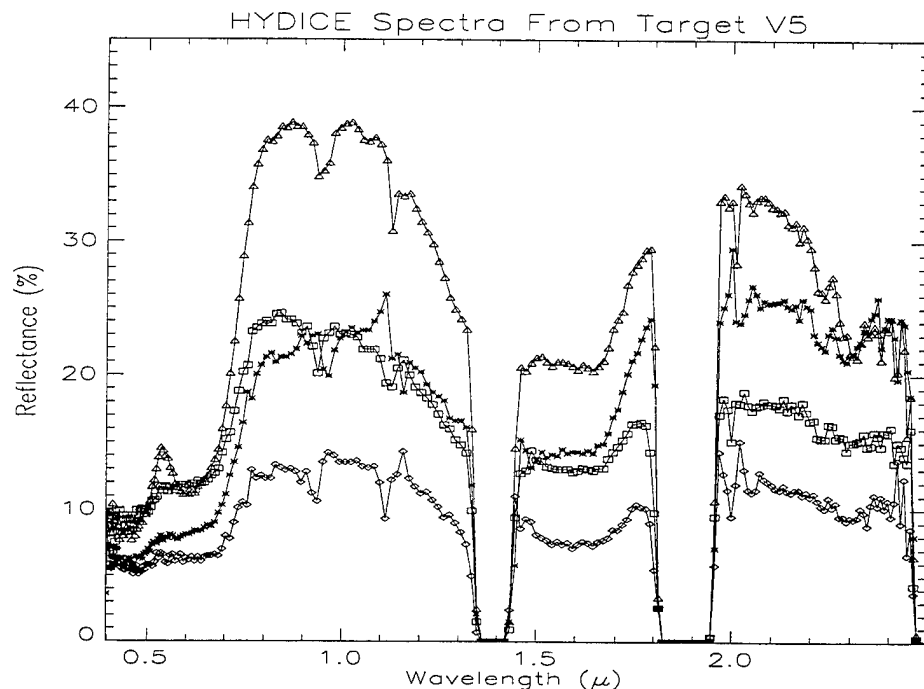


Figure 5.3. Scene-Derived Spectra From V5 (HMMWV)

Correlation in V5 Spectra

	Spectra 1	Spectra 2	Spectra 3	Spectra 4
Spectra 1	1.00	0.89	0.93	0.86
Spectra 2		1.00	0.94	0.95
Spectra 3			1.00	0.96
Spectra 4				1.00

Table 5.1. Correlation Coefficients Associated With Spectra From V5

Figure 5.4 is the ground-truth-derived spectra from V5. Ground-truth spectra are also available for DV3 and DV4 (plots not provided). All ground-truth measurements were collected using a nadir viewing angle and were sampled five times at varying heights above the target objects: V5 at 3 and 10 m; DV3 at 100 centimeters (cm); and DV4 at 8 and 10 m. Multiple samples were taken to obtain a representative spectral signature of the complex paint schemes and materials used to construct the target vehicle and decoys. Note the same wide variability is found in the ground measurements shown here, as in the HYDICE measurements. Although there is not a detailed correspondence between the spectra shown in Figures 5.3 and 5.4, there are reasonably obvious spectral similarities. The correlation coefficients associated with these spectra vary from 0.83 to 0.96. The ground-truth-derived spectra were not used in the analyses.

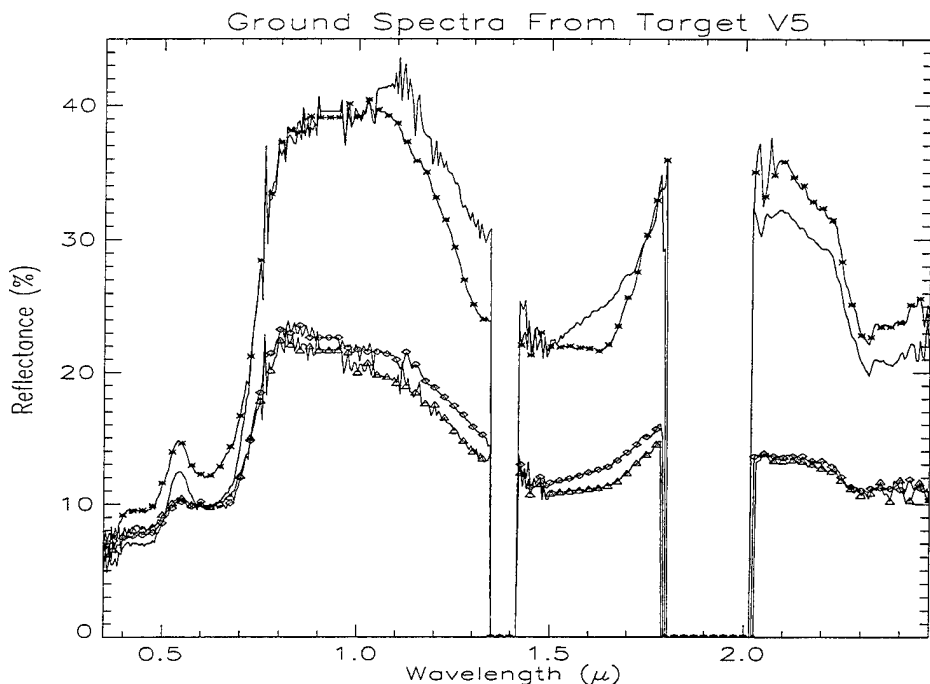


Figure 5.4. Ground-Truth-Derived Spectra From V5 (HMMWV)

Figures 5.5 to 5.8 show the scene-derived spectral line-plots for V6, V7, DV3, and DV4. The HMMWVs (V6 and V7) also display the same chlorophyll edge found in the

natural grass background and target object V5. This feature, however, does not appear in the spectra taken from either DV3 or DV4. In the green band, DV4's spectral response is also substantially greater than the reflectance values found in the other target objects. Spectral reflectance increases rapidly between $0.5 \mu\text{m}$ and $0.6 \mu\text{m}$, reaching a maximum of around 30 to 40 percent. These features tend to support the premise that the fabric material used to assemble the decoy alters the characteristics of the energy reflected from its surface. Variations in DV4's intensity are recorded in Table 5.2. Note that these variations are statistically less significant than those observed in V5 (see Table 5.1).

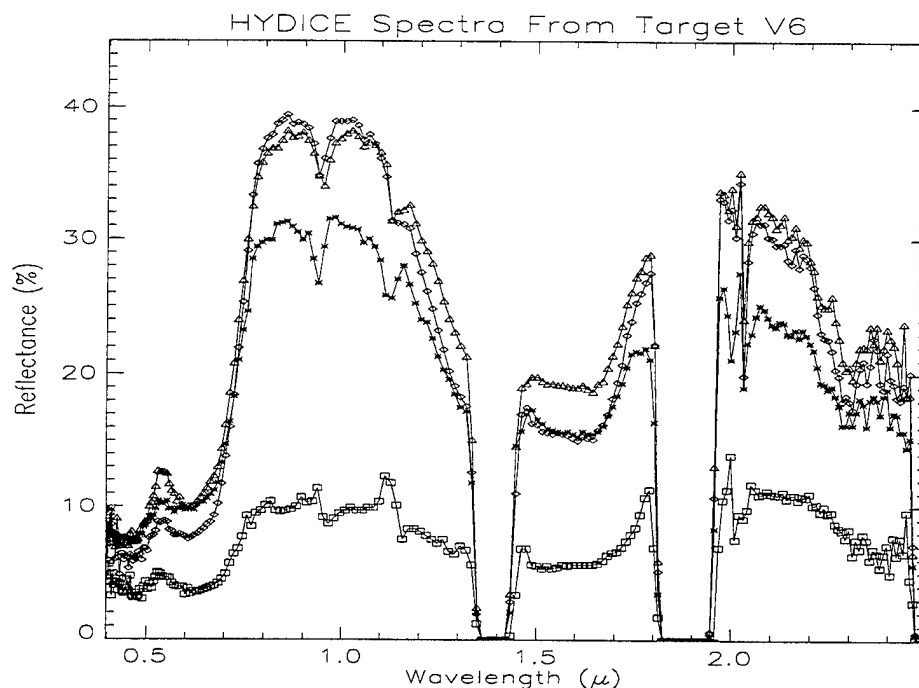


Figure 5.5. Scene-Derived Spectra From V6 (HMMWV)

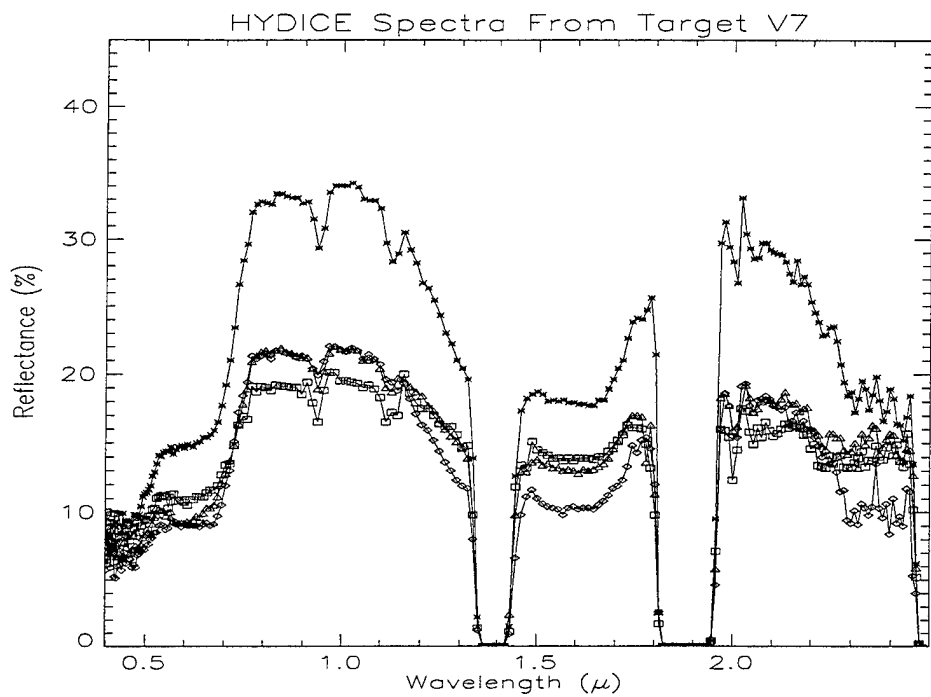


Figure 5.6. Scene-Derived Spectra From V7 (HMMWV)

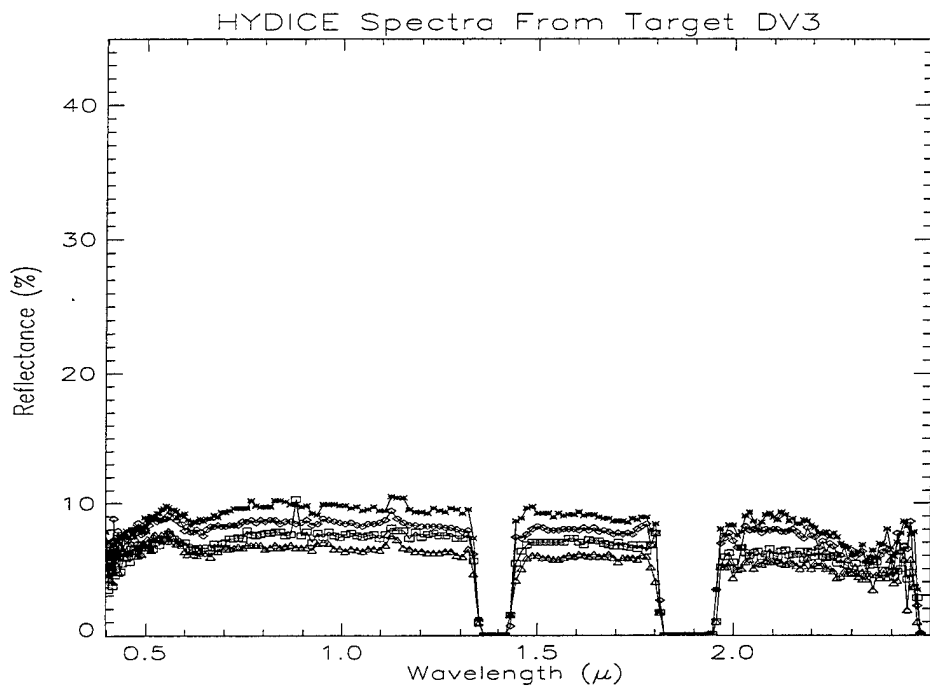


Figure 5.7. Scene-Derived Spectra From DV3 (Decoy)

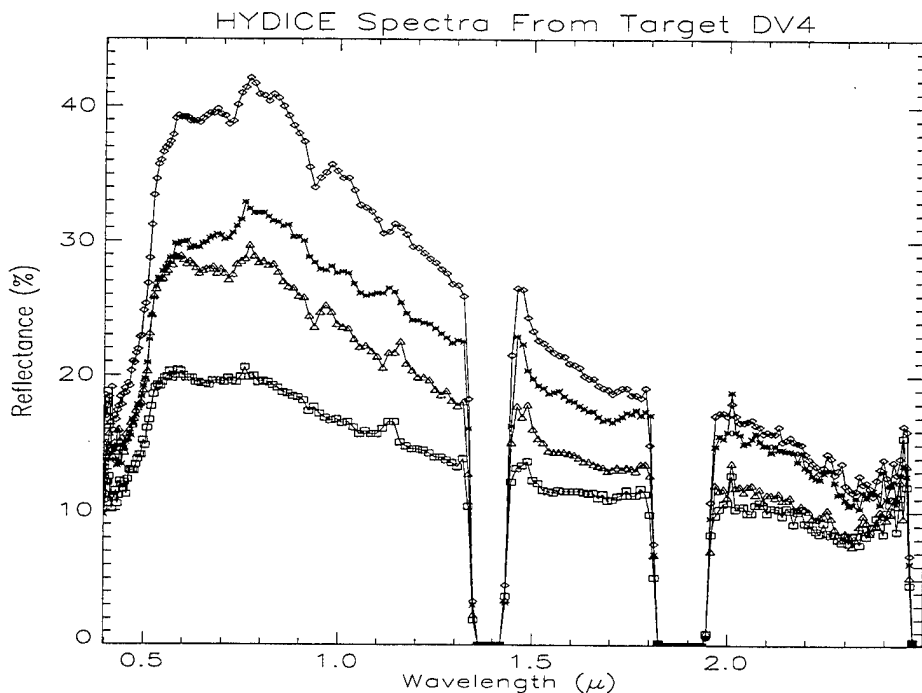


Figure 5.8. Scene-Derived Spectra From DV4 (Decoy)

Correlation in DV4 Spectra

	Spectra 1	Spectra 2	Spectra 3	Spectra 4
Spectra 1	1.00	0.99	0.98	0.97
Spectra 2		1.00	0.99	0.97
Spectra 3			1.00	0.98
Spectra 4				1.00

Table 5.2. Correlation Coefficients Associated With Spectra From DV4

The spectral response fluctuates to some degree within each of the target objects. To compensate for these variations in spectrum an averaging technique was applied to calculate a mean spectra for each vehicle. This approach was considered necessary in order to decrease the probability of false alarms later on in the analyses. Figure 5.9 combines these mean spectra into a single figure to illustrate the spectral diversity within each natural and man-made target class. V7's means spectral signature is almost identical to V5 and has been omitted from the plot to avoid cluttering the figure. The individual

spectra are labeled and displayed with an offset value to assist the reader in discerning the inherent characteristic associated with each spectra under examination. The different scene elements differ substantially still, ranging form the flat spectrum of DV3 to grass with its sharp chlorophyll edge. Table 5.3 lists the correlation coefficients associated with these spectra. Note that the correlation between targets (average spectrum) is higher than most of the values shown in Table 5.1 for target V5.

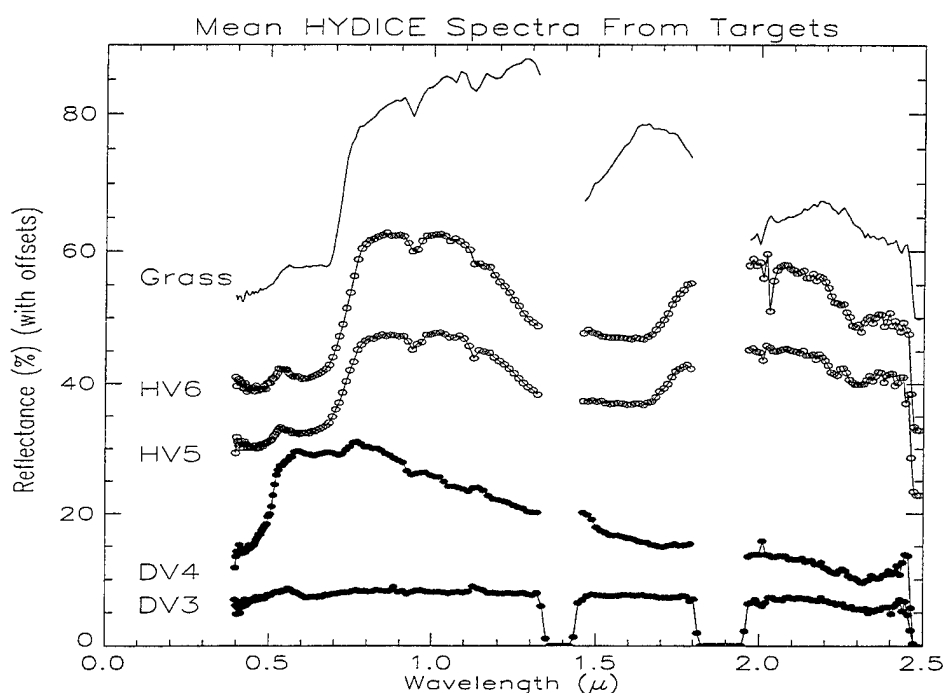


Figure 5.9. Mean Spectra From Targets of Interest

Correlation in Mean Spectra

	DV3	DV4	Grass	V5	V6
DV3	1.00	0.92	0.92	0.96	0.96
DV4		1.00	0.96	0.97	0.96
Grass			1.00	0.99	0.98
V5				1.00	0.99
V6					1.00

Table 5.3. Correlation Coefficients Associated With All Spectra

The spectral characteristics of military paints, regardless of the underlying material, can closely match features exhibited by some natural backgrounds. In this instance, however, significant differences were present between the man-made materials and the natural grass background. The grass has a very distinct signature compared to man-made objects in the NIR and SWIR regions. The man-made materials either level off or decrease significantly within the same regions. A direct comparison at $1.32\text{ }\mu\text{m}$ reveals that the grass has a reflectance of nearly 39 percent (correcting for the offset), whereas V5, V6, and V7 measure at a much lower value of 20. All of the man-made objects, with the exception of DV3, share a broad absorption feature between $1.5\text{ }\mu\text{m}$ and $1.7\text{ }\mu\text{m}$. The grass spectra shows no sign of absorption in this region. DV3's spectral signature is generally featureless across the entire continuum. Data associated with DV3 is assessed as suspect due to difficulties encountered during set up. Field technicians were unable to keep the decoy inflated during the collection process, and thus, it was sampled under less than ideal conditions. The most striking similarities occur in spectra taken from the same target class (i.e., HMMWVs). Their like spectral shape and similar reflectance values are most obvious in the regions from $0.7\text{ }\mu\text{m}$ to $1.23\text{ }\mu\text{m}$ and $1.5\text{ }\mu\text{m}$ to $1.7\text{ }\mu\text{m}$. The shorter wavelengths are characterized by high reflectance values, where the latter region is dominated by a broad absorption feature. The reader is invited to make additional comparisons between all the scene-derived and *in situ*-measured spectra signatures.

Not every target is obviously spectrally unique. Figure 5.10 compares spectra from two different target classes (HMMWV and M-1 Tank) to illustrate the similarities that appear between two dissimilar vehicle types. Both HMMWV and M-1 Tank are easily discernible in the visible region of the spectrum, but their signatures become less distinct longwards of $0.7\text{ }\mu\text{m}$. Calculating the correlation coefficients we get a value of 0.91, indicating that the apparent similarities in the spectrum is something of an illusion. The Tank's high intensity in the visible is probably due to the brighter hues used in

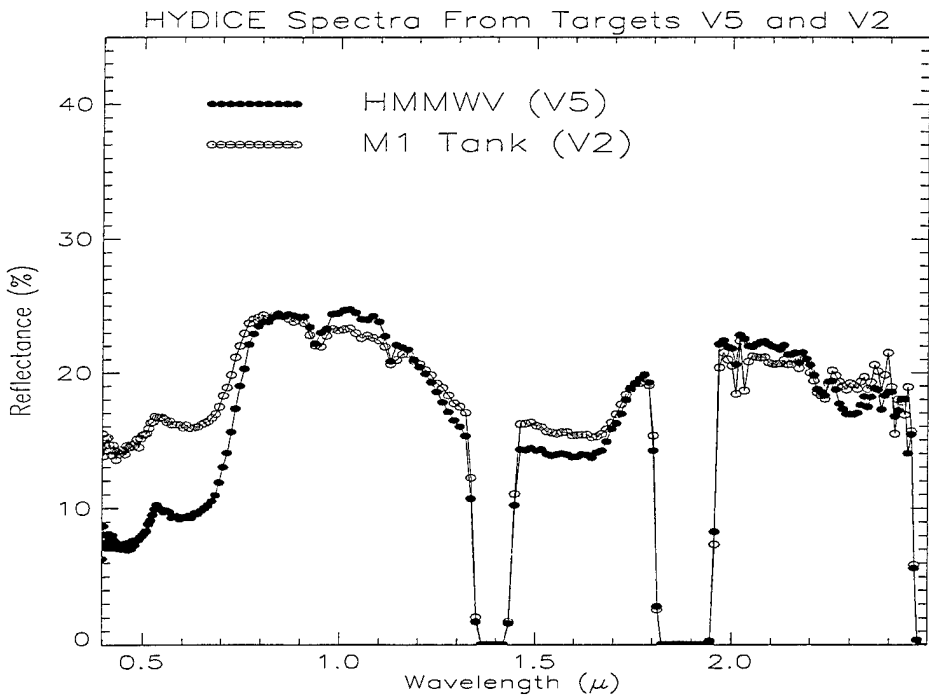
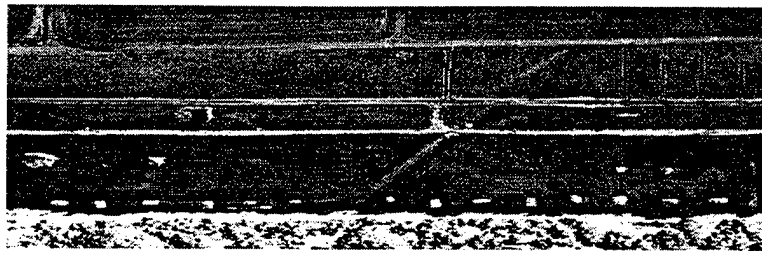


Figure 5.10. Mean Spectra From Targets V5 and V2

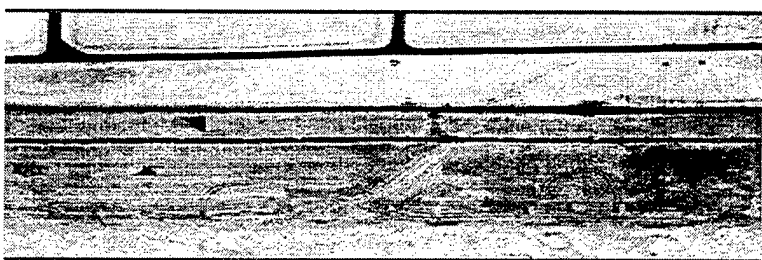
woodland camouflage paint scheme. Note that these dissimilar vehicles have a reasonably high correlation coefficient and, in some instances, are more closely correlated than spectra taken from a single vehicle (i.e., V5). This similarity made the separation of individual spectra extremely difficult and, understandably, account for many of the false alarms the author encountered during the analyses.

2. Principal Components Analysis (PCA) Results

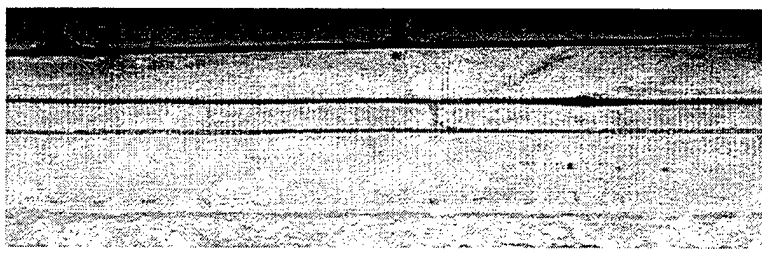
The data set was first investigated using the Principal Components Analysis method. Figures 5.11 and 5.12 show the first ten PC image bands that result from the application of the algorithm. The figures were compressed in the vertical to maximize space and facilitate comparisons between bands. The scene which included the exposed vehicles was selected for the transform. The first step was to qualitatively analyze the PC bands from highest to lowest total variance, to observe any degenerating trends in the data set. The results are consistent with our understanding of the how the PCA technique



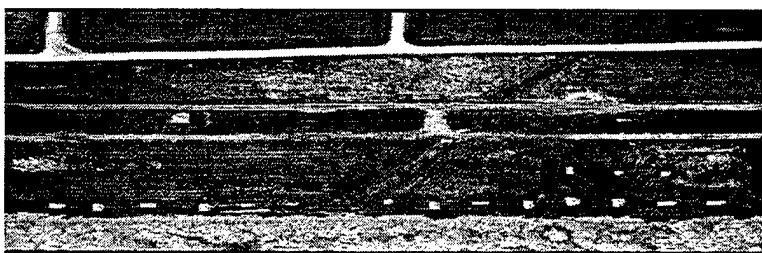
1



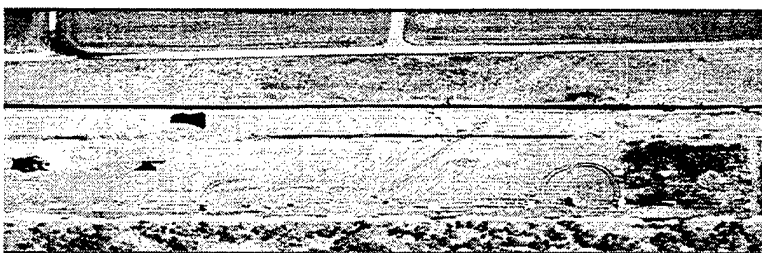
2



3

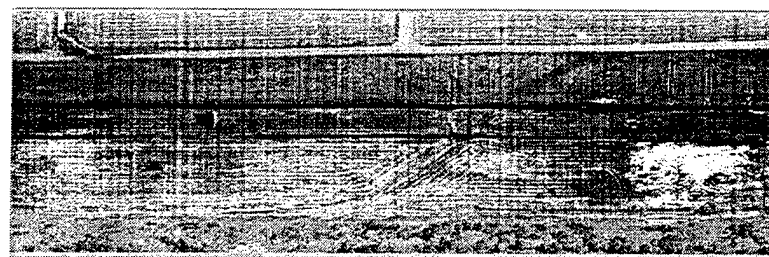


4

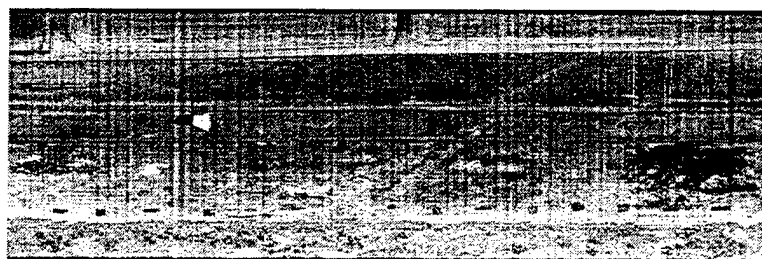


5

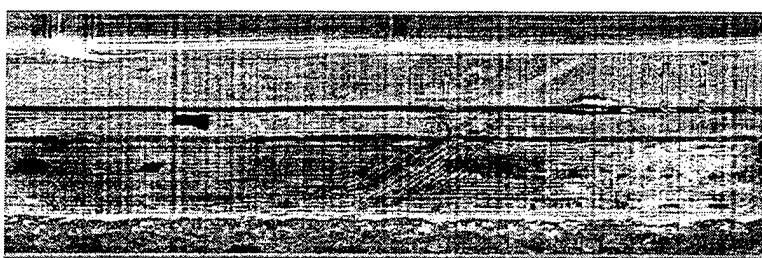
Figure 5. 11. Principal Components Bands 1, 2, 3, 4, and 5 (Ordered Top to Bottom)



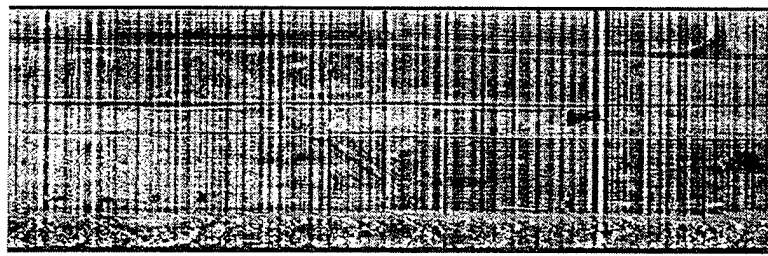
6



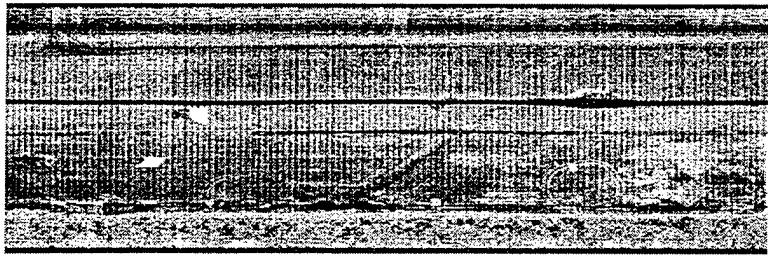
7



8



9



10

Figure 5.12. Principal Components Bands 6, 7, 8, 9, and 10 (Ordered Top to Bottom)

models the basic structure of the data set. The first PC band is typically associated with the total brightness in the image, whereas the next four or five bands highlight differences. Clearly this has analytical benefits since bands one, four, and five highlight the man-made objects in the target array. The remaining, less-correlated bands are dominated by noise and sensor artifacts and do not provide any information of significance to this study.

The second step involved interpreting a graphical plot that shows the most significant components (i.e., eigenvectors) that describe scene's variance. Figure 5.13 provides this graphical illustration. A linear plot is provided to improve the visual interpretation of the PCA results, but the same general situation occurs here too.

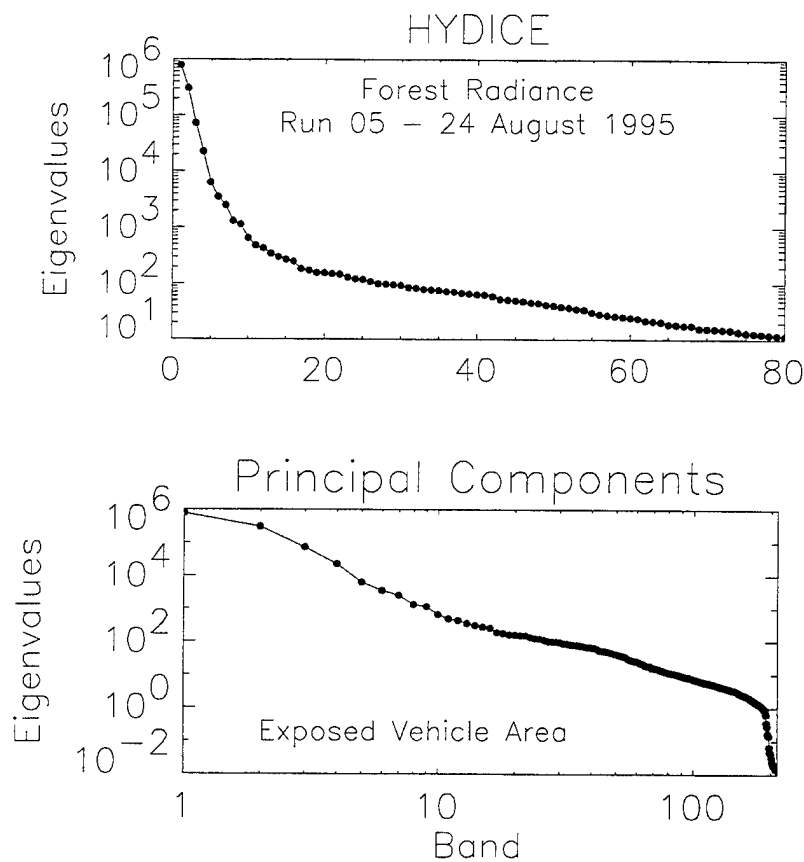


Figure 5.13. Linear and Logarithmic Plots of Total Variance vs. PC Bands

A straightforward examination of the line-plot confirms that the majority of the total variance in the scene is relegated to the first few components. The negative slope of the curve begins to decrease as bands become less correlated. The most significant change in slope is localized between bands ten and fifteen. A logarithmic plot of the PCA components is also provided as an alternate way of interpreting the results. The latter plot shows that there is one additional drop in variance at band 200.

Calculating the inherent dimensionality was found to be a computationally expensive process and the results somewhat difficult to quantify. After careful examination, the author determined that the intrinsic dimensionality of the scene could be represented by as few as fifteen eigenvectors.

3. Low Probability of Detection (LPD) Results

The performance of the Low Probability of Detection (LPD) method depends on the inherent dimensionality of the data set being analyzed. Prior to the running the LPD algorithm, the scene's eigenvectors were calculated and a correlation matrix built. These primary eigenvectors were used by the algorithm to suppress the unwanted spectral signatures that dominate the image, leaving the remaining spectral signatures (i.e., those not included in the selected eigenvectors) to appear as false alarms in the output. The LPD algorithm was applied here in an attempt to discriminate real targets and decoys, and those of unknown man-made or natural background materials. Scene-derived spectra of V5, V6, V7, DV3 and DV4 were selected as target signatures and fifteen eigenvectors were selected to characterize the scene's variability. This number was chosen to ensure that most of the undesirable background signatures would be suppressed during the analyses.

Objects possessing similar spectral features as the target spectra, but appear in a small enough quantity to exclude it from the scene's primary eigenvectors, emerge as similar targets types or false alarms. The number of false alarms on other man-made objects were far more prevalent than the author anticipated. Table 5.4 provides a tabular list of the objects that false alarmed. The target spectra are listed in the left column and

FALSE ALARMS

TARGET SPECTRA	OBJECTS
Scene-derived (V5)	V1,V2,V3,V4,V6,V7, VF3, VF7, C3, C5, C6
Scene-derived (V6)	V1,V2,V3,V4,V5,V7, VF3, VF7, C3, C5, C6
Scene-derived (V7)	V1,V2,V3,V4,V5,V6, VF3, VF7, C5, C6
Scene-derived (DV3)	C3,C5
Scene-derived (DV4)	VF1, VF2, VF4, C3, C5

Table 5.4. False Alarm Results From LPD Algorithm

their associated false contacts appear to their right. Figures 5.14 to 5.21 illustrate the application of the LPD algorithm for each of the aforementioned target objects.

Figure 5.14 shows the results from the V5 spectrum. The output from the algorithm is a pixel value ranging, in this case, from $\sim -5,000$ to $\sim +35,000$. These DNs are proportional to the material abundance (Farrand and Harsanyi, 1995). The scaling from 0-30,000 was selected on the basis of this histogram in order to illustrate the occurrences of the large data values found in the various targets. Figure 5.15 illustrates the range of V5's data values as a histogram. The broad central peak of low (absolute) values is due to the background, indicating that the bulk of endmembers in the scene have little spectral contrast. Materials of low abundance (i.e., man-made objects) are not statistically significant to the scene and will not be included in the continuum from 0.0 to 0.5×10^4 , but will appear in the residual values to the right of the main distribution. Setting a threshold, as would be done with a targeting algorithm, allows for selecting targets. Figure 5.16 shows the results of a threshold set for V5's data values at 1×10^4 .

Using a different target (V6) provides a very similar result, as illustrated Figure 5.17. The distribution of data values is very similar to that found for target V5. Thresholding the data also provides a similar result. Running the LPD analysis for target V7 provides a set of results similar to those found in the two previous targets. Figure 5.18 shows the output. Very different results were found when using the DV3 spectrum. Figure 5.19 shows how only C3 and C4 (camouflage) really lie outside the background data values. Note that the histogram distribution (Figure 5.20) is significantly skewed

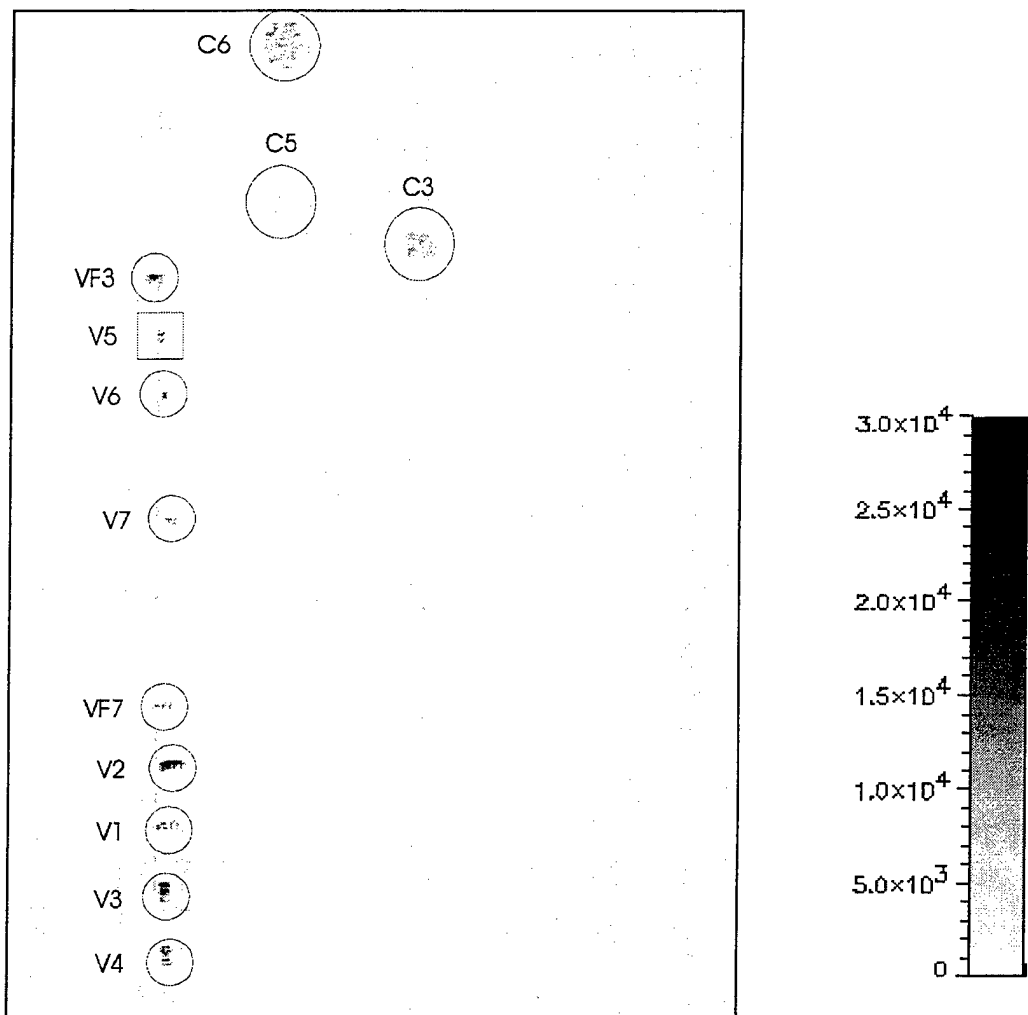


Figure 5.14. LPD Results Using V5 Target Spectra

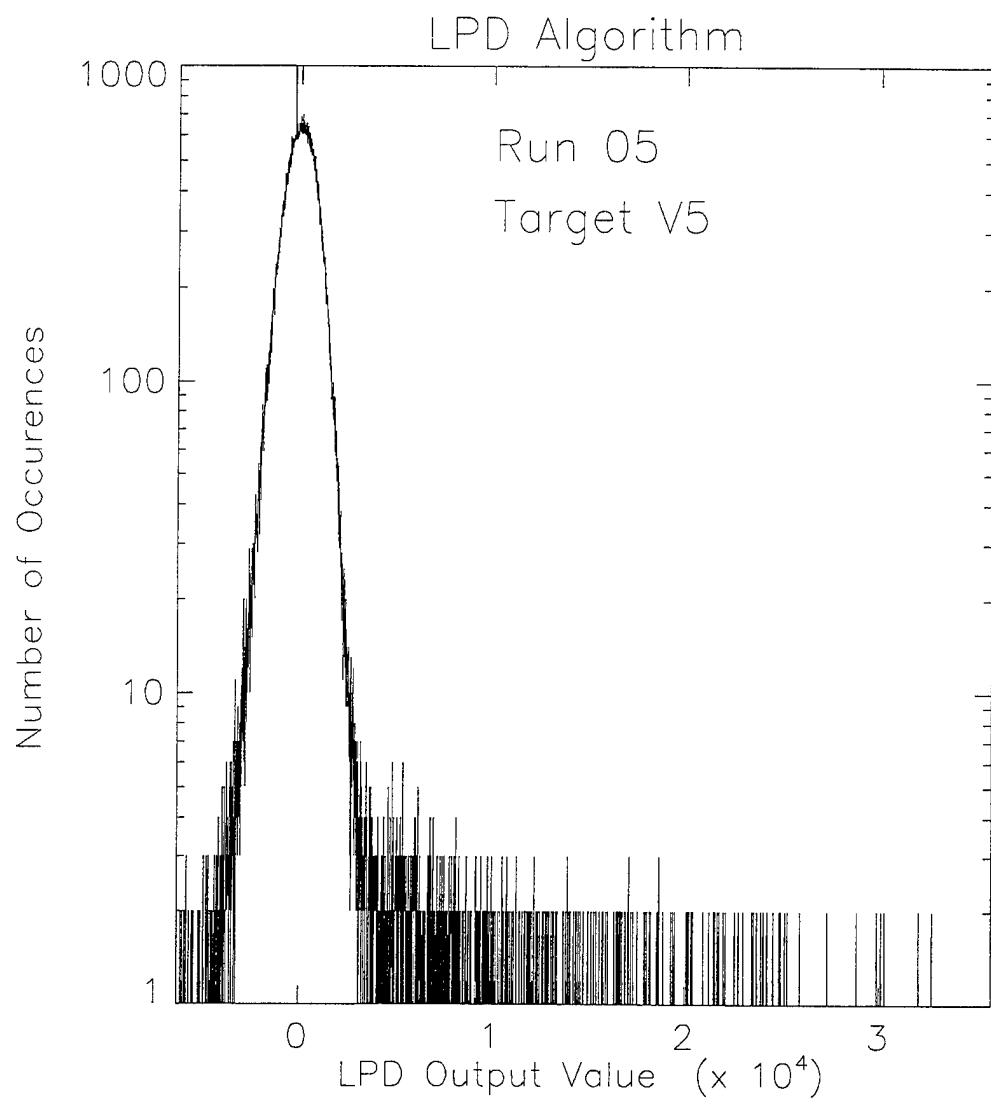


Figure 5.15. LPD Data Distribution Using V5 Target Spectra

LPD - Threshold = 1.0×10^4

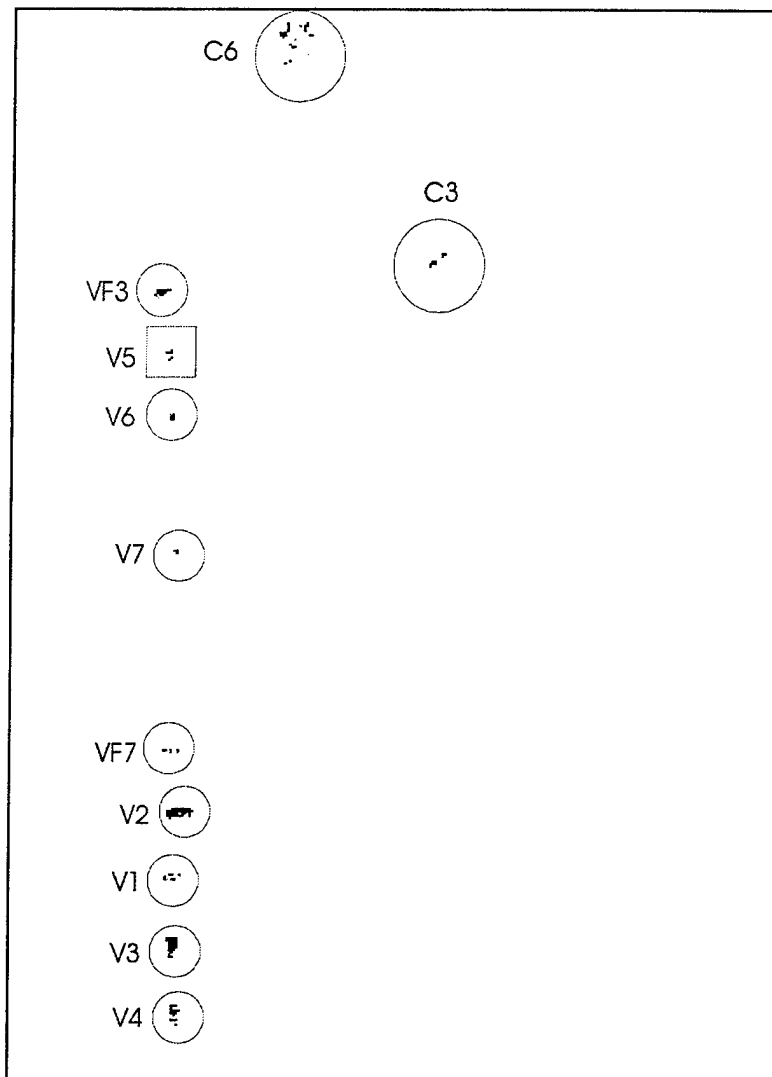


Figure 5.16. Target V5 Results Thresholded at 1×10^4

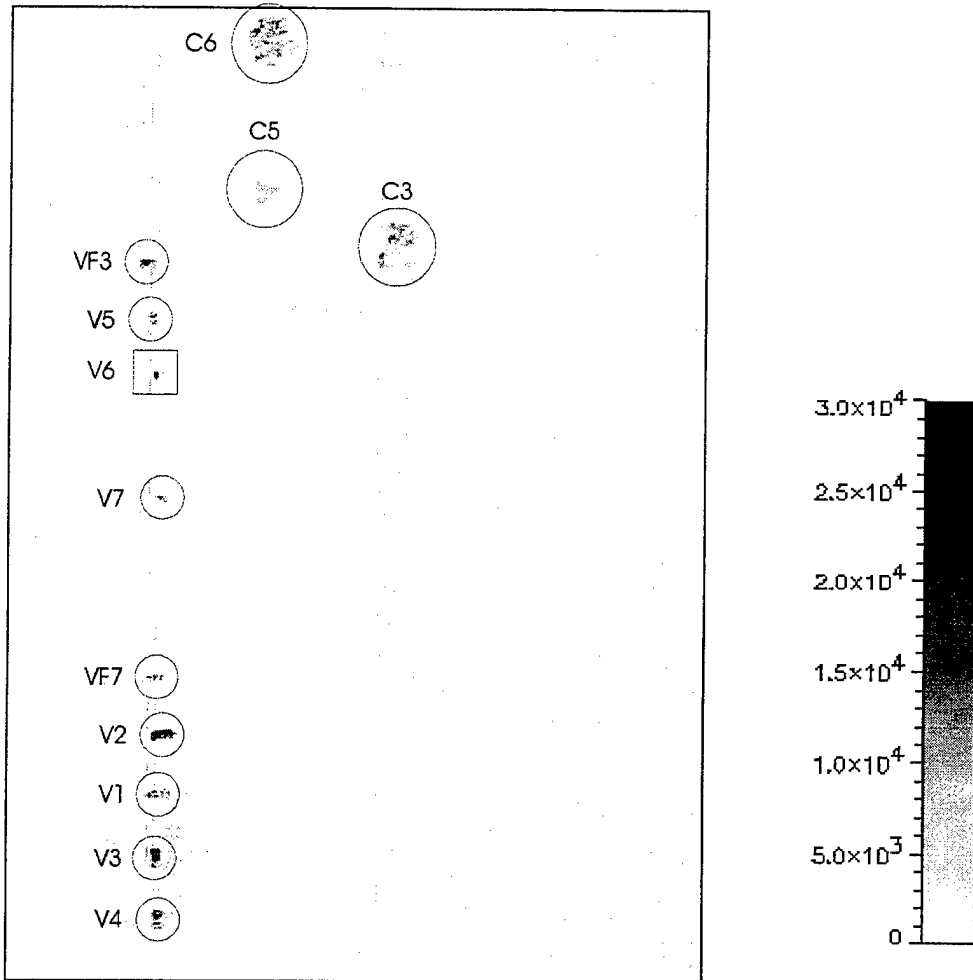


Figure 5.17. LPD Results Using V6 Target Spectra

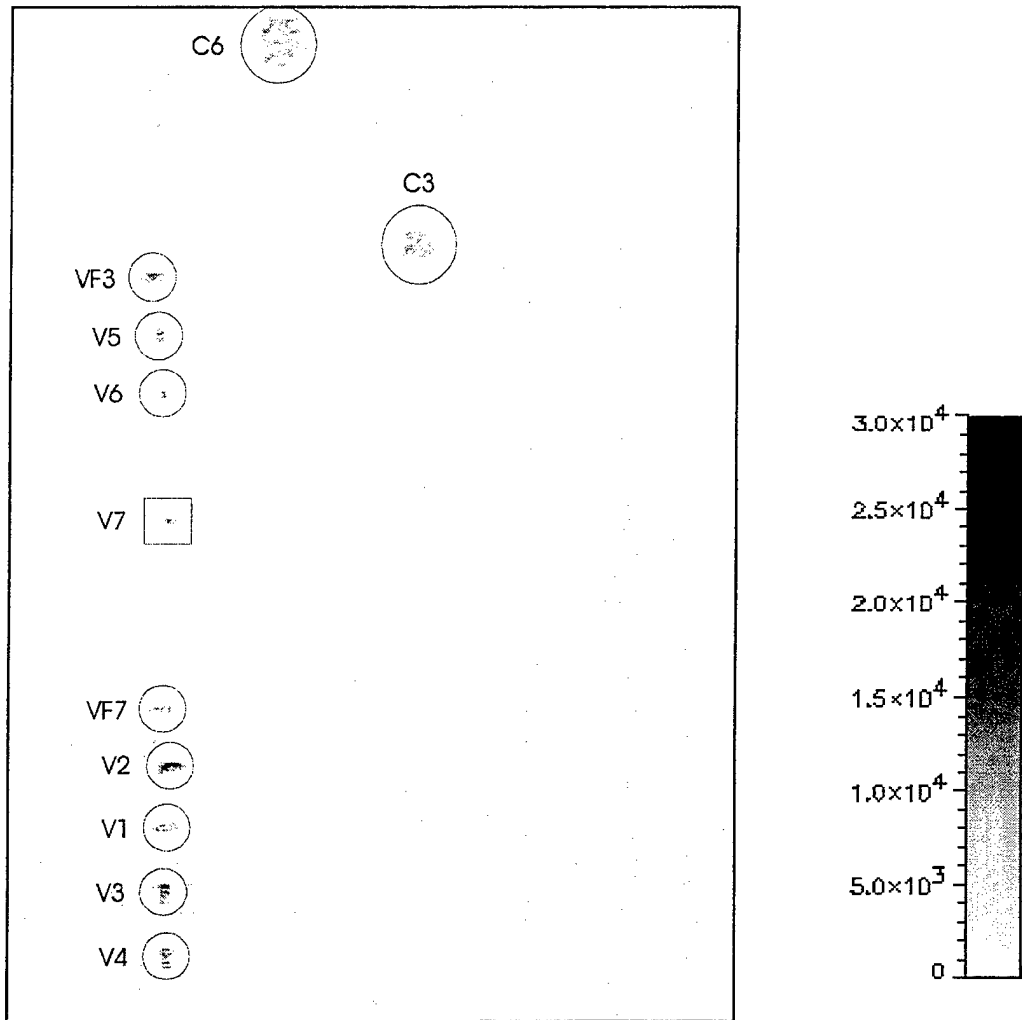


Figure 5.18. LPD Results Using V7 Target Spectra

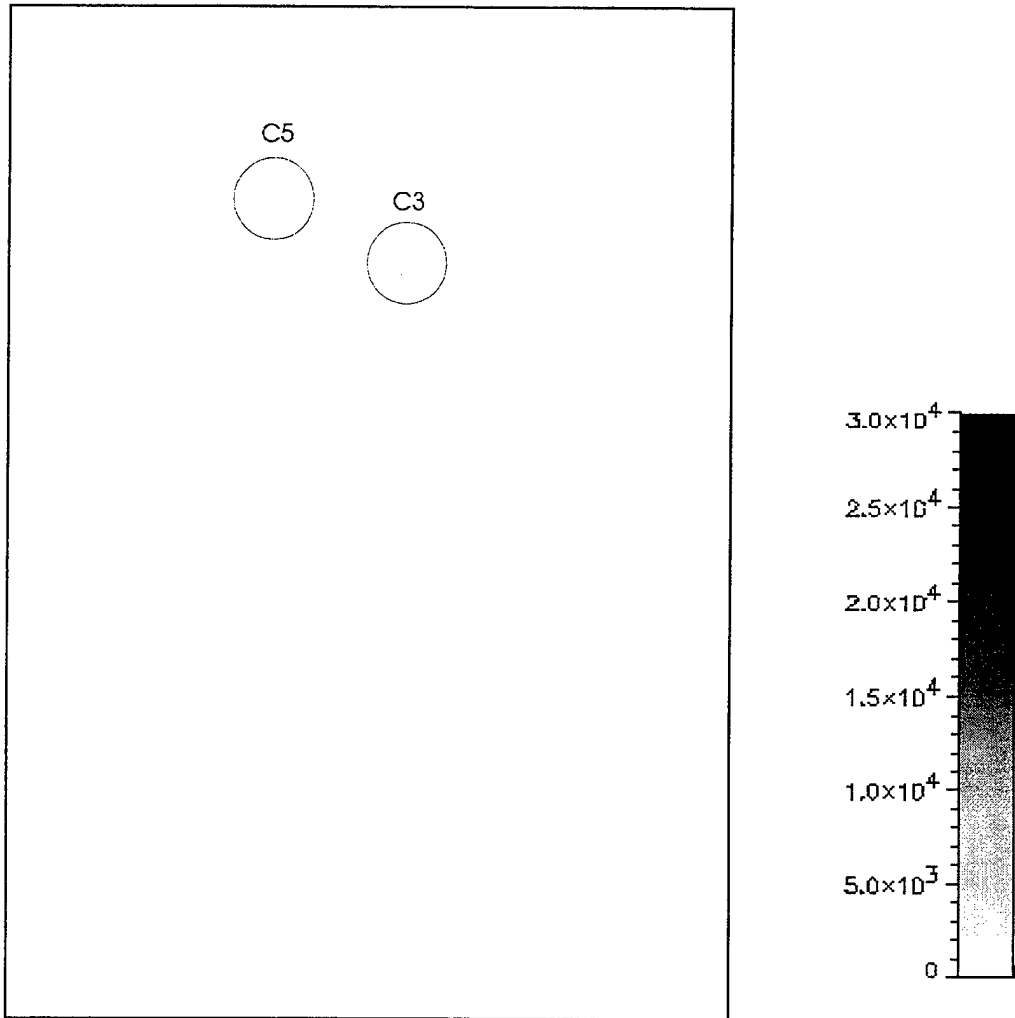


Figure 5.19. LPD Results Using DV3 Target Spectra

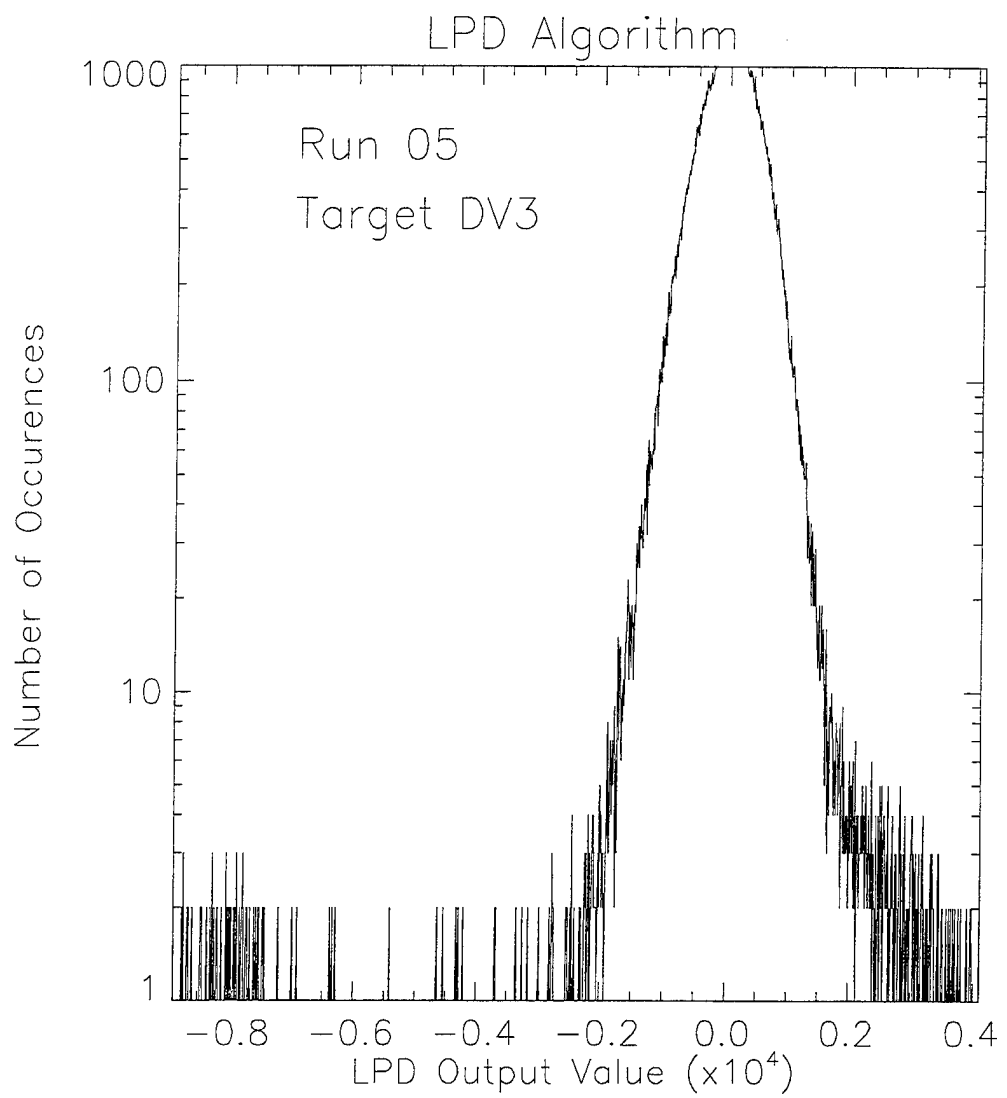


Figure 5.20. LPD Data Distribution Using DV3 Target Spectra

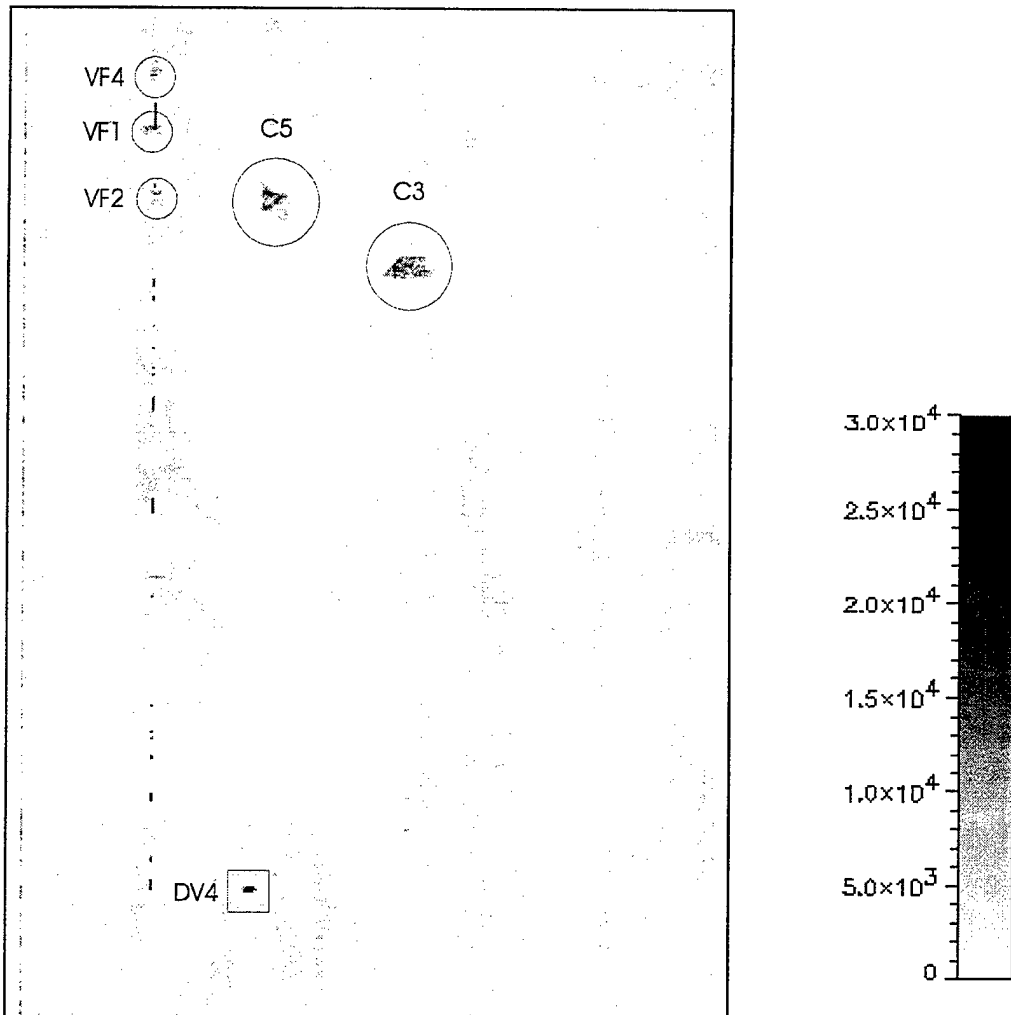


Figure 5.21. LPD Results Using DV4 Target Spectra

towards negative values, in comparison to the results for targets V5, V6, and V7. The histogram of values are quite different from the results found in all the previous examples. This unusual distribution is attributed to a near-flat spectral response caused by its improper setup (Figure 5.7). Finally, the results of running the LPD algorithm with DV4 target spectrum are shown in Figure 5.21.

The results of the applied algorithm indicates that spectral seperability between real and decoy target classes is possible. When the LPD algorithm was run with V5, V6, and V7 as target spectra, neither DV3 nor DV4 flagged as false alarms. There was, however, a significantly high false alarm rate with the HMMWVs and the other military vehicles deployed in the array, which is indicative of a strong spectral correlation. The similar spectral shape of the HMMWVs and the other military vehicles (see Figure 5.10) clearly attributed to their misidentification. Additionally, the camouflage nettings situated at the end of the target array did not pass the selection criteria and were also flagged as false alarms. This phenomenon demonstrates a significant response among woodland camouflage netting and vehicles sporting woodland paint schemes. The only real military vehicles not to false alarm were the Russian-built T72 Tanks (VF1, VF2, and VF4). VF3 was the only T72 Tank to consistently false alarm. This response may be attributed to the different compounds used in the development of Russian military paints.

The LPD algorithm was then applied to the data cube using DV3 and DV4 as target spectra. The results, as expected, show that none of the real HMMWV targets false alarmed using the decoy spectra, which further supports the assertion that the constituent materials are differentiable. This successful discrimination can be traced back to the high spectral contrast between these two dissimilar target classes and the remarkable similarities inherent in their individual class. Other man-made objects not to pass the selection criteria include the three Russian T72 Tanks and two of the three camouflage nets. Results generated using DV3 spectra show that the false alarm on the camouflage netting is less concentrated; that is, the total number of occurrences come into view in far fewer quantities than in any of the other results. This phenomenon, coupled with the fact

that the other decoy (DV4) was not alarmed, suggests that the improper deployment of DV3 had a deleterious effect on the resultant output.

4. Spectral Angle Mapper (SAM) Results

The Spectral Angle Mapper (SAM) technique was applied to the same data set using the same overall approach employed in the LPD analyses. Target objects V5, V6, V7, DV3, and DV4 were used as target spectra. The SAM algorithm is applied in two stages. First, a “Rule” image is generated. This is obtained by (effectively) taking the dot product of the spectrum at each pixel with the target spectrum. The resulting ensemble of angles is presented as a gray scale image, scaled here from 0.0 and 0.3 radian.

Classification is done by thresholding the results at a smaller angle, here defined as 0.1 radian. Objects that have spectra nearly identical to the target spectra will pass the selection criteria ($\Theta < 0.1$), and will be colored black. The remaining pixels are colored white.

The number and location of the false alarms are near-identical to those found in the LPD analyses. Table 5.5 provides a tabular list of the objects that false alarmed in the Rule Image. Figures 5.22, 5.25, 5.27, 5.29, and 5.31 shows where the number of false alarms occurred in the scene. The data are displayed over the 0.0 and 0.3 radian threshold range, and are reasonably quantifiable using the scale to the figure’s right. Figure 5.23 shows the total number of occurrences versus output value in radians. The ordinates of the Y-axis is based on a logarithmic scale. In order to avoid zero values, the results are actually plotted as one (1) plus their occurrence value. Note that the contacts appearing to the left of the solid vertical line, shown here at 0.1 radian, represent the occurrences that appear in the classifier. Rule Image occurrences could be shown by moving the same vertical line out to 0.3 radian. Table 5.6 provides a tabular list of the objects that false alarmed in the SAM Classifier. Figures 5.24, 5.26, 5.28, 5.30, and 5.32 show the false alarms generated. The data are displayed based on a threshold angle of 0.1 radian. Attempts to reduce the false alarm rate by incrementally reducing the threshold angle had little effect on the final output.

FALSE ALARMS

TARGET SPECTRA	OBJECTS
Scene-derived (V5)	V1,V2,V3,V4,V6,V7, VF3, VF7, C3, C5, C6
Scene-derived (V6)	V1,V2,V3,V4,V5,V7, VF3, VF7, C3, C5, C6
Scene-derived (V7)	V1,V2,V3,V4,V5,V6, VF1, VF2, VF3, VF4, VF7, C3, C5, C6
Scene-derived (DV3)	V1,V3,V4, VF1, VF2, VF3, VF4, VF5, VF6, VF7
Scene-derived (DV4)	VF1, VF2, VF4, VF5, VF6, VF7, DV3

Table 5.5. SAM Rule False Alarms

FALSE ALARMS

TARGET SPECTRA	OBJECTS
Scene-derived (V5)	V1,V2,V3,V4,V6,V7, VF3, VF7
Scene-derived (V6)	V1,V2,V4,V5,V7
Scene-derived (V7)	V1,V3,V4,V5,V6, VF3
Scene-derived (DV3)	VF6
Scene-derived (DV4)	None

Table 5.6. SAM Classifier False Alarms

The findings indicate that spectral discrimination between the real and decoy target classes is possible using this technique. When the SAM algorithm was applied using V5, V6, and V7 as target spectra, neither DV3 nor DV4 appeared as false alarms. The algorithm did produce nearly the same false alarm pattern observed in the LPD analyses, with only a few notable exceptions. The actual HMMWVs consistently false alarmed on the other military vehicles deployed throughout the scene. This is further evidence to support the assertion that a strong correlation exists between the spectral characteristics of the paint used by the real military vehicles. The absence of false alarms on the camouflage netting is the most obvious feature missing in the SAM classifiers. These results clearly indicate that the both camouflage nets and decoys spectra have an angular difference of greater than 0.1 radian. The camouflage netting is however visible in each of the Rule Image(s), and thus, establishes that its angular separation falls between 0.1 and 0.3 radian. For the first time, other, quasi-targets such as the tire tracks, dirt roads, and areas of exposed soil appear in the Rule image.

The SAM algorithm was then applied to the data cube using DV3 and DV4 as target spectra. The results show that none of the real target vehicles or camouflage netting false alarmed in the SAM classifier. The only man-made object not to pass DV3's selection criteria was a BTR (VF6). The false alarms generated in DV4's Rule Image is of considerable interest. The large angle (threshold criteria) separation allows us to see exactly how unique the decoy's spectra when is compared to the other objects in the target array. Note that neither the Rule Image nor SAM Classifier figure show any evidence of misidentification with any of the HMMWVs. Distinctive patterns are clear indicators of a spectral distinctiveness between the military camouflage paint covering the real vehicles and the canvas materials used to construct the decoys. The SAM algorithm further demonstrated the capability to detect man-made materials against a natural grass background. Findings associated with DV3's spectra should be considered suspect.

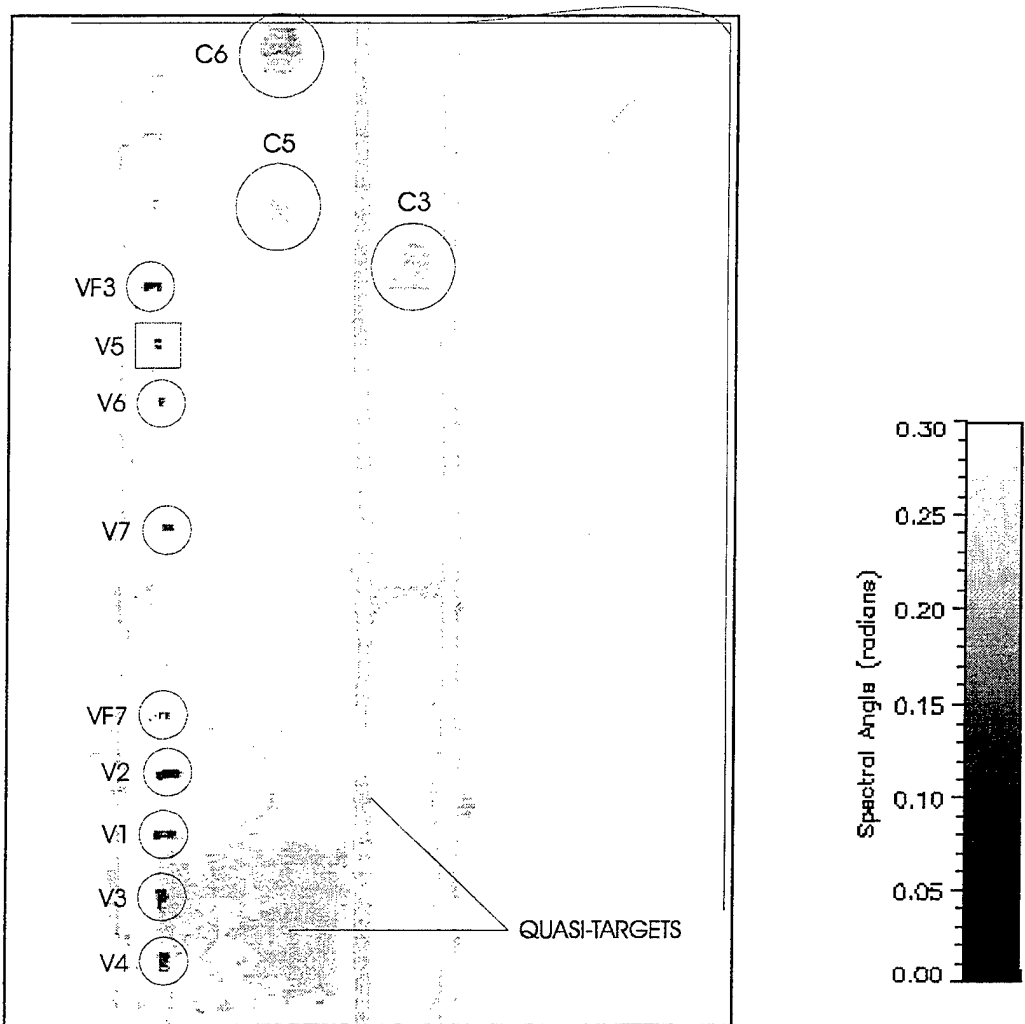


Figure 5.22. SAM Rule Image Using V5 Spectra

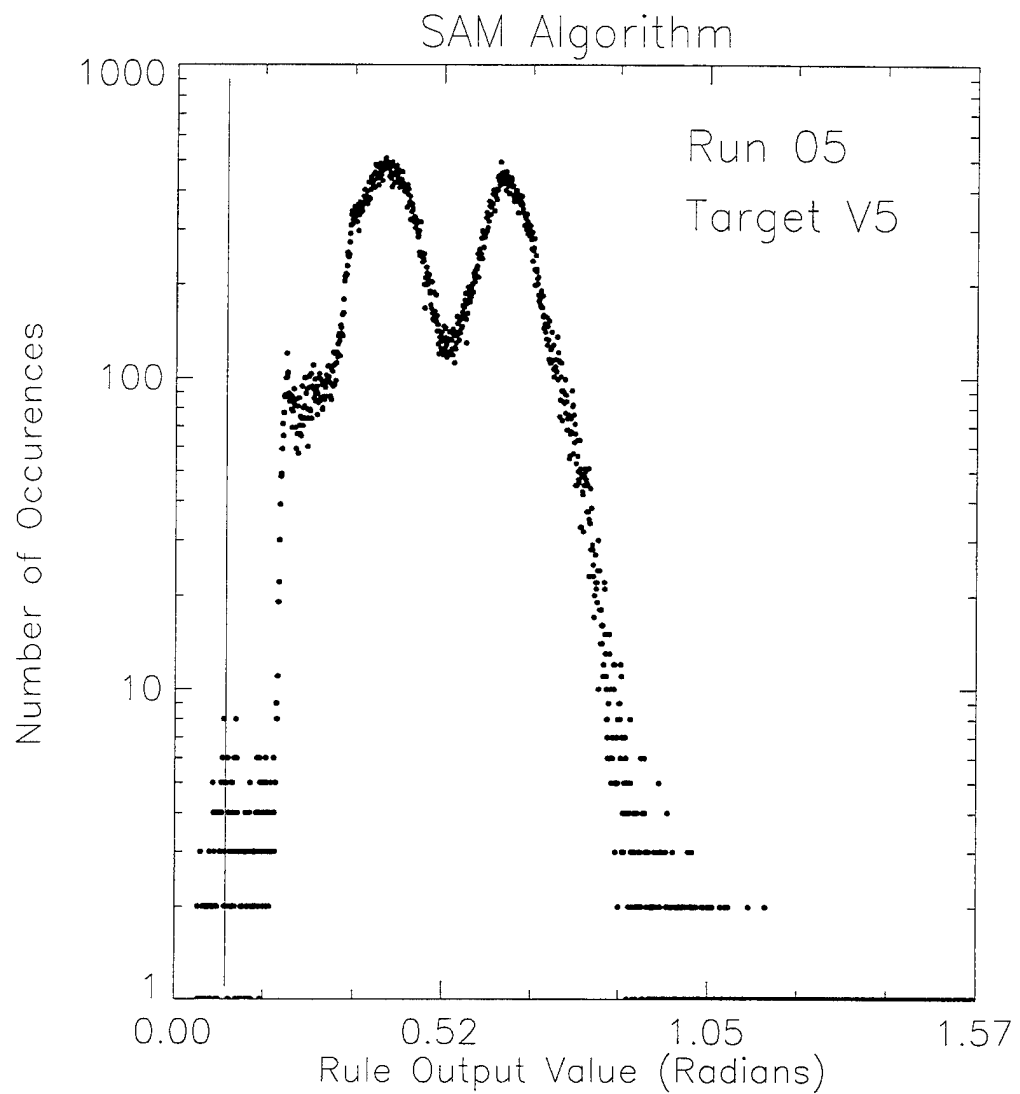


Figure 5.23. SAM Rule Image Data Distribution Using V5 Spectra

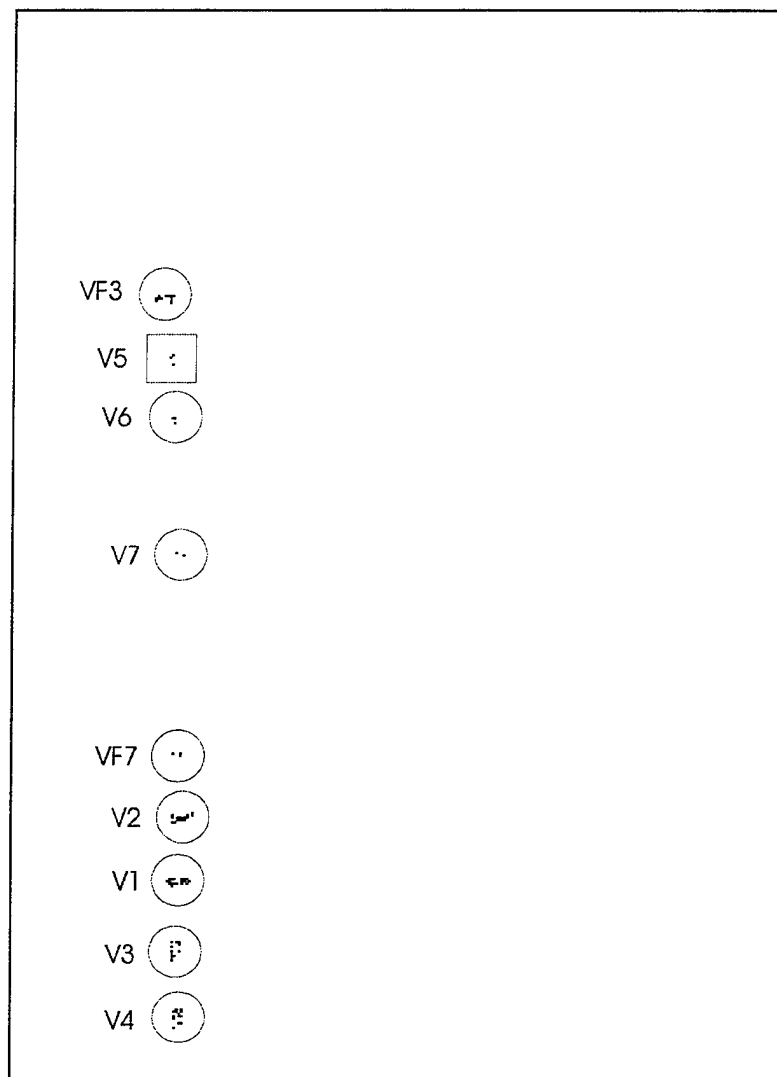


Figure 5.24. SAM Classifier Using V5 Spectra

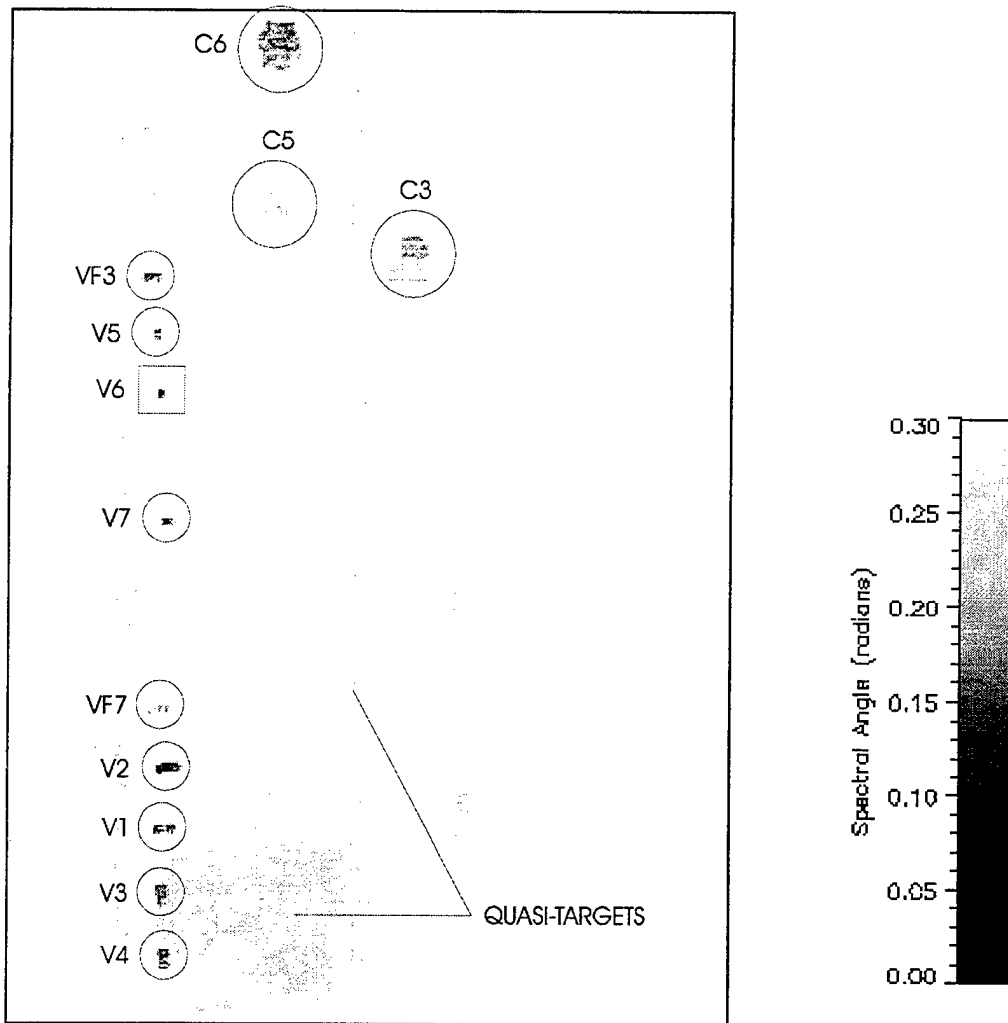


Figure 5.25. SAM Rule Image Using V6 Spectra

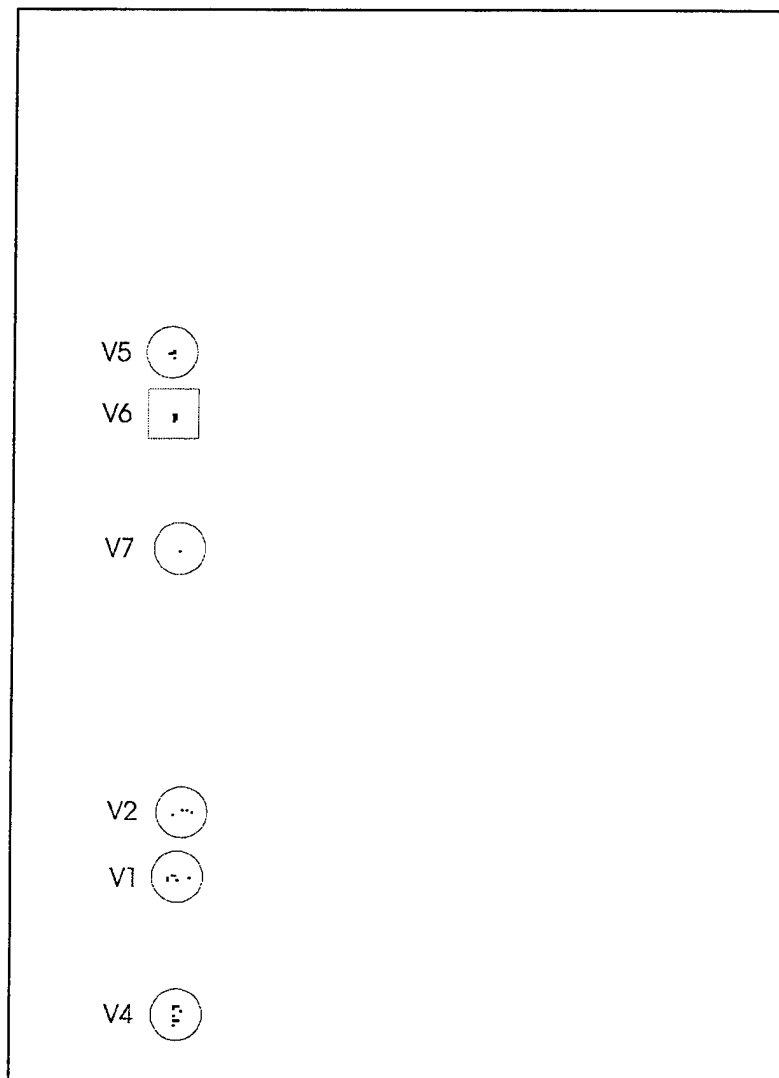


Figure 5.26. SAM Classifier Using V6 Spectra

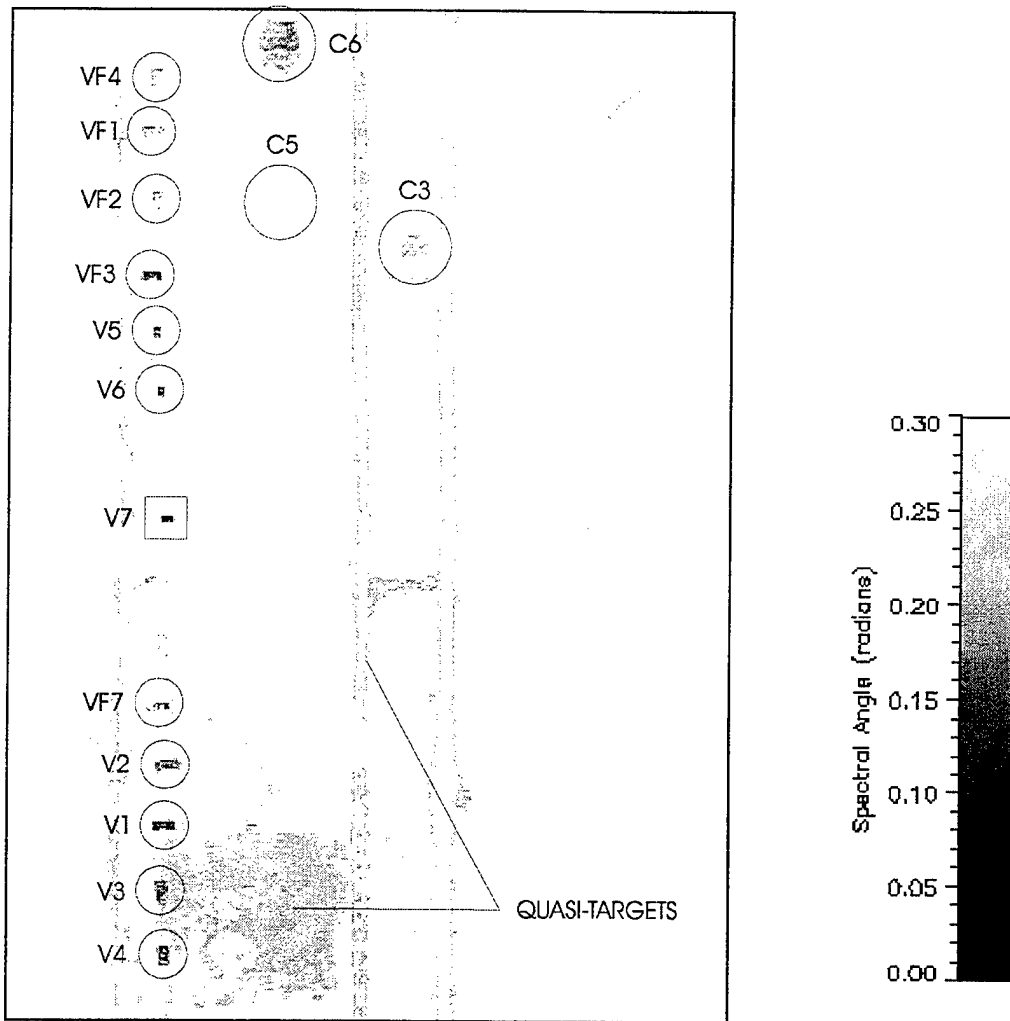


Figure 5.27. SAM Rule Image Using V7 Spectra

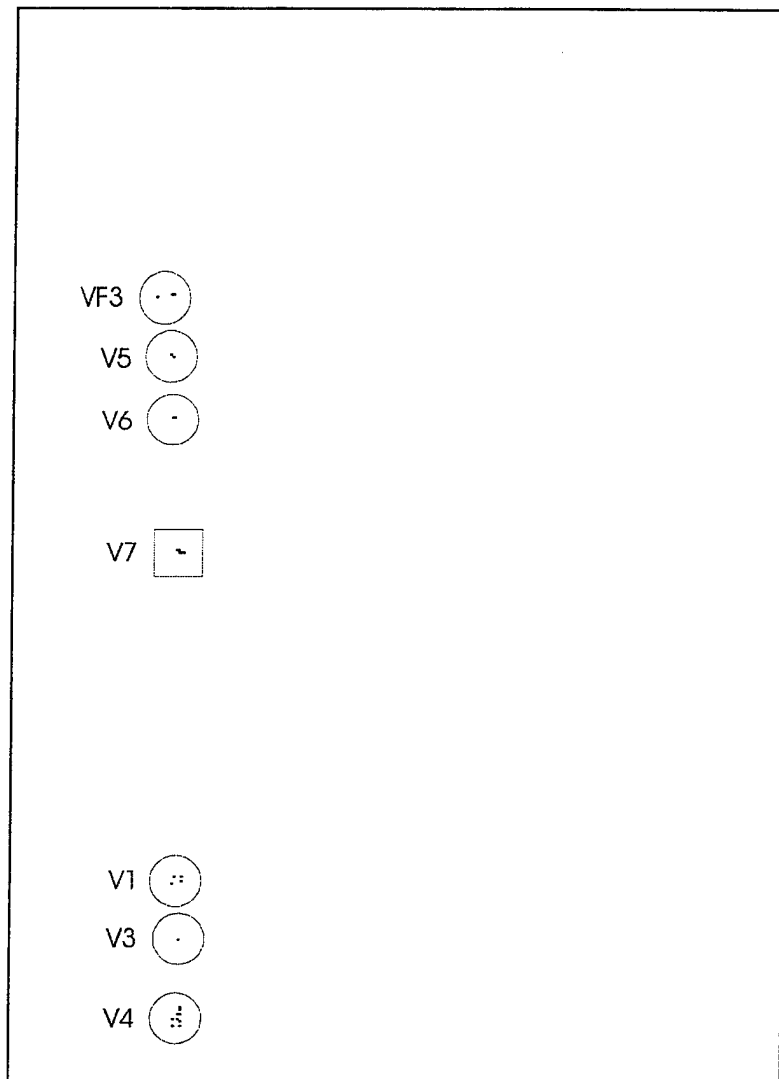


Figure 5.28. SAM Classifier Using V7 Spectra

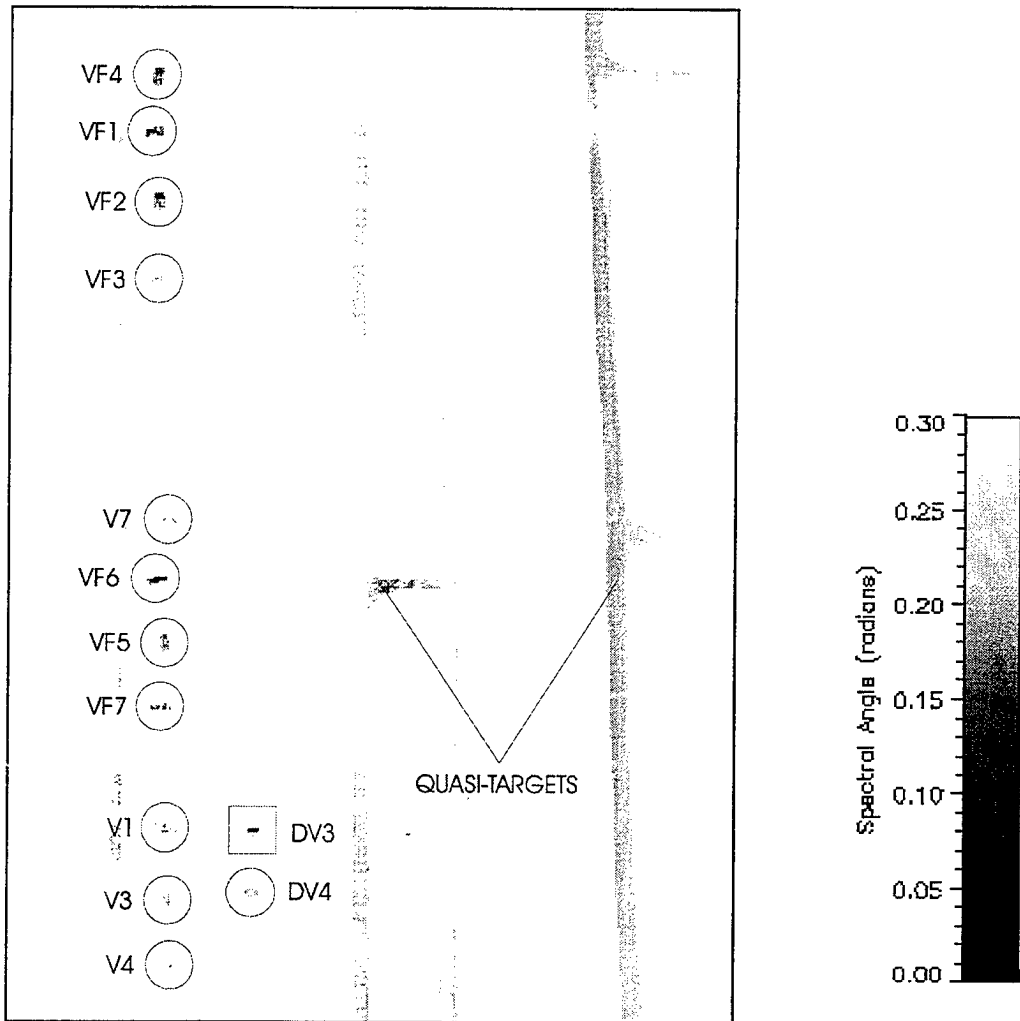


Figure 5.29. SAM Rule Image Using DV3 Spectra

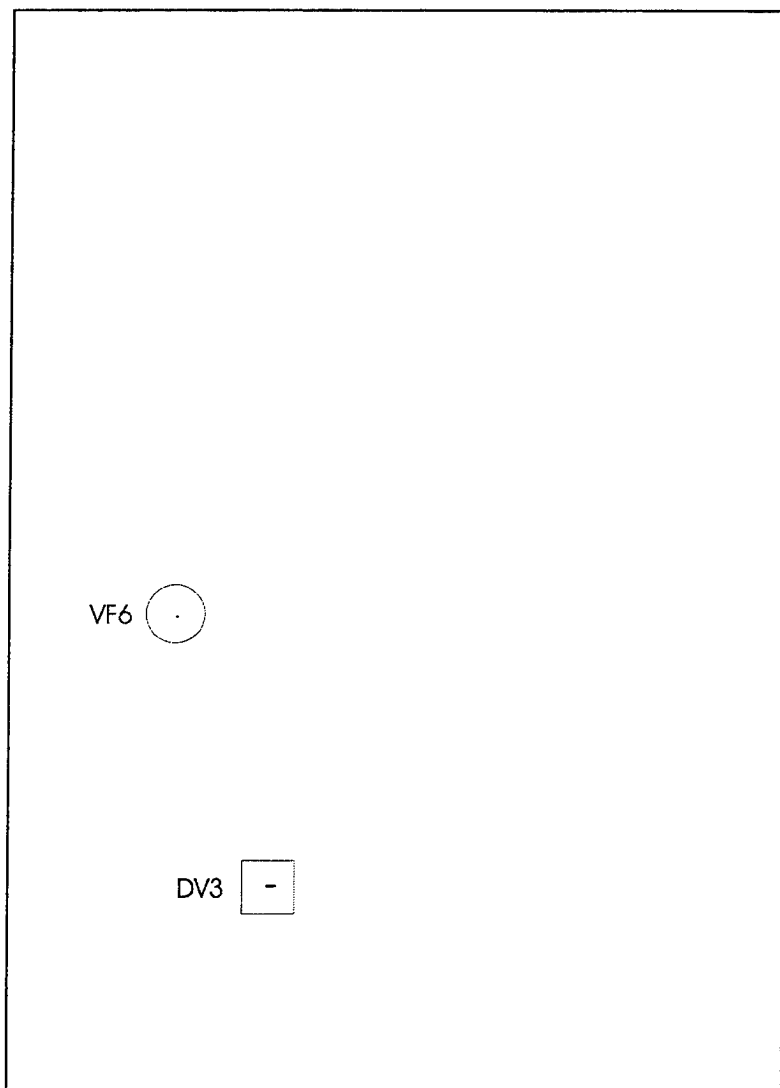


Figure 5.30. SAM Classifier Using DV3 Spectra

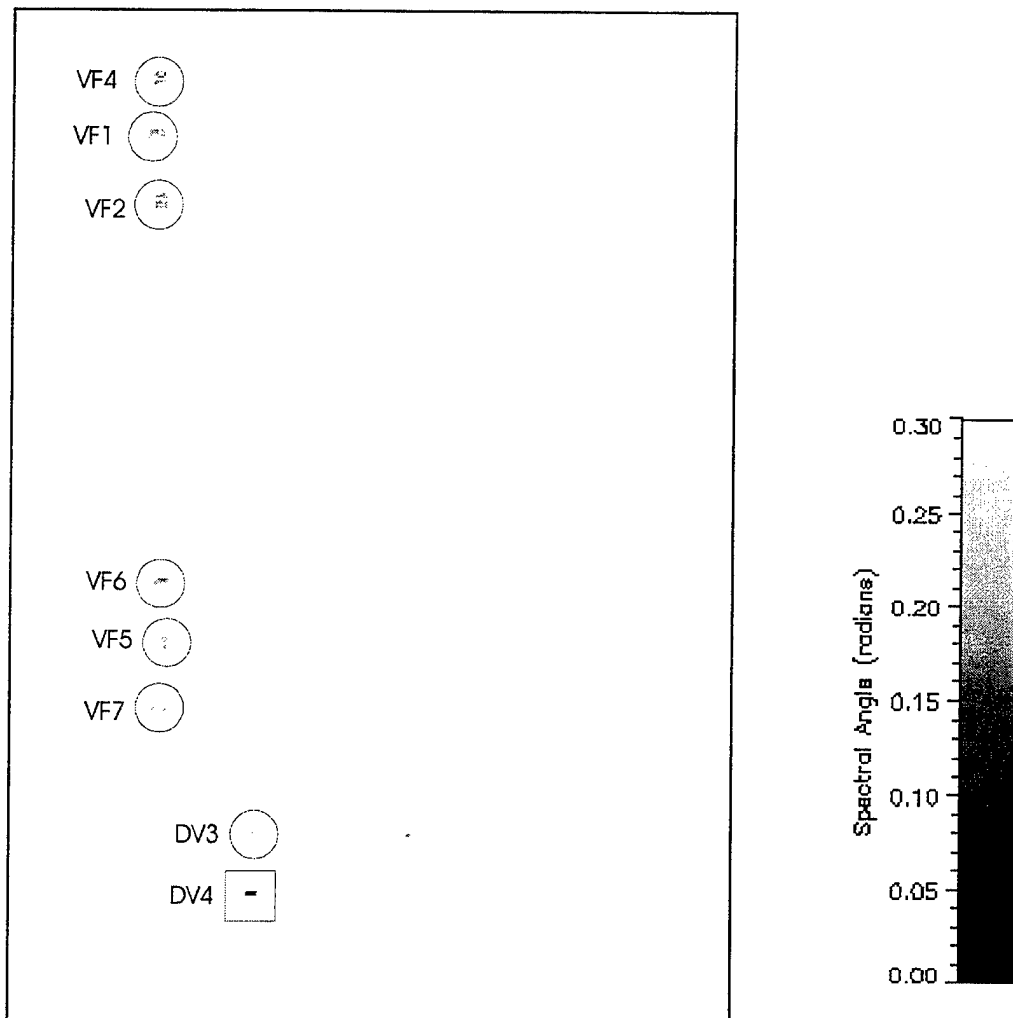


Figure 5.31. SAM Rule Image Using DV4 Spectra



Figure 5.32. SAM Classifier Using DV4 Spectra

VI. CONCLUSIONS AND RECOMMENDATIONS

Operation Forest Radiance I was the HYMSMO program's first attempt at examining the physics and phenomenology of various military target classes under different environmental conditions. The author found the experiment to be very well designed and the collection site an ideal location to conduct the myriad mini-experiments selected for research. The HYDICE instrument and data processing techniques employed during the exercise also proved themselves extremely capable given the high quality of the data made available for exploitation. The resultant outputs generated by the PCA, LPD, and SAM exploitation techniques further demonstrated the capability of today's hyperspectral imaging technologies to satisfy the decoy discrimination problem being investigated in this thesis.

The PCA method produced the information needed to estimate the intrinsic dimensionality of the image cube being analyzed. However, this information came at a premium price. The algorithm was found to be computationally expensive to run and the results somewhat difficult to interpret. The PCA algorithm did not provide any purposeful information (beyond computing the primary eigenvectors that model the endmembers in the scene) that contributed directly to solving the research objective. Another technique, however, did use these results to suppress the unwanted background signatures in the image and facilitated detection and discrimination of the targets of interest.

The LPD algorithm performed extremely well at detecting residual spectra. These residual spectra did not contribute significantly to the scene's overall statistics, and thus, flagged as false alarms. The LPD method was an effective technique for suppressing the background signatures using the scene's primary eigenvectors and for discriminating between the HMMWVs and decoys. The SAM technique performed exceptionally well at discriminating these target objects. The SAM proved to have a significant advantage over the LPD method when it comes to obviating target misidentifications. For example,

the false alarms observed with the LPD algorithm (i.e., camouflage netting) suggest an influence from the relative brightness value of the camouflage material. The SAM algorithm is able to match the spectra without giving statistical weight to their relative brightness values to produce a quantifiable measure of effectiveness.

The multivariate approach employed during the analyses proved to be a worthwhile strategy. The findings clearly show that the actual and decoy target objects are differentiable in a natural grass environment. The low number of false alarms on the decoys serves as strong evidence that the objects are being identified, not just detected. The significant high false alarm rate of the real vehicles indicates that the spectral signatures are actually the signature of the surface paint, not the vehicle itself. The different hues in the paint scheme did prevent the possibility of acquiring homogeneous pixels; thus, a single pixel is characterized by a one signature that represents all of the paint's spectral components. This complex pixel problem seemed to stress the performance of the LPD and SAM algorithms.

Hyperspectral technologies can be a viable tactical asset if the technology is allowed to advance at its current rate. Despite these initial successes, however, further analysis will be required to determine the practicality of using hyperspectral technologies to satisfy many of the requirements relevant to the warfighter. Any negative findings concerning this data set or analysis techniques to discriminate anomalous contacts should not be extrapolated to past or future experiments. The author recommends that future studies include decoys constructed of different types of materials. Detailed laboratory experiments should be conducted to assess the spectral variability associated with military paint compounds.

LIST OF REFERENCES

Anderson, M., Forest Radiance I, Collection and Exploitation Operations Plan (CEOP-3), Hyperspectral MASINT Support to Military Operations, HYMSMO Program Office, pp. 1-47, 1995.

Aldrich, W.S., Kappus, M.E., Resmini, R.G., and Mitchell, P., HYDICE Post Flight Data Processing, *Proceedings of the International Society for Optical Engineering (SPIE)*, Vol. 2758, pp. 354-363, 9-11 April 1996.

Campbell, J.B., Introduction to Remote Sensing, New York: The Guilford Press, 1987.

Elachi, C., Introduction to the Physics and Techniques of Remote Sensing, New York: John Wiley and Sons, 1987.

Farrand, W.H., and Harsanyi, J.C., Discrimination of Poorly Exposed Litologies in Imaging Spectrometer Data, *Journal of Geophysical Research - Plants*, pp. 1565-1578, 1995.

Farrand, W.H., A Comparison for Retrieving Apparent Surface Reflectance from Hyperspectral Data, *Proceedings of the International Symposium on Spectral Sensing Research (ISSSR)*, Vol. 2, pp. 1154-1164, 1992.

Fay, M.E., An Analysis of Hyperspectral Imagery Data Collected During Operation Desert Radiance, Masters Thesis, Naval Postgraduate School, Monterey, CA., p. 21, June 1995.

Goetz, A.F.H., Vane, G., Soloman, J.E., and Rock, B.N., Imaging Spectrometry of Earth Remote Sensing, *Science*, Vol. 228, No. 4704, pp. 1147-1153, June 1985.

Harsanyi, J.C., and Chang, C.I., Hyperspectral Image Classification and Dimensionality Reduction: An Orthogonal Subspace Projection Approach, *IEEE Transactions on Geoscience and Remote Sensing*, Vol. 32, No. 4, pp. 779-785, 1994.

Herring, M., The Shuttle Imaging Spectrometer Experiment (SISEx), *Proceedings of the International Society for Optical Engineering (SPIE)*, Vol. 834, pp. 181-187, August 1987.

Hoffer, R.M., Davis, S.M., Landgrebe, D.A., Phillips, T.L., Swain, P.H., Lindenlaub, and J.C., Silva, L.F., Remote Sensing: A Quantitative Approach, New York: McGraw-Hill, 1978.

Kappus, M., Aldrich, W., and Resmini, R.G., The Flexible HYDICE Sensor's First Year of Operation, *Proceedings of the 11th Thematic Conference on Remote Sensing*, Vol. 1, pp. 433-440, February 1996.

Kruse, F.A., Use of the Airborne Imaging Spectrometer Data to Map Minerals Associated with Hydrothermally Altered Rocks in the Northern Grapevine Mountains, Nevada, California, *Remote Sensing of the Environment*, Vol. 24, No. 1, pp.31-52, February 1988.

Kruse, F.A., Lefkoff, A.B., Boardman, J.W., Heidebrecht, K.B., Shapiro, A.T., Barloon, P.J., and Goetz, A.F.H., The Spectral Image Processing System (SIPS) - Interactice Visualization and Analysis of Imaging Spectrometer Data, *Remote Sensing of the Environment*, Vol. 44, No. 2 and 3, pp.145-163, May-June 1993.

Marshall, J.P., Near-Real-Time Intelligence of the Tactical Battlefield. Research Report No. AU-ARI-92-6, Maxwell A.F.B, AL: Air University Press, pp. 42-43, January 1994.

Multispectral User's Guide (MUG), Washington, D.C., Department of Defense, August 1995.

Pagano, T.S., and Durham, R.M., Moderate Resolution Imaging Spectroradiometer (MODIS), *Proceedings of the International Society for Optical Engineering (SPIE)*, Vol. 1939, pp. 1-13, February 1993.

Palmadesso, P., Antoniades, J., Baumback, M., Bowles, J., and Rickards, J., Use of Filter Vectors and Fast Convex Set Methods in Hyperspectral Analysis, *Proceedings of the International Symposium on Spectral Sensing Research (ISSSR)*, Vol. 1939, 1995.

Porter, W.M., and Enmark, H.T., A System Overview of the Airborne Visible/Infrared Imaging Spectrometer (AVIRIS), *Proceedings of the International Society for Optical Engineering (SPIE)*, Vol. 834, pp. 22-29, August 1987.

Richards, J.A., Remote Sensing Digital Image Analysis, New York: Springer-Verlag, 1995.

Rinker, J. N., Hyperspectral Imagery - What Is It? - What Can It Do?, Presented at the USACE Seventh Remote Sensing Symposium, 1992.

U.S. Joint Chiefs of Staff. Joint Doctrine for Intelligence Support to Operations. Joint Pub 2-0. Washington, D.C.: Joint Chiefs of Staff, p. II-1, May 1995.

Unmanned Aerial Vehicles (UAVs), *Annual Reports*, August 1995.

Ustin, L.S., Duan, L., Hart, Q.J., and Haxo, R., Seasonal Changes Observed in AVIRIS Images of Jasper Ridge, California, *International Geoscience and Remote Sensing Symposium*, Vol. 4, pp. 2360-2362, August 1994.

Vane, G., and Goetz, A.F.H., Terrestrial Imaging Spectroscopy: Current Status, Future Trends, *Remote Sensing of the Environment*, Vol. 44, pp. 117-125, May-June 1993.

BIBLIOGRAPHY

Adams, J.B., Smith, M.O., and Gillespie, A.R., Simple Models for Complex Natural Surfaces: A Strategy for the Hyperspectral Era of Remote Sensing, *International Geoscience and Remote Sensing Symposium (IGARSS)*, pp. 1-9, July 1989.

Barr, S., Hyperspectral Image Processing, *Proceedings of the International Symposium on Spectral Sensing Research (ISSSR)*, Vol. 1, pp. 477-490, July 1994.

Bernhardt, P.A., and Antoniadis, J.A., Hyperspectral Imaging Using Rotational Spectro-Tomography, *Proceedings of the International Society for Optical Engineering (SPIE)*, Vol. 2480, p. 78, April 1995.

Evens, T.D., and Henley, P., Spectral Characteristics (0.4 μm - 2.5 μm) and the Detection of Camouflage Materials, *Proceedings of the International Symposium on Spectral Sensing Research (ISSSR)*, Vol. 1, pp. 497-515, July 1994.

Fulghum, D.A., Predators Bound For Bosnia Soon. *Aviation Week and Space Technology*, pp. 72-73, November 1995.

Gillespie, A.R., Smith, M.O., Adams, J.B., Willis, S.C., Fisher III, A.F., and Sabol, D.E., Interpretation of Residual Images: Spectral Mixture Analysis of AVIRIS Images, Owens Valley, California, *Proceedings of the Second Airborne Visible/Infrared Imaging Spectrometer (AVIRIS) Workshop*, JPL Publication, 90-54, pp. 243-270, 1990.

Goetz, A.F.H., Vane, G., Soloman, J.E., and Rock, B.N., Imaging Spectrometry of Earth Remote Sensing, *Science*, Vol. 228, No. 4704, pp. 1147-1153, June 1985.

Harsanyi, J.C., Farrand, W.H., Heji, J.M., and Chang, C.I., Automated Identification of Endmembers in Hyperspectral Image Sequences, *Proceedings of the International Symposium on Spectral Sensing Research (ISSSR)*, Vol. 1, pp. 267-276, July 1994.

Johnson, P.E., Smith, M.O., and Adams, J.B., Quantitative Analysis of Planetary Reflectence Spectra with Principal Components Anaysis, *Proceedings of the 15th Lunar and Planetary Science Conference, Part 2, Journal of Geophysical Research*, Vol. 90, pp. C805-C810, February 1985.

Kruse, F.A., Imaging Spectrometer Data Analysis - A Tutorial, *Proceedings of the International Symposium on Spectral Sensing Research (ISSSR)*, Vol. 1, pp. 44-50, July 1994.

Lewotsky, K., Hyperspectral Imaging: Evolution of Imaging Spectrometry, *Optical Engineering (EO) Reports*, p. 15, November 1994.

Molinelli, E., and Muncill, G., Use of Principal Components to Characterize Upwelling off the Coast of California, *Proceedings of the International Symposium on Spectral Sensing Research (ISSSR)*, Vol. 2, pp. 707-710, July 1994.

Pieters, C.M., and Englert, P.J., Remote Geochemical Analysis: Elemental and Mineralogical Comparison, New York: The Press Syndicate of the University of Cambridge, 1993.

U.S. Department of Defense. Conduct of the Persian Gulf War, Final Report to Congress. Washington, D.C.: Department of Defense, p.167, April 1992.

Vane, G., and Goetz, A.F.H., Terrestrial Imaging Spectroscopy, *Remote Sensing of the Environment*, Vol. 24, pp. 1-29, February 1988.

Vane, G., First Results from the Airborne Visible/Infrared Imaging Spectrometer (AVIRIS), *Proceedings of the International Society for Optical Engineering (SPIE)*, Vol. 834, pp. 166-174, August 1987.

INITIAL DISTRIBUTION LIST

1. Defense Technical Information Center 2
8725 John J. Kingman Road., Ste 0944
Fort Belvoir, Virginia 22060-6218
2. Dudley Knox Library 2
Naval Postgraduate School
411 Dyer Rd.
Monterey, California 93943-5101
3. Richard C. Olsen, Code PH/OS 5
Department of Physics
Naval Postgraduate School
Monterey, California 93943-5002
4. Chairman, Code CC 1
C4I Academic Group
Naval Postgraduate School
Monterey, California 93943-5002
5. David D. Cleary, Code PH/CL 2
Department of Physics
Naval Postgraduate School
Monterey, California 93943-5002
6. Lieutenant Steven M. Bergman 2
2012 Cottonwood Street
Findlay, Ohio 45840
7. HYDICE Program Office 3
11781 Lee - Jackson Memorial Highway
Fairfield, VA 22033-3309
8. George Conner, Code OR/CO 2
Department of Operations Research
Naval Postgraduate School
Monterey, California 93943-5002

9. Captain Frank Kelly, Code NS/KF	1
Department of National Security Affairs	
Naval Postgraduate School	
Monterey, California 93943-5002	
10. Captain A. Legrow, Code N632	1
Navy TENCAP	
Pentagon, Room 5D773	
Washington D.C., 20350-2000	